Development of Thermocells Driven by Volume Phase Transition of Hydrogel Nanoparticles

郭, 本帥

Development of Thermocells Driven by Volume Phase Transition of Hydrogel Nanoparticles

2016-2021

Kyushu University

Department of Chemical Engineering

Benshuai Guo

Supervisor: Yoshiko Miura, Yu Hoshino

Contents

Chapter 1. Introduction

1.1. Background of thermal energy harvesting

1.1.1. Global thermal energy potential

The thermal energy in the environment is abundantly available from solar energy, geothermal and industrial sources.[1] With the increase in global energy consumption, a large amount of thermal energy is discharged into the environment without being effectively or economically used.[2] As a renewable energy source, energy production from thermal energy is considered to be one of the key instruments to restrain the growth of global energy demands and thereby abate greenhouse gas emissions.[3],[4]

Generally, the energy conversion process chain from the primary energy carrier to the final energy use is subject to considerable losses. In the global industrial primary energy utilization, 63% of the energy is lost in the process of combustion and heat transfer.[5] The major loss can be defined as 'waste heat' , and is determined to be a very considerable source of energy.[6] Researchers classify effectively utilized energy in the end use as energy services, and the lost part is distinguished as rejected energy[2]. According to statistics from Lawrence Livermore National Laboratory, in all energy sectors, including industry, Japan's rejected energy still accounts for close to 60%.[7] In the United States in 2020, this rejected energy data representing waste heat emissions is also as high as 66%.[8] Not only in the industrial sector, but also in the commercial, residential and transportation sectors also show huge energy losses. It is estimated that the largest source of waste heat in the energy consumption process chain around the world is power generation (Figure 1-1).[2] It turns out that the global energy loses about

72% after consuming the primary energy carrier, and this part of the energy is discharged into the environment as waste heat.

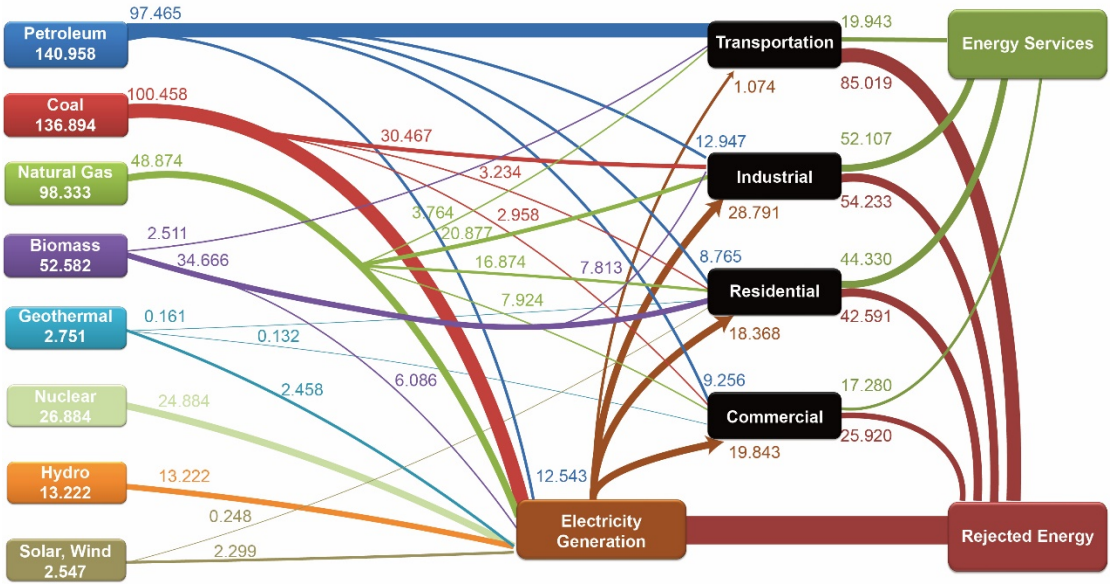

Figure 1-1. Estimated world energy consumption in petajoule (PJ). The PJ is equal to one quadrillion (10^{15}) joules.

The process of generating waste heat has many forms, and all of them appear in the conversion of energy. The actual energy conversion device has a theoretical efficiency limit, and the energy balance between energy input and energy services is the theoretical basis for analyzing waste heat generation (Figure 1-2).[5] The energy loss can be summarized into three main categories, namely exhaust loss, effluent loss and other losses. Exhaust loss refers to flue gas or vapor exhaust. The effluent loss mainly comes from the coolant with water or air. Other losses include radiation, convection, conduction, friction, electrical resistance, transmission, etc.[9] The existence form of waste heat is determined by the way of energy loss.

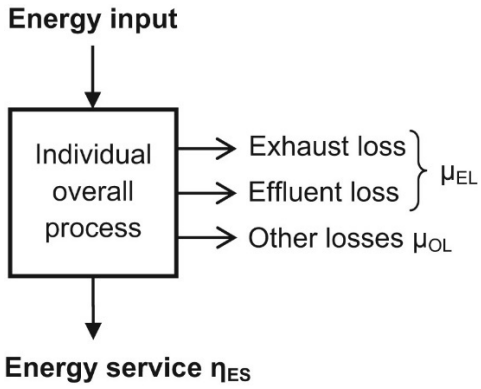

Figure 1-2. Energy balance and loss path in the energy conversion process.

In the process of energy conversion, either efficiency η_i or loss μ_i can be calculated by first law of thermodynamics (Eq. 1-1).

$$\eta_i \text{ or } \mu_i = \frac{\text{energy input (energy stream i)}}{\text{energy output}} \qquad \text{Eq. 1-1}$$

It can be known by calculation that the energy loss has a share of 51% for industrial, 60% for commercial, 49% for residential and 81% for transportation sector (Figure 1-1). For the electricity generation sector with the largest energy loss, if 1% of the waste heat in the energy conversion process can be recovered (a practical waste heat harvest target), then 3.7×10^{11} kWh of electric energy can be recycled for direct use or storage. Recent studies have also confirmed that it is feasible and necessary to effectively harvest waste heat to improve energy conversion efficiency.[10]–[12]

However, the challenge in harvesting waste heat is that it happens in different ways and under different circumstances. The factors involved include the temperature range, the continuity of waste heat, and the form of heat transfer (radiation, convection, or conduction). Among them, the most important factor that affects whether waste heat can be practically harvested is its temperature range or 'quality'.[13] The other two factors also affect the complexity or cost-effectiveness of waste heat harvesting. The quality of heat is a characteristic of its ability to work or usefulness. As explained by Carnot efficiency, the efficiency of thermal processing production is directly proportional to the temperature difference.[14] A higher temperature leads to a higher temperature difference and is therefore classified as a higher quality heat source. As shown in Table 1-1, thermal quality can be classified.

Table 1-1. Thermal energy grades. [13]

High quality	923 K (650 °C) and above
Medium quality	503 K (230 °C) – 923 K (650 °C)
Low quality	393 K (120 °C) – 503 K (230 °C)
Ultra-low quality	less than 393 K (120 °C).

Theoretically, the higher the grade of waste heat, the easier it is to harvest with high efficiency. However, ultra-low-quality waste heat below 100°C is considered the most fertile field for research and development. Based on the statistical data of the above-mentioned world energy consumption process chain, the researchers investigated the temperature distribution of waste heat in various sectors (Figure 1-3).[2] All sectors, especially the commercial sector, show relatively large amounts of ultra-low-quality waste heat (<100 °C). As for the residential sector and power generation, there is no high-quality waste heat (≥300 °C). The transportation sector does not generate low-quality and medium-quality waste heat (100–299 °C). Overall, the proportion of ultra-low-grade waste heat is 63%. In addition, low-quality waste heat not only exists in the conversion process of primary energy, but also exists in a large amount in a widely form. For example, the human body is an important source of low-quality waste heat, which is responsible for the continuous production of heat through metabolic functions[15]. The human body releases about 100-525 W of heat, which is

continuous and widespread[16]. Depending on the practical use situation, these widespread waste heat still have a high harvest value.

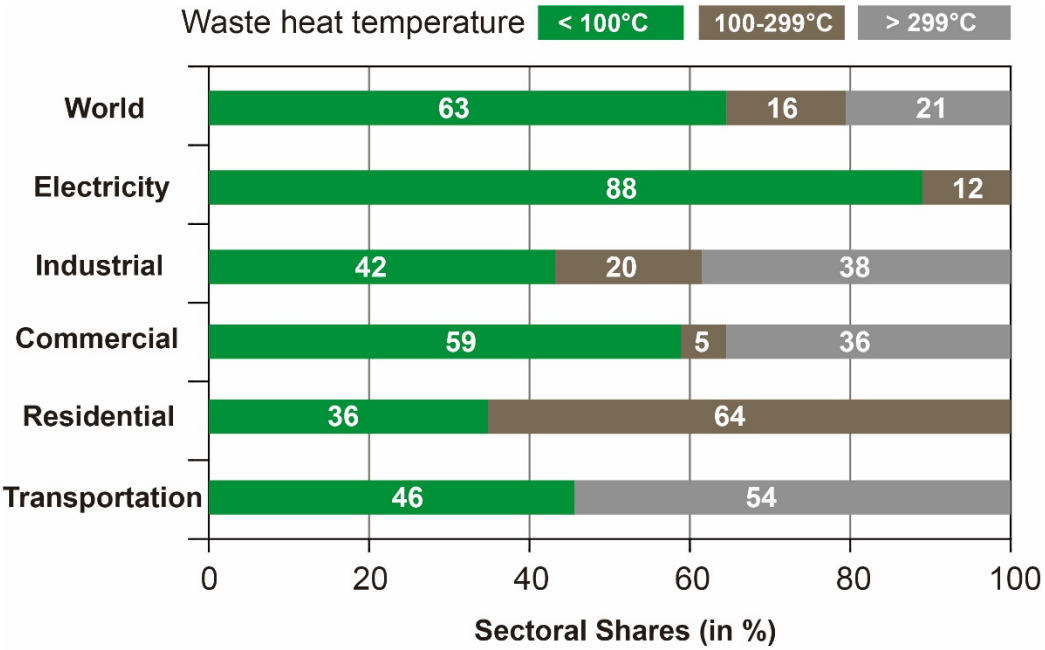

Figure 1-3. Sectoral shares of waste heat distribution in world energy consumption.

The most economical and practical waste heat recovery is for preheating.[11] The waste heat in the high temperature range can be used for mechanical power, while the thermal energy in low temperature range is usually used for water heating or space heating processes. However, this harvesting method requires specific facilities to be set up depending on the environment. It is more desirable to convert thermal energy into electrical energy that is easier to store and use. Currently, a variety of methods can be used to perform electrical energy generation from high-quality waste heat. Mainstream technologies include thermal cycle[17], turbine power generation[18] and external

combustion gas turbine[19]. Among them, thermal power cycles, such as the Rankine cycle (RC), Kalina cycle, and inverted Brayton cycle (IBC), treat the working fluid as an energy carrier and use waste heat to convert the working fluid from liquid to gas.[12] The highest efficiency of harvesting high-quality waste heat and medium-quality waste heat using these methods can reach 25.3% and 38.2%, respectively.[12] However, these methods are completely inapplicable or extremely inefficient for low-quality waste heat.[4],[5] Therefore, the development of a universal and efficient technology for converting low-quality waste heat into electrical energy is highly required (Figure 1-4).

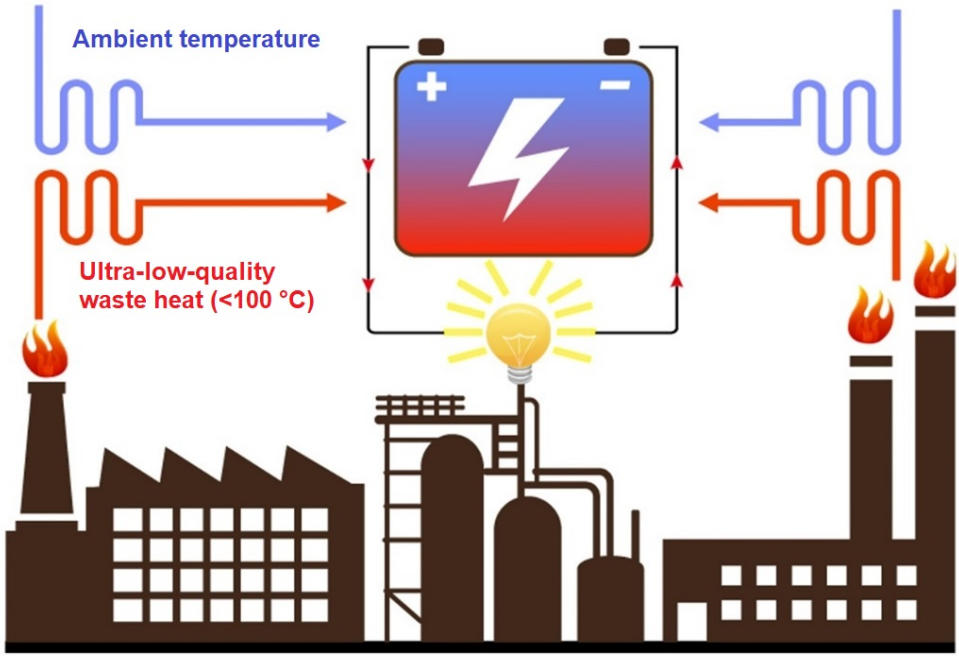

Figure 1-4. Energy loss recycling of converting waste heat into electrical energy

Waste heat emission reduction is conducive to the development of a harmonious society and promotes the adjustment of economic structure and the transformation of growth patterns. It is an inevitable choice to establish a resource-saving and environment-friendly society.[9],[20] Furthermore, the widespread waste heat is a kind of renewable energy, which is essential for the promotion of sustainable development goals (SDGs). Its potential as an alternative source of electricity is considerable.[3] At present, there are still unprecedented challenges in the research of multiple fields related to high-efficiency waste heat harvesting. To carry out thermoelectric conversion for the vast and huge global waste heat potential, and to make it practical and commercial, it is necessary to effectively harvest the ultra-low-quality waste heat, which accounts for the highest proportion. Therefore, it is very important to develop a novel and environmentally friendly solution for converting low temperature range thermal energy into electrical energy.

1.1.2. Thermoelectric conversion techniques

Thermal energy and electricity are two forms of energy at opposite ends of a spectrum. Thermal energy is ubiquitous, but the quality is low, whereas electricity is versatile, but its generation is demanding. Different from using thermodynamic machines to convert thermal energy into mechanical energy (Rankine cycles), the direct conversion process from thermal energy to electrical energy is called thermoelectric conversion. From a thermodynamic point of view, the conversion of low-grade energy (waste heat) to high-grade energy (electric energy) is difficult. Its limit efficiency (Carnot efficiency) can be confirmed by the theory of thermodynamics.[5],[14] However, with continuous advancements in scientific research, many effective and feasible waste heat harvesting measures have been established. These are briefly described in the following and summarized in Table 1-2.

Thermophotovoltaic System (TPV). It is the direct conversion process from heat to electricity via emitted photons. A typical thermophotovoltaic system consists of a thermal emitter and a photovoltaic diode cell[21]. It is mainly used to harvest waste heat in the form of high-temperature radiation. However, due to the need for auxiliary devices such as transmitters and filters, a large amount of optical energy loss occurs in the process. Moreover, as the temperature of the heat source decreases, the radiant energy emitted to the TPV battery will be greatly reduced[22]. Therefore, this technology is difficult to recover low and ultra-low-quality waste heat.

Thermionic Generation (TIG). It is a more direct method in which electrons are released from the electrodes due to high temperature to generate electrical energy. It has attracted much attention due to its simplicity and compactness. However, ordinary metal cathodes cannot produce sufficient electron emission.[23] Therefore, this technology most of the time requires the use of expensive electrode materials and maintains the operation in a vacuum state.[24] This brings a lot of inconvenience to its practical application.

Thermoelectric Generation (TEG). This technology is based on the characteristics of semiconductors, which generate electric potential due to temperature differences (Seebeck effect).[25] TEG materials are currently commercialized and can be integrated into a variety of thermoelectric conversion systems. It can harvest a wide range of waste heat, while the recovery efficiency for low and ultra-low-quality waste heat is extremely low.[26]

Pyroelectric Generation (PEG). It can use nano-structured pyroelectric materials to convert external temperature change over time into electrical energy. Unlike TEG, where a stable and continuous spatial temperature gradient is needed, this technology allows to displace electrical charges from temporal temperature changes by using a suitable material or device.[11] The efficiency and output power can be much larger by using PEG than TEG methods. A research shows it may reach an efficiency up to 50% of Carnot efficiency.[27] However, PEG also requires the use of expensive semiconductor materials, and its power capacity needs to be improved.[28]

Osmotic Heat Engine (OHE). This technology uses thermal energy to control the osmosis process to convert salinity gradients into electrical energy. Literature studies have shown that using a mixture of volatile ammonia and carbon dioxide and adopting heat at a temperature of 50°C can produce a power density of more than 200 W/m^2.[29] This technology is suitable for the recovery of large-scale ultra-low-quality waste heat. However, its permeable membrane system and heat exchange equipment require high costs.[30] Similar technologies include Pressure-retarded osmosis (PRO)[31] and Reverse electrodialysis technology (RED)[32], which also face the same problem of high device cost.

Thermally Recharged Battery (TRB). The TRB is a kind of flow battery fed by solutions which can be regenerated by utilizing a thermal process when exhausted. The method of organic solvent distillation is usually used to regenerate the electrolyte of the flow battery.[33] This technology has several advantages, such as a simple and easy-to-expandable device, and only requires relatively inexpensive reactants and electrode materials.[34] However, the maintenance cost of the device and the risk of toxic solvent leakage have become obstacles to its widespread practical use.[35]

Thermocell or Thermo-electrochemical Cell (TEC). Thermocells are batteries constructed with the same electrochemical redox pair on both electrodes and operate at different temperatures. When a thermal gradient is applied, the thermocell can continuously generate electricity without generating emissions or consuming any materials.[36] The electric energy produced by this technology per unit thermal gradient

depends on the entropy change of the redox reaction.[37] This simple setup and the use of inexpensive materials have stimulated its application in ultra-low-quality waste heat harvesting.

Table 1-2. Current technologies to directly convert waste heat to electricity.

Technology	**Typical sources of waste heat**	**Ref**
Thermophotovoltaic System (TPV)	High-quality waste heat. Heat source above a certain temperature is required to generate photons.	[38]
Thermionic Generation (TIG)	High-quality waste heat. Heat source above a certain temperature is required to generate electrons.	[39]
Thermoelectric Generation (TEG)	Medium and high-quality waste heat. A stable and continuous heat source is required to maintain the temperature gradient.	[40]
Pyroelectric Generation (PEG)	Medium and high-quality waste heat. The change of heat source over time is required.	[27]
Osmotic Heat Engine (OHE)	Low and Ultra-low-quality waste heat. High input is required for water and organic solute vaporization.	[29]
Thermally Recharged Battery (TRB)	Low and Ultra-low-quality waste heat. High input is required for distillation process.	[34]
Thermocells /Thermo-electrochemical Cells (TEC)	Low and Ultra-low-quality waste heat. A stable and continuous heat source is required to maintain the temperature gradient.	[36]

Among all the technologies mentioned above, TEG and Thermocell have the greatest potential for commercialization and practicality. This is because they can efficiently convert a stable and continuous temperature gradient into electrical energy without generating any emissions.[33],[40] Moreover, as discussed above, the difficulty in harvesting waste heat is that thermal energy exists in a wide range of forms and usually in different environments. The devices of these two technologies are relatively simple and small[41],[42], which greatly expands their application directions. The following describes the development, mechanism, and performance evaluation of TEG. The introduction of Thermocells will be detailed in the next section of this chapter.

As the biggest competitor of this research, TEG is the simplest technology applicable to achieve the direct heat-to-electricity energy conversion.[43]–[45] The basic principle of the TEG is based on the concept of the Seebeck effect of thermoelectric materials discovered in the early 20th century. The generated open-circuit voltage V_{OC} (V) of TEG is directly proportional to the temperature gradient as shown mathematically below[46]:

$$V_{OC} = S_e \Delta T \qquad \text{Eq. 1-2}$$

Where S_e is the Seebeck coefficient (V K^{-1}) of the TEG materials and ΔT is the temperature difference. The TEG system is a solid-state device composed of *p*-type and *n*-type semiconductors, where the *p*-type has excess holes and the *n*-type has excess electrons to carry current (Figure 1-5). When heat flows from the hot surface to the cold surface through the TEG material, the free charge (electrons and holes) of the

semiconductor moves. This charge movement converts thermal energy into electrical energy. This is called the Seebeck effect[47]. This effect stems from the material's ability to generate current when subjected to a temperature gradient. The Seebeck coefficient, S_e, is a non-linear function of temperature and is specific to each different material and crystal structure[48]. Among standard TEG modules, semiconductors composed of tellurium (Te), bismuth (Bi), antimony (Sb) or selenium (Se) have always been the most widely used carrier materials.[49] The Seebeck coefficient largely depends on the effective mass and mobility of carriers. The typical Seebeck coefficient of commercially available n-type bismuth telluride (Bi_2Te_3) is -150 $\mu V\ K^{-1}$, while p-type antimony telluride (Sb_2Te_3) is 101–161 $\mu V\ K^{-1}$ at room temperature.[50],[51]

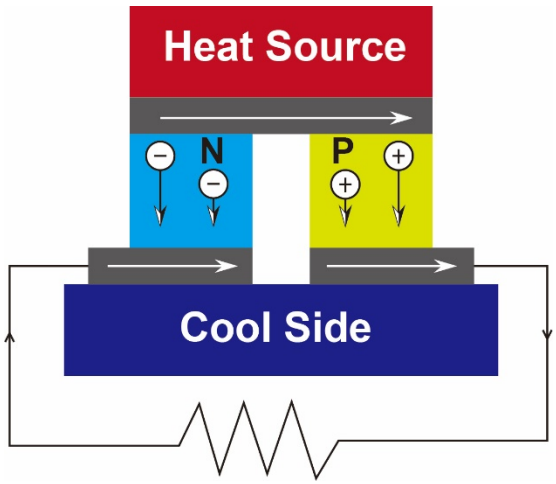

Figure 1-5. A TEG device with *n*-type and *p*-type semiconductors electrically in series and thermally in parallel.

Typically, commercial TEG devices consist of multiple modules are electrically connected in series and thermally connected in parallel to increase the output power (Figure 1-6).[16] This can be used to compensate for the low voltage generated by a single TEG module because it is able to generate n times the output voltage (if n is the number of TEG modules in series) and a maximum electrical output power. Hsu et al. invented a TEG system for automobile exhaust heat recovery. The system consists of 24 TEG modules and can provide ≈12W of electric power at $\Delta T = 30°C$.[52] Sano et al. used a similar method to develop a very efficient multiple module (with a relative efficiency of 15%).[53]

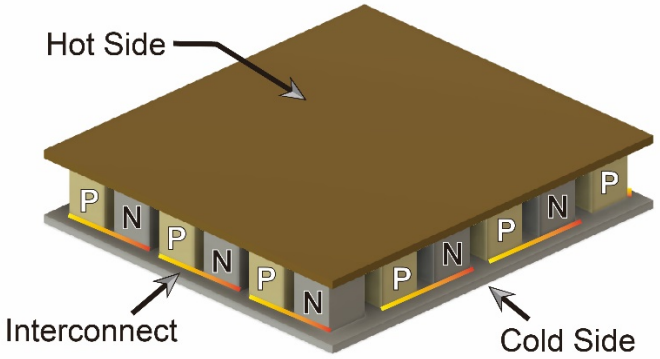

Figure 1-6. Multiple TEG modules converting the thermal energy flow existing between hot and cold junction into electrical energy.

Although there are many indicators to evaluate the capacity of TEG materials in harvesting waste heat and converting them into electrical energy, the most important

parameter is the dimensionless figure of merit, ZT.[54] It can help us determine the efficiency of thermoelectric conversion, and it is also applicable to other thermoelectric conversion technologies.[55] The maximum power-generation efficiency of a TEG material, η, is defined as the output of electrical energy (P) divided by the thermal energy (Q) supplied, as expressed:

$$\eta = \frac{P}{Q} = \left(\frac{T_{hot}-T_{cold}}{T_{hot}}\right)\left[\frac{\sqrt{1+ZT_m}-1}{\sqrt{1+ZT_m}+\frac{T_{cold}}{T_m}}\right] \quad \text{Eq. 1-3}$$

where T_{hot} and T_{cold} are referred to temperatures of hot, cold sides of the TEG, and T_m is the average temperature, respectively. Carnot efficiency is the ratio of the temperature difference between the hot side and the cold side ($T_{hot} - T_{cold}$) to T_{hot}. The coefficient of performance for TEG refrigeration adopts a slightly different expression, which depends on thermoelectric properties of materials through the figure of merit, ZT. The definition of ZT is:

$$ZT = \frac{\sigma S_e^2}{\kappa} T \quad \text{Eq. 1-4}$$

The ZT is determined by Seebeck coefficient (S_e), as well as the electrical conductivity (σ), absolute temperature (T), and thermal conductivity (k). The S_e value is positive for p-type (hole) conduction and negative for n-type (electron) conduction. The product of $S_e{}^2\sigma$ is usually referred to as the power factor. Note that the ZT_m in Eq. 1-3 is the average value of ZT between T_{hot} and T_{cold}, whereas the T in Eq. 1-4 refers to a specific temperature. Generally, a higher ZT will result in a higher conversion efficiency. From an efficiency point of view, a ZT_m value ~2 to 4 is needed for a TEG

device to be a competitor with other thermoelectric conversion technologies.[56] Although many materials have been studied in the past 40 years, according to Wiedemann-Franz law, due to the strong interdependence between the three parameters of electrical conductivity, thermal conductivity and Seebeck coefficient.[57] An increase in electrical conductivity will result in an increase in thermal conductivity. However, an increase in conductivity will also result in a decrease in Seebeck coefficient. Therefore, the efficiency of TEG devices has not yet been improved (Figure 1-7). To date, no TEG material has reached the target goal of $ZT \geq 3$.[58]

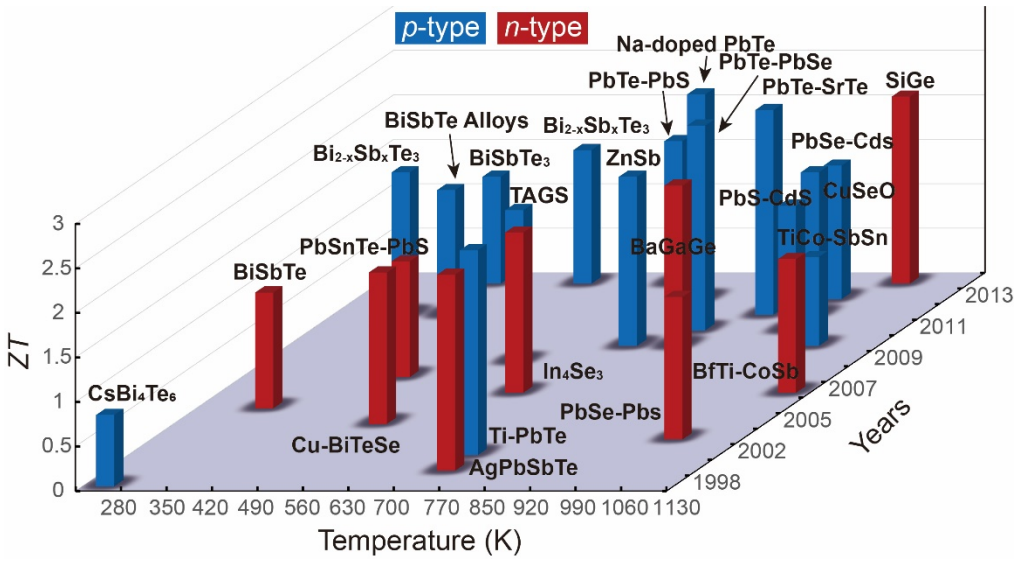

Figure 1-7. Dimensionless thermoelectric figure of merit, *ZT*, as a function of operating temperature and time (years). Important milestones are illustrated, adapted from ref[40] with additional data.

Through research on the latest TEG technology, there are few practical examples of high-efficiency TEG devices in the temperature range of low and ultra-low quality waste heat. A summary of literature reviewed on low and ultra-low-quality waste heat TEGs is presented in Table 1-3. All of its *ZT* is lower than 1, and the voltage generated by a single TEG module is very low under a considerable temperature difference near the ambient temperature.

Table 1-3. Summary of the TEG review papers at low and ultra-low quality waste heat temperature range.

TEG Materials	**Number of modules**	**Temperature difference (K)**	**Voltage**	**Power**	**Ref**
$Bi_{0.4}Te_{3.0}Sb_{1.6}$	7	30	83.3 mV	0.21 μW	[59]
Ni-Ag	7	6.6	0.9 mV	2 nW	[60]
$Bi_{0.5}Sb_{1.5}Te_3$	1	50	30 mV	0.06 μW	[61]
Bi_2Te_3 and Sb_2Te_3	100	15	160 mV	4.18 nW	[62]
Bi_2Te_3	8	19	7 mV	2.1 μW	[63]
Si micro-wires	34	54	9.3 mV	N/A	[64]
ZnO and Zn-Sb	10	180	460 mV	246 μW	[65]

Most single TEG near ambient temperature produce voltage in the mV range and generate output power in the μW range or less. Therefore, harvesting sufficient energy from low-quality waste heat to generate electricity has become a challenge. Researchers have found that the ZT of TEG materials is 2.5 at 300 °C, but drops below 0.4 at low temperatures (for example, 27 °C).[66] The efficiency comparison of TEGs and other thremoelectric conversion technologies as a function of the thermal energy source temperature is shown in Figure 1-8[67]. The *ZT* values are assumed to be temperature independent, and the cooling source temperature is set at ambient temperature.

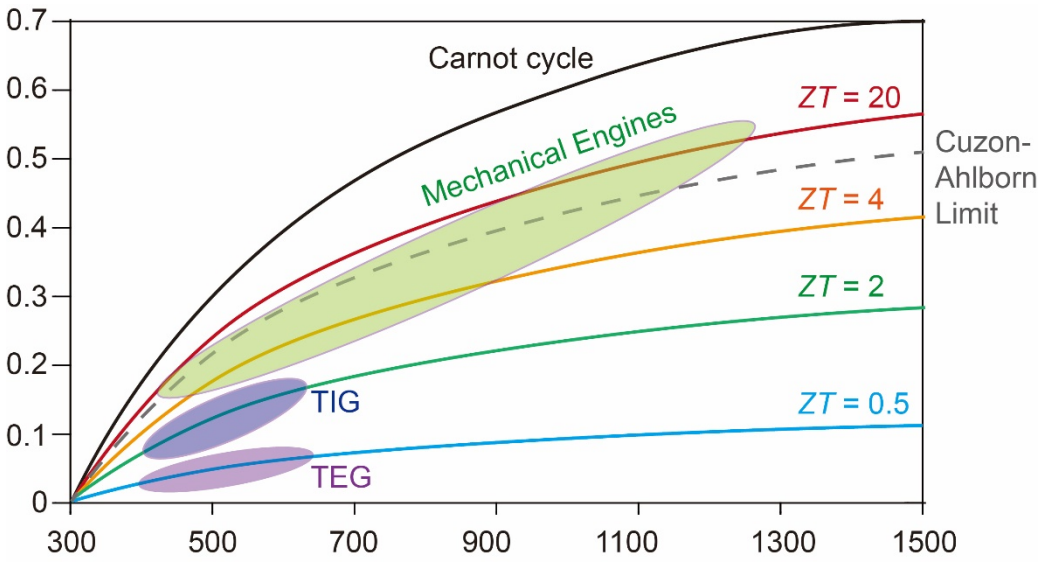

Figure 1-8. Thermoelectric power generation efficiency versus T_{hot} (T_{cold} = 300 K). Efficiency for conventional thermoelectric mechanical engines as well as the Carnot efficiency limit and the Curzon-Ahlborn efficiency limit are also shown.[68],[69]

The TEG device does not show high-efficiency thermoelectric conversion under the low temperature difference near the ambient temperature. Besides, the research on practical TEG device still faces many limitations in recent years. Limitations exist in the TEG researching field can be summarized as:

• It is still problematic to achieve higher *ZT* at temperatures less than 150 °C.[41]

• TEG materials costing is high ($7 to $42 per Watt), while the efficiency is comparatively low even for harvesting high-quality waste heat.(6-8%).[70]

• Semiconductor materials of TEG containing Bi, Te, and Sb are toxic and are relatively scarce rare earth elements. The silicides, polycrystalline iron disilicide, cobalt monosilicide, etc., which are substituted for TEG materials, have low efficiency.[71]

• The flexibility of TEG materials is insufficient. Commercially available devices with rigid plates cannot effectively collect thermal energy on uneven surfaces.[72]

In summary, TEG is the closest to commercialization and practicality among many thermoelectric conversion technologies. However, there are many shortcomings and limitations in the direction of low-quality waste heat harvesting with broader application prospects. It is necessary to find alternative technologies that are more efficient, safer, and scalable.[45] Recently, researchers have been trying to use thermocells instead of TEG materials to improve the efficiency of power generation and expand its application in the field of low-quality waste heat harvesting.[73]

1.2. Thermocell

As mentioned above, among thermoelectric conversion strategies, the solid-state TEG have been studied extensively in recent decades and show high efficiency for harvesting high-quality waste heat.[41] However, harvesting low-quality heat by using TEG has been hindered by their high cost and the limitations of simiconductor materials with toxic or rare elements.[26] Thermocells, also called thermo-electrochemical cells or thermo-galvanic cells (TEC), have huge potential for thermoelectrical energy conversion.[74],[75]

A thermocell is a non-isothermal electrochemical cell in which two electrodes are deliberately kept at different temperatures (Figure 1-9).[76] The two electrodes are in contact with the electrolyte containing the redox chemical species and connected to an external circuit. Even though the same electrode is used and immersed in the same concentration of the redox species solution, the temperature difference can produce a potential difference. This is due to the temperature dependence of the redox reaction.[42] When a temperature gradient is applied across the cell, the redox species are oxidized at the anode and reduced at the cathode. The flow of current in thermocells is continuous. This is beacause the reduced species are transported to the anode where they are oxidized by convection, diffusion and migration in electrolyte, and then the oxidized species are transported back to the cathode to produce a continuous reaction. As long as the components of thermocells are not degraded, the cell reaction can theoretically produce electrical energy indefinitely.

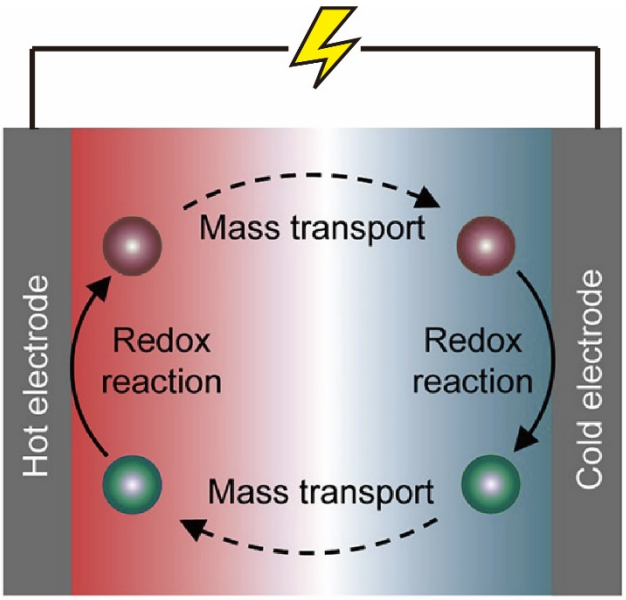

Figure 1-9. Schematic of a typical thermocell driven by redox reaction and redox species mass transportation.

A continuous thermo-voltage generated by thermocell is based on the temperature dependent change of solvent entropy. The capacity can be defined as thermogalvanic coefficient. This can also be defined as Seebeck coefficient in a broad sense because they are both used to describe the voltage produced by per unit temperature difference, although the mechanism is different.[77] The coefficent is expressed by[42],[78]:

$$S_e = \frac{\partial E}{\partial T} = \Delta E \cdot \frac{1}{nF} = \frac{[(S_B + \hat{S}_B) - (S_A + \hat{S}_A)]}{nF} \qquad \text{Eq. 1-5}$$

where E is the electrical potential, n is the electrons transfer number, F is Faraday's constant, S_A and S_B are the partial molar entropies of redox species A and B, respectively, $\hat{S}_A$ and $\hat{S}_B$ are their Eastman entropies.[73] The Eastman entropy of redox species is

attributed to the interaction of ions (and their solvation shells) with the electrolyte solution. In most cases, this value can be ignored. As such, Eq. 1-5 can be written as:

$$S_e = \frac{\Delta V}{\Delta T} = \frac{S_B - S_A}{nF} \qquad \text{Eq. 1-6}$$

Theoretically, the voltage generated by thermocells will increase as the Seebeck coefficient increases, thereby improve the current produced. However, during operation, the maximum electrical power output of thermocells is limited by three main sources of overpotential, including ohmic overpotential, charge transfer overpotential and mass transfer overpotential. These overpotentials come from the internal resistance of the cell, the kinetic process of charge transfer, and the diffusion of substances in the electrolyte solution including diffusion, migration and convection. This results in the actual maximum electrical power output that cannot be determined by the capacity of the voltage generated by the thermocells. Therefore, the performance of a certain thermocell cannot be determined based on the Seebeck coefficient solely.

One factor describing the performance of thermocells is energy conversion efficiency. The energy conversion efficiency (η) of a thermocell is defined as the ratio of maximum electrical power output (P_{max}) from the cell to thermal power flowing through the cell[79]:

$$\eta = \frac{P_{max}}{Q} = \frac{V_{OC} \cdot I_{SC}}{4} \cdot \frac{1}{A \cdot \kappa \left(\Delta T / d\right)} \qquad \text{Eq. 1-7}$$

where V_{oc} and I_{sc} are the open-circuit voltage and the short-circuit current, respectively, κ is the thermal conductivity of electrolyte solution, A is the cross-

sectional area of the cell, ΔT is the absolute temperature difference between hot and cold electrodes, and d is the electrode separation distance.

The current-potential relationship (I-V) of an ideal electrochemical device will be square, and the maximum current can be obtained with the minimum voltage loss. However, like the overpotentials come from the internal resistance, the kinetic process, and the mass-transport, most published thermocells are dominated by a limiting resistance and follow a V = IR relationship (Figure 1-10).[80] The P_{max} achieved at 0.5 V_{oc} and 0.5 I_{sc}.

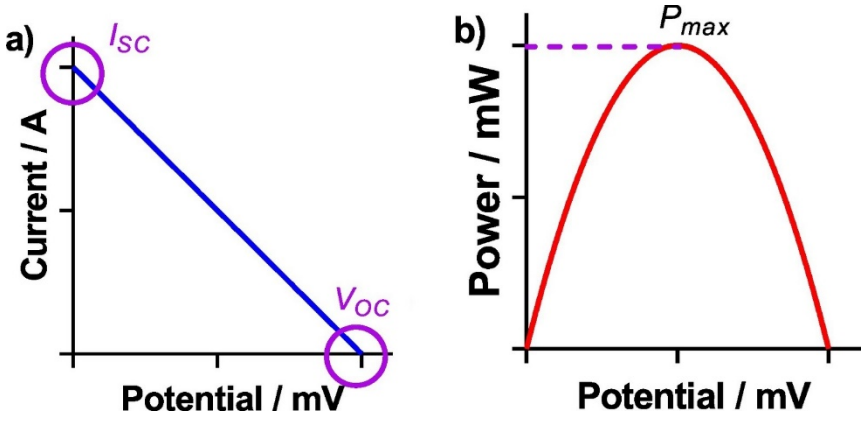

Figure 1-10. Simulated (a) I-V data and (b) P-V data displaying the performance of a thermocell.

Applying the relationships from Eq. 1-6, $V_{oc} = S_e \Delta T$ and $I_{sc} = S_e \Delta T / R_{cell}$, to Eq. 1-7, where S_e is the Seebeck coefficient, R_{cell} is the internal resistance of the thermocell, leads to the following equation:

$$\eta = \frac{S_e^2 \cdot \Delta T}{4\kappa} \cdot \frac{d}{A \cdot R_{cell}} \qquad \text{Eq. 1-8}$$

The theoretical energy conversion efficiency relative to Carnot efficiency (η_r) can be expressed by the following equation, when Eq. 1-8 is divided by the Carnot efficiency ($\eta_c = \Delta T/T_{hot}$):

$$\eta_r = \frac{S_e^2 \cdot T_{hot}}{4\kappa} \cdot \frac{d}{A \cdot R_{cell}} = \frac{S_e^2 \cdot T_H}{4\kappa} \cdot \sigma_{\text{eff}} \qquad \text{Eq. 1-9}$$

where T_{hot} is referred to temperatures of the thermocell hot side, σ_{eff} represents the effective conductivity in thermocell, analogous to the electrical conductivity in TEG. For an ideal thermocell system, the effective conductivity can approximate the ionic conductivity of the electrolyte; for an actual device, it can be evaluated from the internal resistance of the cell.[81]

Similar to TEG, thermal gradient is an important factor in the performance of thermocells. An electrolyte with high thermal conductivity limits the ΔT that can be kept between the electrodes, and a decreased temperature gradient will reduce the potential of the thermocell. Therefore, the dimensionless figure of merit ZT mentioned in TEG (Eq. 1-4) can be used as another factor to describe the performance of thermocells.[42]

As mentioned in the previous section, the ZT value of solid-state TEG devices at ambient temperature is lower than 1. However, this figure of merit cannot be directly applied to thermocells, because the effective conductivity of thermocells is not the only transportation property that affects its performance. The actual transport process is

limited by the diffusion and concentration of active redox species. Therefore, the *ZT* of thermocells tends to be smaller than that of TEG.[42] However, a cross-strategy comparison of *ZT* cannot be used to conclude that the thermoelectric capacity of a thermocell is lower than that of a TEG material. We need to combine the two factors of η_r and *ZT* to evaluate the performance of thermocell.

1.2.1. Liquid-state thermocell

Most research on thermocells has focused on liquid-state thermocells (LTC).[73] This is due to the well-known strong interdependence of S_e, electrical conductivity, and thermal conductivity in solid TEG materials as mentioned above (Eq. 1-4). This is especially problematic for the development of low cost materials free of rare earth elements.[41] Alternatively, LTCs offer more methods to decouple the interdependence of S_e, electrical conductivity, and thermal conductivity.[36] Furthermore, a design of LTC are also required because of low cost, scalable and their potential of high η_r and *ZT* at the temperature around physiological temperature to efficiently harvest ultra-low quality waste heat.[82]

1.2.1.1. Aqueous thermocell

A pristine LTC in aqueous solution consists of two electrodes and electrolyte containing a water-soluble redox species. The electrodes and electrolyte of an aqueous

thermocell are readily available and do not require complex manufacturing. Typically, an aqueous thermocell containing the ferri/ferrocyanide redox species ($Fe(CN)_6^{3-}/Fe(CN)_6^{4-}$) has a negative S_e of −1.4 mV K^{-1} from 0.05 to 0.2 M (Figure 1-11).[36] This is due to the oxidation occurs at the hot side electrode and the reduction undergoes at the cold side electrode (for a redox specie with a positive S_e, this procedure is reversed).

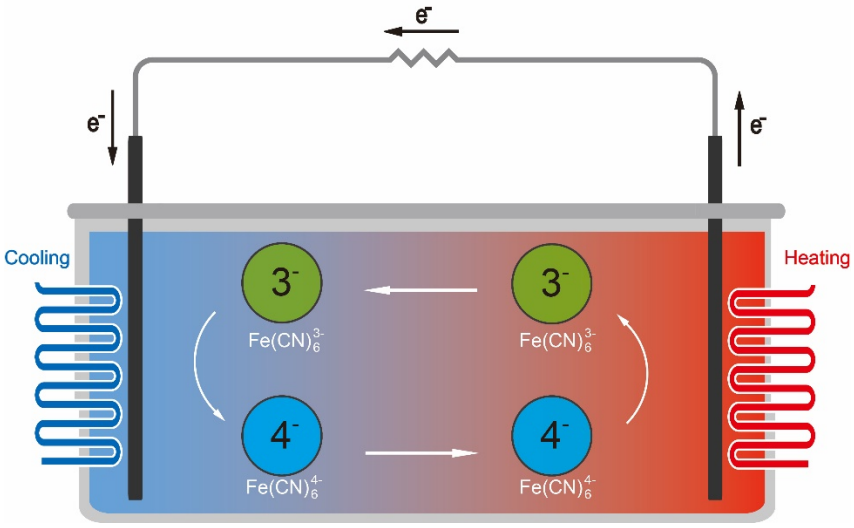

Figure 1-11. Schematic of an aqueous thermocell containing $Fe(CN)_6^{3-}/Fe(CN)_6^{4-}$.

Aqueous electrolyte solutions are mostly employed by LTCs due to the fast ion diffusion and the compatibility with many redox species. Therefore, aqueous thermocells generally exhibit higher power output. Futhermore, cell components based on aqueous electrolyte solutions have better safety and scalability, and can often be maintained at a lower cost. The researches on the performance improvement of aqueous

thermocells from the past to the present have mainly focused on redox species, electrode materials and engineering strategies.[42],[73]

1.2.1.1.1. Redox species of aqueous thermocells

As an important component of thermocells, redox species have been extensively investigated to improve their thermoelectric capacity and stability. As discussed, the maximum potential difference that can be generated in a thermocell is determined by the S_e of the redox species, which represents the entropy change that occurs when the species undergo a redox reaction (Eq. 1-5). The entropy change in this process includes the redox species structure represented by S, ionic solvation shell indicated by $\hat{S}$, and and transportation of electrons to electrodes. This can be analogous to the concept of *p*-type and *n*-type semiconductors in TEG, which can be defined as positive and negative according to the difference between absolute entropy changes by redox species in thermocells.[36] In addition, solubility and chemical reversibility in the aqueous solution are also important factors for selecting suitable redox species.

Intrinsic partial molar entropy of hydrated ions serves as a primitive criterion to screen suitable redox species in aqueous thermocells.[83] The ferri/ferrocyanide redox species mentioned above is the most widely used due to the considerable partial molar entropy change.[77] Another example is the iodide/triiodide (I^-/I^{3-}) redox species, which shows a positive S_e of 0.86 mV K^{-1}.[84]

The S_e of redox species exhibits electrolyte environmental dependence. Electrolyte additives can influence the thermoelectrochemical process. For example, by introducing α-cyclodextrin (α-CD) as a molecular host to the iodide/triiodide thermocell, α-cyclodextrin selectively interacted with the hydrophobic I^{3-} anion, that led to a significant improvement of S_e from 0.86 to 1.45 mV K^{-1}.[85] A recent work reported that the addition of strong chaotropic cations (guanidinium) and highly soluble amide derivatives (urea) as electrolyte additives to the ferri/ferrocyanide thermocell can induce the interaction with $Fe(CN)_6^{4-}$ ions at the cold side of the cell, that would synergistically enlarge the entropy difference. The decrease in the concentration of reducing species promotes the reaction to proceed towards the reduction reaction at the cold side of the cell and vice versa, thereby increasing the value of S_e from -1.4 to -4.2 mV K^{-1}.[86]

The common redox species used in aqueous thermocells and their combinations with electrolyte additives are summarized in Table 1-4. These redox species exhibit different S_e in different use conditions and cell designs, which makes it an important factor that directly affects the performance of aqueous thermocells.

Table 1-4. Seebeck coefficients of aqueous thermocells using various redox species with and without electrolyte additives.

Redox species	S_e (mV K^{-1})	*Ref*
$[Fe(CN)_6]^{3-/4-}$	-1.40	[87]
$[Fe(CN)_6]^{3-/4-}$ (guanidinium/urea)	-4.2	[86]
I^-/I^{3-}	0.86	[88]
I^-/I^{3-} (α-CD)	1.45	[85]
I^-/I^{3-} (Me_{18}-α-CD + KCl)	1.90	[89]
Fe^{2+}/Fe^{3+}	1.76	[90]
Quinhydrone	-0.63	[91]
$Co^{2+/3+}(py\text{-}pz)_3$	2.36	[92]
$[Ru(Hxim)_6]^{2+/3+}$ (Him=imidazole, x=0≈1)	-3.7	[93]

1.2.1.1.2. Electrodes of aqueous thermocells

As in other electrochemical techniques, whether the electrodes used in thermocells can achieve high current density is a key challenge that directly affects the thermoelectric conversion efficiency of the cell.[73] In most aqueous thermocells research, noble metal electrodes (such as Pt or Ni) are wiedely used because their high catalytic activity can minimize the charge transfer overpotential.[36] However, the high cost of noble metal electrodes hinders the commercial application of thermocells. In

addition, noble metals need to undergo complex surface treatment before actual use of the electrode in order to exert its best performance, which also increases the maintenance cost of the electrode in disguise.[77],[80] Carbon materials are gaining prominence as a prospective, cheaper alternative to noble metals. Nanotubes and graphene with nano-structures have high effective surface area that can increase the amount of reaction sites. The porous surface of the carbon electrode can be seen through the scanning electron microscope (SEM) image (Figure 1-12a and Figure 1-12b). For most commonly used redox species, carbon electrodes can also achieve fast electron transfer kinetics.[94] Both of these characteristics can increase the current density available from the aqueous thermocell and thus increase the thermoelectric conversion efficiency. In addition, the wide range of manufacturing methods that can be used to produce nanostructured carbon means that electrodes can be produced in a variety of useful forms. Most of the research in this field has focused on the composite material which incorporate nano-structured carbon materials such as nanotubes and graphene[79],[95], and additional treatment via additives[96] or doping[97]. Using these composite materials can provide rapid redox process, high thermal conductivity and high electrical conductivity, and high weight specific surface area. In the early research, bucky paper of multi-walled carbon nanotubes (MWCNT) was used as the electrode of aqueous thermocells. The output power of the MWNT-bucky paper tested under the same conditions is 33% higher than that of the platinum electrode.[79] Im et al. reported that the use of carbon nanotube aerogel sheet electrodes can further improve the performance of the cell, achieving a Carnot relative efficiency of 3.95% at a

temperature difference of 51 °C with $Fe(CN)_6^{3-}/Fe(CN)_6^{4-}$ redox species.[96] When using carbon electrodes and platinum electrodes, the maximum output density that can be achieved by the aqueous thermocells containing $Fe(CN)_6^{3-}/Fe(CN)_6^{4-}$ redox species is summarized in Figure 1-12c.

(a)

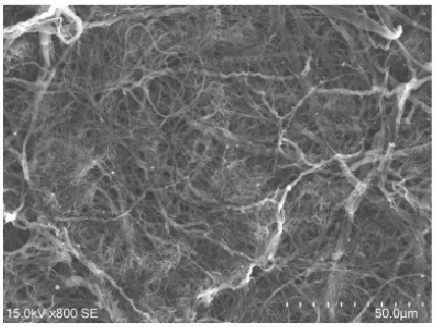

(b)

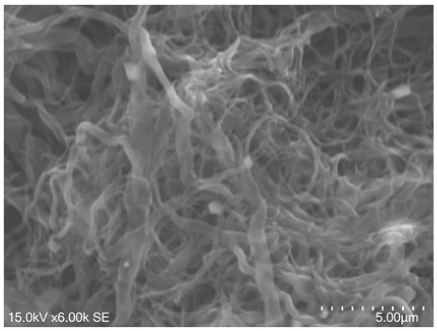

(c)

Electrode material	P_{max} (W m^{-2})	$P_{max}/(\Delta T)^2$ (mW K^{-2} m^{-2})
Activated carbon cloth	12.0	1.80
MWNT foam	9.3	1.35
C-cork (pressed)	8.6	1.15
Graphene sheet	5.8	0.78
MWNT sheet	4.2	0.59
Platinum foil	11.0	1.38
MWNT sheet	1.8	0.5
Platinum electrode	3.2	1.28

Figure 1-12. (a) Low- and (b) high-resolution SEM images of a carbon nanotube (CNT) electrode. (c) Summary of P_{max} and $P_{max}/(\Delta T)^2$ for different carbon electrode materials when using 0.9 M $Fe(CN)_6^{3-}/Fe(CN)_6^{4-}$ redox species. Data taken from Ref.[79],[94],[96],[98]

Unlike rigid metallic electrode materials, carbon-based electrodes can be made into flexible thin films and has a long service life. Therefore, carbon-based electrodes are feasible for working in tandem with waste heat recovery from uneven surfaces such as in wearable devices.[99] However, although these electrodes are described as potentially low-cost, the relatively complex manufacturing process may need to be simplified to make these electrodes commercially viable.

1.2.1.1.3. Engineering strategies for higher-performance aqueous thermocells

As discussed earlier, since the substances that are electron carriers in aqueous thermocells move in the aqueous solution, they are affected by the related parameters of substance diffusion and mass transfer.

Due to the temperature difference, there is thermal convection in the aqueous thermocells. Therefore, the cell direction and electrode spacing in the cell design will greatly affect the performance. The mass transfer of redox species through diffusion is relatively slow. However, it can be increased significantly by introducing convection into the system. The increase in natural convection homogenizes the concentration, resulting in a decrease in cell resistance, an increase in the mass transfer rate of the redox species to the electrode, and an increase in power output.[100] However, increasing convection will also increase the heat transfer rate of the entire cell. This results in the need for a larger input energy to maintain the thermal gradient, which reduces the conversion efficiency.[87] Therefore, suppressing or enhancing convection as needed,

and maintaining a balance between electrical conductivity and thermal conductivity are very important factors in the device design of aqueous thermcells.

The heat transfer can be reduced by adding a separation membrane in the cell between the electrodes, which can reduce the natural convection in the cell and maintain the temperature gradient. As reported, inserting a poly(vinylidene fluoride) (PVDF) separation membrane in a 0.7 M iodide/triiodide aqueous thermocell can greatly mitigate natural convection, increasing the open-circuit voltage from 1.3 to 2.8 mV at a temperature difference of 12°C.[101] For separation membranes inserted equidistantly from the hot electrode and the cold electrode, the best cell performance can be obtained. Infrared thermal imaging of the cell showed that for the film located in the middle between the hot electrode and the cold electrode, the largest thermal gradient can be achieved, which is related to the best cell performance. This is due to the natural convection on both sides of the separation membrane is minimized. This weakens the heat transfer process across the cell compared to placing the separation membrane closer to the hot or cold electrode.

Recently, the influence of separation membranes on $Fe(CN)_6^{3-}/Fe(CN)_6^{4-}$ aqueous thermocells have been systematically measured. By optimizing the position, thickness, and composition of the separation membrane, a highest power density to date of ~12 W m^{-2} was achieved by using a cotton separation membrane.[94]

Placing the separation membrane in a suitable position in the cell helps to maintain a stable temperature gradient, thus the power output can be maximized. However, the effect of the thickness of the separation membrane needs to be considered. The ion conductivity of the electrolyte-filled separation membrane is 30% lower than that of the pure electrolyte.[101] Therefore, it is found that increasing the thickness of the separation membrane will reduce the cell power performance due to the decrease in the ion diffusion speed.

Since the electrical conductivity and thermal conductivity of the aqueous electrolyte are positively correlated, the above-mentioned engineering strategy aims to find a balance point that is most suitable for the performance of the thermocell. Suppressing natural convection and inserting the separation membrane is beneficial to maintain the temperature gradient but at the same time reduces the effective conductivity, resulting in an increase in the internal resistance of the cell. Conversely, enhancing natural convection and reducing the distance between electrodes is beneficial to increase the effective conductivity and thus reduce the internal resistance of the cell, but the temperature gradient will be difficult to maintain due to the increase in thermal conductivity. This is similar to the coupling relationship between thermal conductivity and electrical conductivity in TEG, which is also a challenge for aqueous thermocells.

Overall, aqueous thermocells are the simplest, cheapest and most widely studied thermocells. They are a promising method for harvesting ultra-low quality waste heat of <100°C. Through the efforts of researchers, such as selecting the most suitable redox

species, using electrode materials with a larger effective area, and ingenious device design based on engineering strategies, the maximum power density of aqueous thermocells reached 12 W m^{-2}[94], the maximum *ZT* reached 0.12, and the highest Carnot's relative efficiency is 3.95%[96]. However, the low output power density per unit temperature and relatively low thermoelectric conversion efficiency of aqueous thermocells are still not enough to support their commercialization and practicality. The root cause of this is that the S_e of aqueous thermocells is not high enough (although it is relatively high compared to TEG materials). Research on the improvement of redox species in aqueous solutions has reached a plateau. Using additives to change the thermodynamic environment of the thermocell system, rather than simply improving the mass transfer performance of redox species may be a more promising direction.

1.2.1.2. Ion liquid thermocell

The low boiling point of water limits the working temperature of aqueous thermocells to be lower than 100°C. In order to expand its operating temperature range to harvest low-quality waste heat above 100°C, researchers are studying electrolytes with higher boiling points, such as ionic liquids. In addition to higher operating temperatures, another advantage of ionic liquids electrolytes is that they can be used to solvate redox species that are insoluble in water, or use redox species that are unstable in an aqueous environment in their oxidation or reduction states.[102],[103] Benefitting from the neglectable vapor pressure and high ionic conductivity of the ionic liquids, the

service lifetime and efficiency of thermocells can be improved, respectively.[104] In addition, the unique solvation environment provided by ionic liquids may cause the entropy of redox species to become larger during oxidation/reduction, resulting in a higher S_e.[105] Some ionic liquid structures and abbreviations that have been studied for thermocell applications are summarized (Figure 1-13).[36]

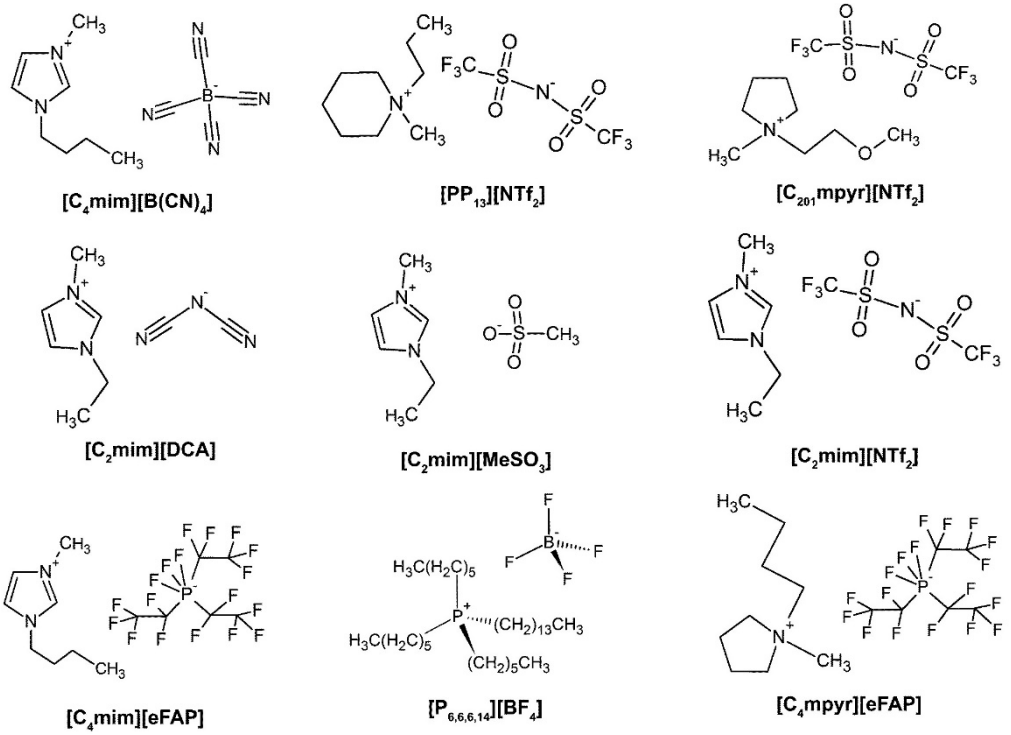

Figure 1-13. Structures of ionic liquid studied in thermocells.

Similar to aqueous thermocells, ionic liquid thermocells can also conduct performance studies through three aspects: redox species, electrodes, and engineering strategies.

Most of the inorganic redox species in aqueous solutions can be used in ionic liquids. For example, there are reports that a series of Co and Fe metal complex redox species ($Co^{2+/3+}(bpy)_3$ and $Fe^{2+/3+}(bpy)_3$) in [C_4mpyr][eFAP] can achieve a S_e of 0.45 mV K^{-1}.[106] Similar to the S_e in aqueous solution, $Fe(CN)_6^{3-}/Fe(CN)_6^{4-}$ redox species in [C_4mpyr][NTf_2] can obtain a S_e of -1.49 mV K^{-1}.[105] In addition, the researchers measured S_e in many Fe-based redox species in different ionic liquids. Although none of the reported values exceeds the maximum value obtained in aqueous solutions, some effects of different ionic liquid properties on S_e have been determined.[107],[108] The most important correlation factor is the ionic charge density of the ionic liquid. The increase in the charge density leads to an increase in the absolute value of S_e.[109]

There are relatively few researches on the electrode materials of ionic liquid thermocells. Researchers report that they have checked on a series of electrode materials including platinum, modified platinum electrodes (platinum black or PEDOT modified), stainless steel, etc.[110] The performance of $Fe^{2+/3+}(bpy)_3$ redox species in [C_2min][$B(CN)_4$] using these electrodes has been measured. Except for unmodified stainless steel, all electrodes showed higher power output values. This result is due to the difference in charge transfer resistance of the cell. This work shows that common electrode materials can be used in ionic liquid thermocells without sacrificing electrical power output. For $Co^{2+/3+}(bpy)_3$ ionic liquids thermocells, glass carbon electrode outperforms platinum electrode, leading to higher power density and lower separation of oxidation and reduction.[102]

The biggest challenge in achieving high thermocell performance with ionic liquid electrolytes is its high viscosity. In aqueous electrolytes, relatively slow charge transfer and higher internal resistance are power limiting factors. However, in ionic liquid electrolytes, due to the slow diffusion of redox ions, the mass transfer process has become a limiting factor.[111] To overcome this challenge, some engineering strategies have been applied to ionic liquid thermocells, such as the use of stirring to increase forced convection in addition to natural convection[112], or the addition of other organic solvents[113] to reduce electrolyte viscosity. However, the use of external energy for stirring will reduce the efficiency of energy conversion in a disguised form; the addition of organic solvents will greatly increase the maintenance cost and risk of ionic liquid thermocells.

In addition to the factor of the application temperature range, the advantage of ionic liquid thermocells lies in its relatively high electrical conductivity and the thermal conductivity that can be suppressed. However, due to the increase in electrolyte viscosity caused by it, overcoming the performance degradation caused by the slowing down of mass transfer is the main direction in the future. Another thing to mention is that due to the high cost of ionic liquids and auxiliary means, the possibility of commercialization and practicality has not yet been seen.

In summary, thermocells in liquid state are relatively simple and promising thermoelectric conversion technology. This technology may harvest and continuously convert low and ultra-low quality waste heat into electrical energy. As the starting point

of research in the thermocell field, it has attracted the attention of many researchers. The main challenges faced by LTCs are slowly revealed along with the progress of research. The most important of these is that its output power density and energy conversion efficiency cannot meet commercial applications. The fundamental reason lies in the following three aspects:

(1) LTCs use liquid electrolytes, resulting in relatively low conductivity of electrolytes. Even if ionic liquids are used at the expense of mass transfer efficiency, their conductivity is still somewhat different from other solid-state thermoelectric conversion materials. Low conductivity will increase the internal resistance of the battery, thereby affecting the performance of the output power.

(2) The redox species used in LTCs do not produce a high enough voltage per unit temperature (S_e is low). As discussed above, S_e theoretically comes from the entropy deterioration of the redox reaction at different temperatures, as well as other entropy deterioration caused by the electron transfer and mass transfer processes. The research on redox species tends to stagnate, and Fe-based redox species are used in most LTCs. The theoretical upper limit of S_e makes it impossible to increase the maximum open circuit voltage of a single LTC by effective means. It is necessary to improve S_e by focusing on other factors that can increase the entropy change in the cell.

(3) Liquid electrolyte has the risk of leakage in practical applications. Although this risk did not affect the evaluation of LTCs in the laboratory research stage. However, the application of LTCs is limited because of this shortcoming. For example, they are

difficult to use to recover waste heat generated by the human body to power wearable electronic devices unless other auxiliary measures are adopted[26],[73].

Faced with the above challenges, many non-liquid stete or non-completely liquid state thermocells have been extensively studied in recent years. And there are still researchers in the LTC field proposing new solutions to solve these problems.

1.2.2. Non-liquid-state thermocell

1.2.2.1. Quasi-solid state thermocell

As mentioned above, there are many potential thermocell applications that are not suitable for LTCs, especially those thermocell applications where electrolyte leakage may occur, such as the power supply of flexible and wearable devices. The development of quasi-solid state thermocells aims to solve this problem. Unlike the more brittle inorganic solids, quasi-solid state refer to the fact that they are usually a combination of solid organic polymer and liquid components and have the mechanical properties of a solid.

A quasi-solid state thermocell using $Fe(CN)_6^{3-}/Fe(CN)_6^{4-}$ redox species in poly(sodium acrylate) and polyvinyl alcohol electrolytes achieved S_e of -1.09 mV K^{-1} and -1.21 mV K^{-1}, respectively.[114],[115] Recently, a quasi-solid state thermocell composed of a cellulose polymer matrix and $Fe(CN)_6^{3-}/Fe(CN)_6^{4-}$ was also reported.[116] Compared with LTCs using same redox species, the power density and cell

performance of this quasi-solid state thermocell are not significantly degraded. Therefore, this new form of thermocells has proved its possibility to replace LTCs for leakage-preventing waste heat harvesting.

Another latest research on quasi-solid state thermocell has a record-breaking progress. $Fe(CN)_6^{3-}/Fe(CN)_6^{4-}$ redox species are used in a gelatin matrix prepared with ion donors (KCl, NaCl and KNO_3). This gelatin electrolyte has a thermal diffusion effect, thereby obtaining a S_e of 17.1 mV K^{-1}.[117] This is the highest S_e to date in thermocells based on redox reactions.[76] By using human body heat, a proof-of-concept wearable thermocell device consisting of 25 unipolar elements generated more than 2.2 V and a peak power of 5 uW.[117] This quasi-solid state thermocell with ionic gelatin shows promise for efficient and environmental thermoelectic energy conversion. This work also provides a promising method for realizing cable-free and battery-free energy supply for IoT sensors.

Recently, a variety of quasi-solid electrolyte materials based on conductive polymers have been developed. They also have the advantages of high S_e, high flexibility, and easy manufacturing, thus have proven to be promising.[118],[119] However, the thermodynamic and transport properties of these new quasi-solid electrolyte materials are still ambiguous and require further research before application.

In general, the quasi-solid state thermocell technology has great potential as a specific application direction. In particular, high Se can be obtained. However, the mass transfer process in quasi-solid electrolytes is more difficult than in ionic liquids. In

order to obtain better cell performance, the thermoelectric conversion efficiency must be sacrificed. In other words, the external environment needs to provide more continuous and stable heat sources. Compared with the manufacturing cost of the quasi-solid electrolyte, this is a fatal disadvantage in commercialization. The practical application of this technology still needs a long way to go.

1.2.2.2. Multi-phase thermocell

In the research of thermocells, the main direction of improving Se has been changed to create a greater difference in entropy in the cold and hot sides of the cell. Therefore, some recent studies have used the huge entropy change brought about by the phase change of redox species to improve the performance of thermocells. Because these types of thermocells often require electrolytes with more than two phases, they are called multi-phase thermocells.[76]

The multi-phase thermocells developed by the bromine vapor cycle have been reported successively by Endo et al. since the 1980s. [120]–[122] A S_e of 5.68 mV K^{-1} can be achieved when the hot side of the thermocell is operated at the temperature above the boiling ponit of gas phase Br_2. This result is attributed to the evaporation of Br_2, while the corrosive and toxic vapors limit its practicality. Recently, a thermocell based on the redox species of acetone and iso-propanol has been developed, which can achieve a high S_e of -9.9 mV K^{-1} due to the liquid-gas phase change (Figure 1-14).[123] Relative to the Carnot efficiency, the conversion efficiency is 1.57%, which is

comparable to the conventional $Fe(CN)_6^{3-}/Fe(CN)_6^{4-}$ redox species. In addition, unlike the Br_2/Br^- redox species, acetone and iso-propanol are harmless to the environment.

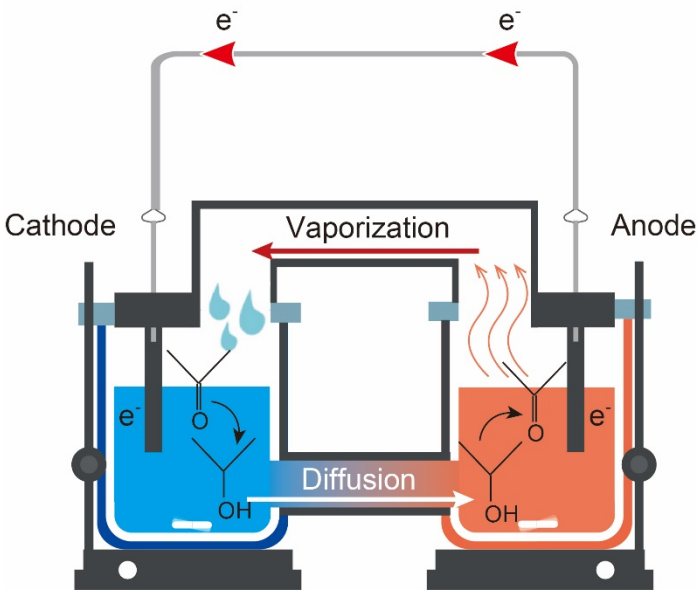

Figure 1-14. Scheme of the acetone and iso-propanol liquid-gas two-phase thermocell. At the hot side, oxidation of iso-propanol to acetone occurs, and the reverse reaction occurs at the cold side of the cell.

The phase transition is most likely to occur at the critical temperature. A study reported that the critical temperature of the electrolyte is close to the working temperature of thermocells by adjusting the composition of the cobalt-Prussian blue analog complex (Co-PBA; $Na_xCo[Fe(CN)_6]_y$). Using this complex redox species can obtain dramatic voltage changes near the critical temperature.[124]

The latest research has improved the LTCs through the thermal crystallization process, so that they present a solid-liquid two-phase state during the working process, thereby increasing the entropy change of the oxidation-reduction reaction. This method achieved a record-breaking thermoelectric conversion efficiency relative to Carnot efficiency of 11.1%, and a high S_e of -3.73 mV K^{-1} using $Fe(CN)_6^{3-}/Fe(CN)_6^{4-}$ redox species with a guanidinium cations.[82] After the addition of guanidinium cations, $Fe(CN)_6^{3-}/Fe(CN)_6^{4-}$ concentration ratio at the cold and hot electrodes changed due to the crystallization of $Fe(CN)_6^{4-}$. Unlike LTC techniques that enhanced S_e while sacrificed effective ion conductivity, this thermosensitive crystallization solid-liquid two-phase thermocell enhances S_e and reduces effective thermal conductivity without sacrificing ion conductivity. This provides a feasible solution for solving the low efficiency problem caused by the balanced relationship between electrical conductivity and thermal conductivity in LTC systems.

Multi-phase thermocells use sophisticated cell module design to introduce the huge entropy change produced by phase change into the thermocell system, thus it can obtain larger S_e or higher thermoelectric conversion efficiency than conventional LTCs. However, in practical applications, in order to ensure that there is enough space for the phase change to proceed, such a multiphase thermocell often requires a larger device design.[73] In contrast, they need higher single cell efficiency than conventional LTCs to ensure that they will not cause higher manufacturing and maintenance costs due to excessive volume in actual applications. In addition, although redox species containing

gaseous form tend to produce higher amounts of S_e, they are more likely to leak than in liquid form, which also limits their broader application.

After summarizing the non-liquid state thermocell, it can be seen that these technologies are still in the laboratory research stage. The performance potential brought by this new form of thermocells is considerable. They have achieved the highest S_e (17.1 mV K^{-1}) and the highest thermoelectric conversion efficiency (11.1% relative to Carnot efficiency) in thermocell-related research to date. However, to achieve this performance improvement needs to sacrifice the advantages of simplicity and scalability of LTCs. The stability and reproducibility of special electrolyte additives or special redox species used in non-liquid state thermocells need to be checked. In the direction of practicality, quasi-solid state thermocells are more suitable for use in wearable devices, while multiphase thermocells are more suitable to achieve ultra-high cell performance near a specific temperature.

1.2.3. Recent developments in thermocell application

At present, the practical application of thermocells is severely limited by the low voltage. Although the maximum potential of a single thermocell will be limited by Se and the temperature gradient, by connecting multiple thermocells in series, the potential difference can increase significantly.[86] This is similar to the concept used in solid state TEG, in which multiple TEG devices are connected in series to maximize electrical power output (Figure 1-6). The *n*-type and *p*-type semiconductor materials can be

equivalent to thermocells with negative and positive S_e, respectively. As mentioned above, the S_e of $Fe(CN)_6^{3-}/Fe(CN)_6^{4-}$ redox species is -1.4 mV K^{-1}, which can be used as an n-type thermocell. It is also reported that the $FeSO_4/Fe_2(SO_4)_3$ redox species in the aqueous solution can be used as a p-type thermocell. Its S_e is 1.7 mV K^{-1}.[94] When n-type and p-type cells are connected in series, when ΔT =10 K, the total voltage increases to 31 mV, which is equivalent to 3.1 mV K^{-1}, while the current remains the same. An array of 50 thermocell pairs are connected in series, and for the same ΔT, the S_e is improved to 150 mV K^{-1}, the maximum voltage is increased to 1.5 V. The voltage range above this value can power a variety of electronic devices through conventional methods, which increases the possibility of practical use.[82]

Overall, the use of thermocells to harvest low- and ultra-low-quality waste heat offers the promise of an low-cost, sustainable and continuous method of energy generation. The global waste heat potential and increasing spotlight on wearable devices also lead a demand of thermocell applications. Utilizing advances in transport theories and electrochemistry, breakthroughs have been made in the development of thermocells with greatly improved power density and conversion efficiency. However, although these advances have achieved important commercial feasibility and possible applications, a lot of research is still needed to understand and overcome key performance limitations. These insights require further development of basic research and cell design. The breakdown of all the thermoelectric conversion technologies and thermocells discussed above is summarized in Figure 1-15.

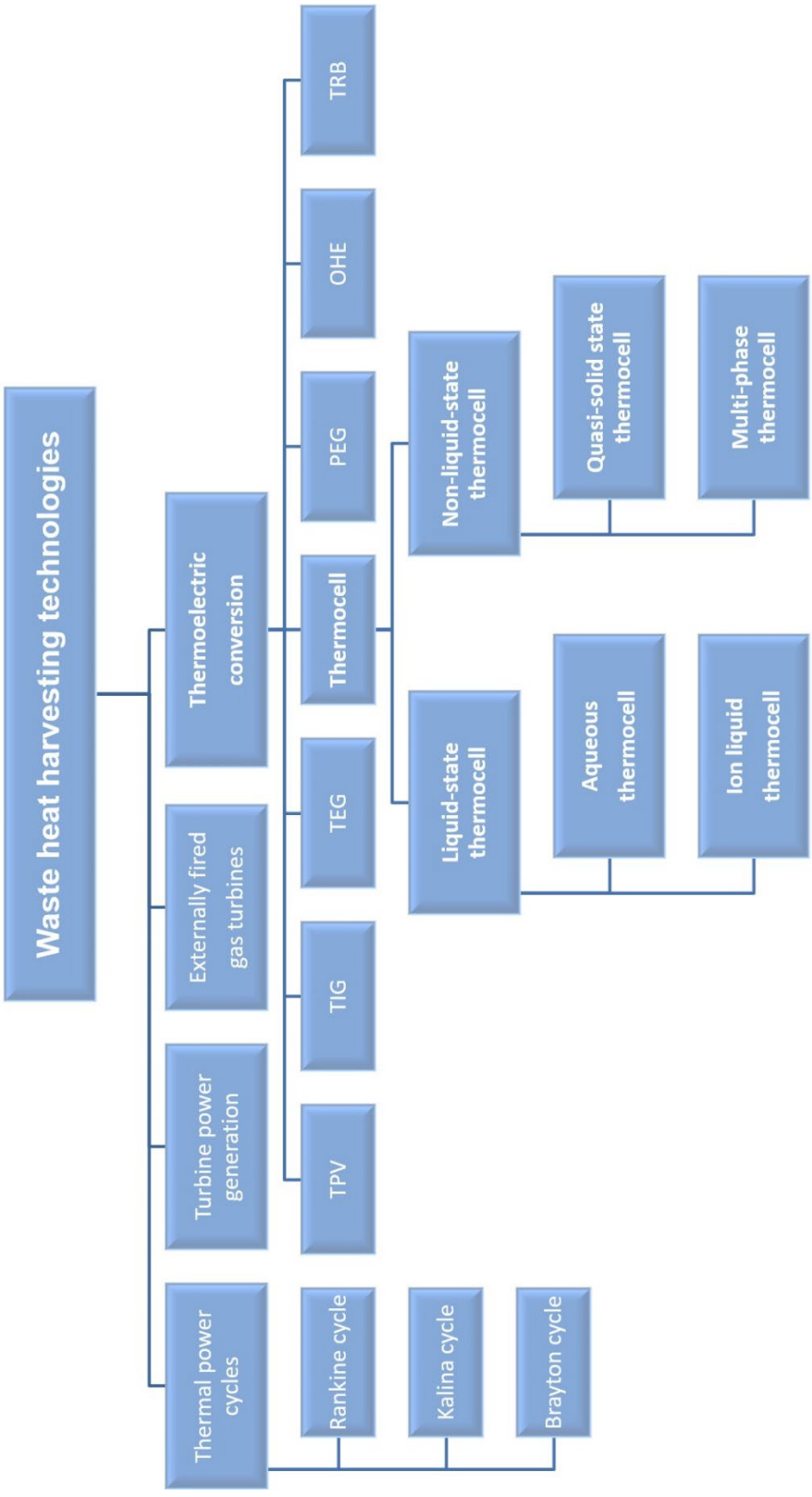

Figure 1-15. Technology options for waste heat harvesting.

In order to improve performance, it is necessary to further understand the basic properties of thermocells, including the use of new redox species and electrolyte additives to maximize entropy change, as well as improving electrode properties and engineering strategies to increase the mass transfer rate. In addition, the requirements of thermocell materials will vary according to the anticipated application. For example, for wearable devices, the use of non-toxic redox species and electrolytes will be important, while higher temperature applications require more thermally stable electrolytes. To date, for the most convenient liquid-state thermocells, the electrical power output of Se and unit temperature difference needs to be improved. It is necessary to develop a new thermocell system in addition to the conventional redox species to enhance the cell performance, thereby expanding the wide application direction with the possibility of commercialization and practicality.

1.3. Thermal responsive hydrogel nanoparticles

Gels are macromolecular three-dimensional polymer networks. Gels have both solid and fluid properties in many respects. On one hand, when removed from their container, gels have structural integrity and do not flow appreciably. On the other hand, the transport of material through a gel is similar to mass transport in a fluid for molecules that are significantly smaller than the pore size of the gel.[125]

In the case of hydrogels, they are swellen with a medium such as water, and are typically composed of hydrophilic organic plymer component that is cross-linked into a network by either physival or hemical interactions. Hydrogels can also be classified based on their size as either macrogels or microgels. Macrogels are bulk gels whose size can range from millimeters or even larger, while microgels, which also called hydrogel nanoparticles, are colloidally stable hydrogels whose size can range from tens of nanometers to micrometers.[125] Swelling is the most important feature of hydrogel nanoparticles, which is achieved through chemical or physical cross-linking between polymers. In other words, the essence of forming hydrogel nanoparticles is to form suitable crosslinks between polymers.[126]

Stimuli-responsive hydrogels nanoparticles are of great interest as materials with dynamic functions[127] because they show a drastic volume change in response to a small external stimuli such as change in temperature[128]–[131], pH[132], photo irradiation[133], electric field[134], and molecular recognition[135],[136]. They are also called

'smart' materials, due to the swelling upon water absorption and responsibility to subtle changes in the environment as mentioned above by swelling changing.[137]

1.3.1. Thermal responsive polymers and gels

Poly(*N*-isopropylacrylamide) (pNIPAM) hydrogels nanoparticles are the most widely studied stimuli-sensitive hydrogel. pNIPAM can be easily synthesized through a variety of methods, such as free radical initiation, photo-initiation, redox initiation, and ionic intiation.[138] The earliest research on pNIPAM began in the 1960s. Heskins et al. reported the phase transfer of pNIPAM driven by thermal entropy changes.[139] That is, the pNIPAM can undergo phase separation from the swollen phase to the shrunk phase at the critical temperature around 32 °C as a result of entropically driven dissociation of water from the polymer chains (Figure 1-16).[140],[141] The dissolution behavior of polymers in solvents is mainly related to three kinds of equilibrium, namely, the intermolecular interaction between solvent-solvent, solvent-polymer, and polymer-polymer. As a stimuli-sensitive polymer, the pNIPAM tends to choose stronger interactions to be more stable in the environment of aqueous solutions. pNIPAM contains hydrophilic and hydrophobic functional groups. Hydrophilic functional groups form hydrogen bonds with water as a solvent-polymer interaction in an aqueous solution, while hydrophobic functional groups tend to undergo polymer-polymer hydrophobic interactions.[137] Under the conditions where the pNIPAM has a random-coil molecular structure, the solvent-polymer interaction (hydrogen bond) is stronger

than polymer-polymer interaction (hydrophobic effect). When the temperature is increasing, the hydrogen bonds between hydrophilic groups and water molecules are broken. The globular polymer conformation occurs due to the entropically favored release of the structured water molecules. As a result, the hydrophobic polymer-polymer interaction become stronger than the solvent-polymer interaction, and the phase separation of the pNIPAM polymer occurs. The critical temperature at which the phase separation occurs is called lower critical solution temperature (LCST).

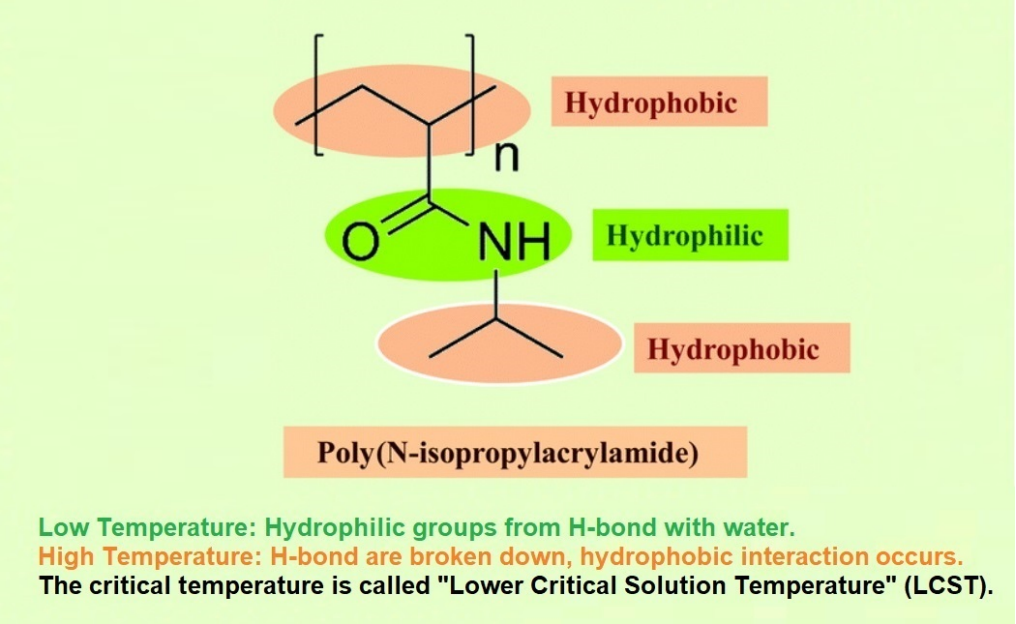

Figure 1-16. Illustration of structure of pNIPAM.

It can be known from the phase transfer mechanism of pNIPAM that the critical temperature of the intermolecular interaction that occurs with temperature is affected

by the relative strength of the hydrophilic and hydrophobic functional groups in the polymer. As the hydrophobicity of the hydrophobic functional groups in the polymer increases, it is easier to form a stable polymer-polymer interaction at a lower temperature, resulting in a decrease in LCST. On the contrary, if hydrophilic functional groups are dominant, more energy is needed to break the hydrogen bonds in water, which will cause the polymer to undergo phase transfer at higher temperatures. This improves the LCST as a result.

Contrary to the behavior of LCST, some thermal responsive polymers will show an upper critical solution temperature (UCST). In this case, the phase separation of the polymer occurs in a relatively low temperature environment due to intermolecular interactions such as hydrogen bonds or electrostatic interactions. While, at high temperatures, this interaction is broken and the polymer dissolves and swells.[125]

The LCST behavior in an aqueous solution is attractive, and therefore, thermal responsive polymers such as pNIPAM are widely used in the synthesis of responsive polymers. Hydrogel nanoparticles comprising of the thermal responsive polymers is called thermal responsive hydrogel nanoparticles. pNIPAM. Since pNIPAM also changes in volume during the phase separation process, this effect is called volume phase transfer (VPT). Its LCST temperature is called the volume phase transition temperature (VPTT). Basically, the VPTT of the hydrogel nanoparticles is the same as the LCST of the constituent polymer.

Controlling the LCST of thermal responsive hydrogel nanoparticles can enable it to achieve phase transition at a specific temperature which meet the application requirement, thereby greatly expanding its application direction. As a typical thermal responsive polymer exhibiting VPT, pNIPAM hydrogels nanoparticles with stimuli responsive molecular recognition properties and a LCST near 32 °C have been developed to reversibly capture and release target molecules such as dyes[142], drugs[143] and proteins[144]. More recently, the gels have been applied as an economical media to extract and/or concentrate moisture[139],[145], salts[146] and carbon dioxide[147] using low temperature waste heat and solar energy as an energy source.

1.3.2. pH responsibility of the thermal responsive hydrogel nanoparticles

Researchers have develop proton concentration (pH) responsive polymers and hydrogel nanopariticles by copolymerizing ionic monomers with pNIPAM.[148]–[151]

The swelling of pH responsive hydrogel nanoparticles is the result of the interdependence between the pH and the ionic strength of the solution in contact with the gel. Inside the hydrogel nanoparticle, ionizable monomers will dissociate according to the pH. The free counter ions generated in the hydrogel nanoparticles are exchanged with the salt ions in the solution, thereby generating a certain osmotic pressure difference between the gel and the solution. Therefore, the hydrogel nanoparticles will swell until the elastic and osmotic force inside the gel reach equilibrium.[152] According

to this mechanism, changing the ionization strength of the functional groups in the hydrogel nanoparticle polymer can effectively adjust the pH.

Our group reported the use of proton imprinting methods to synthesize thermal responsive hydrogel nanoparticles whose acid dissociation constants (pK_a) can reversibly shift before and after VPT (Figure 1-17).[153] The pK_a shift can lead a responsive pH change of the hydrogel solution. By controlling the solution pH during the synthesis of thermal responsive hydrogel nanoparticles with a monomer consisting of carboxylic acid, protons are imprinted into the stable structure of the hydrogel nanoparticles after synthesis. The nanoparticles obtained by this method can form a hydrophobic polymer matrix that specifically binds to protons after VPT occurs, thereby achieving a large reversible pK_a shift of 2.2.

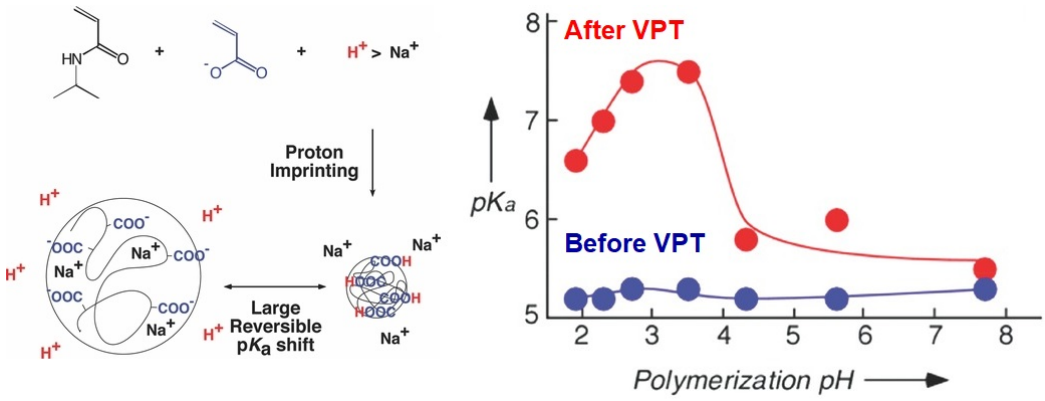

Figure 1-17. Reversible pK_a shift of thermal responsive hydrogel nanoparticles consisting of carboxylic acids triggered by VPT. Reproduced with permission from ref[153].

Furthermore, to obtain thermal responsive hydrogel nanoparticles displaying a reversible pK_a shift over a wider range of pK_a values, a procedure to prepare proton imprinted nanoparticles that show temperature dependent pK_a shifts in the tuned pK_a range is required. The detailed method is reported as introducing an acrylic acid whose α-position was substituted by a strong electron-withdrawing or electron-donating group such as chloride or methyl, respectively, into the pNIPAM thermal responsive hydrogel nanoparticles (Figure 1-18).[154]

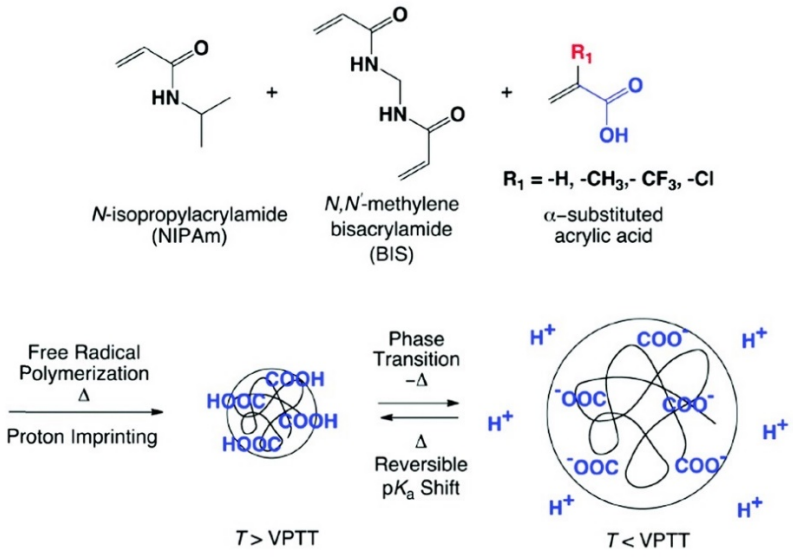

Figure 1-18. Synthesize of proton-imprinted thermal responsive hydrogel nanoparticles using a variety of acrylic monomers. The wide range pK_a shift of carboxylic acids in nanoparticles is triggered by VPT. Reproduced with permission from ref[154].

As reported[153], the high pK_a value of acrylic acid nanoparticles polymerized at low pH is attributed to the proton imprinting effect. Because acrylic acid monomers are protonated in the presence of high concentrations of protons at low pH, the protonated acrylic acid is easily incorporated in the less polar domain of the growing pNIPAm, through hydrogen bonding with other carboxylic acids on the polymers. Due to this mechanism, by the selection of carboxylic acid-containing monomers, the pK_a values of α-substituted acids in the collapsed nanoparticles can be tuned (Figure 1-19).[154]

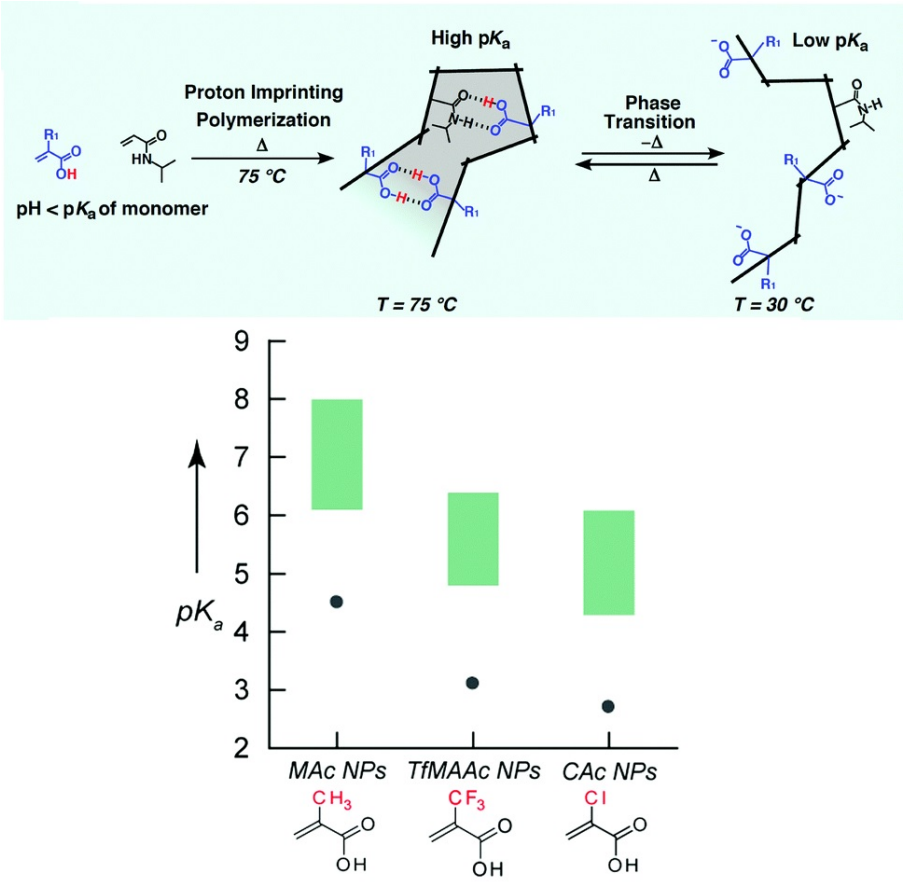

Figure 1-19. Mechanism of thermal responsive pK_a shift of proton-imprinted nanoparticles triggered by the VPT. pK_a values of α-substituted acrylic acid at 75°C and 30°C are shown in green bars. The pK_a values of monomers are shown in black. Reproduced with permission from ref[154].

In addition, the method of simultaneously introducing two monomers with different charges, such as ionized Brønsted acid and Brønsted base, has also been studied.[155] This method can expand the pK_a shift range of thermal responsive hydrogel nanoparticles. The maximum achieved pK_a shift range was approximately 3.3 log units (from 4.0 to 7.3) at 75 °C.

Hydrogel nanoparticles with this property can change the pH of the solution by more than 1000 times before and after VPT and have a wide range of application prospects. For example, the use of thermal energy for reversible ion/proton exchange, so as to realize the reversible collection of acid gases (such as carbon dioxide)[147],[156], or use in seawater desalination[146] and other fields.

1.3.3. Swelling kinetics of the thermal responsive hydrogel nanoparticles

The swelling process parameters of thermal responsive hydrogel nanoparticles, including relaxation time, radius change and their molecular dynamics, will all affect their material properties in practical application on a macroscopic scale.

The relaxation time of the swelling process of a thermal responsive hydrogel nanoparticle is determined experimentally from the single-exponential region of the time dependent volume change in a temperature jump experiment. The relationship of final equilibrium radius (R) and total radius (ΔR_0) change of a gel can be described as[157],[158]:

$$\Delta R(t) \sim \left(\frac{6\Delta R_0}{\pi^2}\right) exp\left(\frac{-t}{\tau}\right) \qquad \text{Eq. 1-10}$$

where τ is the relaxation time. The radius of a thermal responsive hydrogel nanoparticle changes rapidly for times smaller than τ. The τ is defined as the decay time appearing in the single-exponential region:

$$\tau = \frac{R^2}{\pi^2 D} \qquad \text{Eq. 1-11}$$

where D is the ratio of the osmotic bulk modulus and the friction coefficient between the hydrogel network and water and is also called the collective diffusion coefficient. It shows that the τ is proportional to the square of the hydrogel radius and inversely proportional to the D of the hydrogel and is attributed to the inner structure of the polymer network.[157],[158]

Our group reported novel thermal responsive nanoparticles in a hydrogel film for temperature-responsive quick and reversible capture of salt in seawater.[146] This study pointed out that the film made of hydrogel nanoparticles will also undergo VPT with temperature changes in aqueous solution. The macroscopic result is a rapid and reversible change in membrane area (Figure 1-20a and Figure 1-20b). The

shrinking/swelling process can be adapted to a single exponential decay (Eq. 1-10) and exhibits rapid phase transition kinetics (Figure 1-20c). This is due to the fast VPT behavior of NPs in the film. The relaxation time of the hydrogel nanoparticles dispersed in the solution is 6 orders of magnitude faster than that observed in the membrane structure. And the relaxation time can be changed effectively through the structural design of the polymer.[146] This result proves that the VPT of hydrogel nanoparticles is fast and sensitive, and therefore, can be used to harvest small and rapid thermal energy changes.

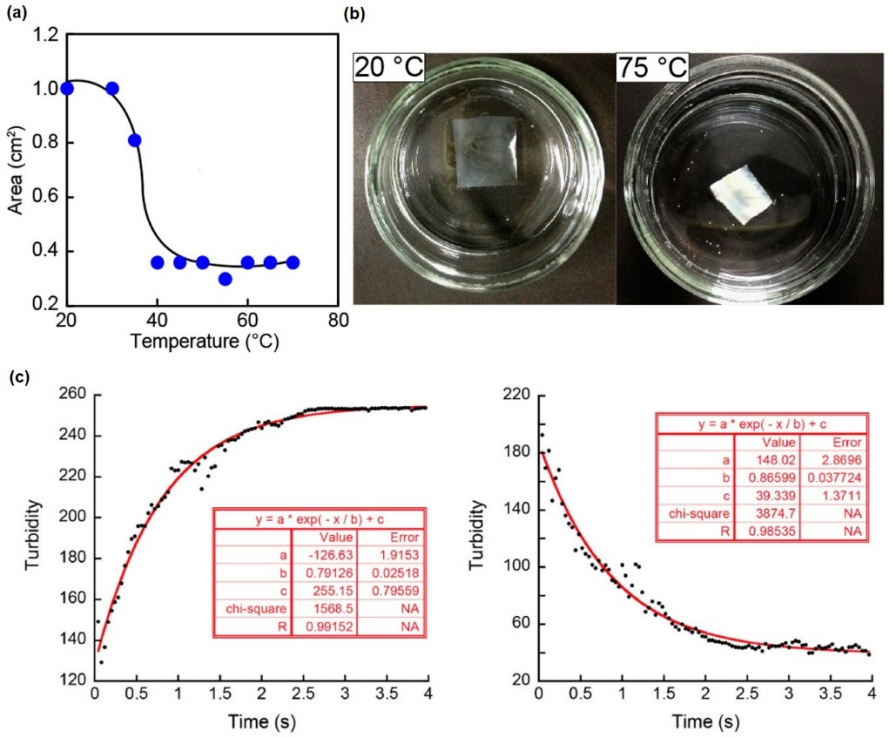

Figure 1-20. (a) Area of thermal responsive nanoparticles film as a function of water temperature. (b) Thermal responsive nanoparticles film in water at 20 and 75 °C. (c) Time-dependence of the turbidity change of mixed nanoparticles film in heating and

cooling process. The relaxation time τ of 790 and 870 ms, respectively, is measured. Reproduced with permission from ref[159].

In general, thermal responsive hydrogel nanoparticles have been widely studied in many fields and have attracted a lot of attention. Especially in drug delivery[160],[161], medical devices[162],[163], and functional materials[164],[165]. Adjusting pH sensitivity and LCST, coupled with engineering strategies to change its swelling kinetics, further broaden the application of thermal responsive hydrogel nanoparticles.[146],[154],[155] However, few studies have introduced these excellent characteristic of thermal responsive hydrogel nanoparticles into a more macroscopic research field, such as the energy field.

1.4. About this study

Since the industrial revolution, the massive use of a large number of chemical fuels and the rapid growth of industrial production activities have led to severe environmental problems and energy crises. At the same time, a huge amount of waste heat is generated in global energy consumption and industrial production, and this thermal energy has a high potential for energy recovery. Energy harvesting from ultra-low-quality waste heat (temperature < 120 °C) with the largest proportion, delocalized but abundant, such as automobile exhaust heat, human body heat and solar heat is crucial to realize sustainable development goals (SDGs) and carbon-free human society. However, improving the conversion efficiency of converting waste heat energy resources into electricity, the most convenient high-grade energy, remains a significant challenge. The development of highly efficient thermoelectric conversion devices that is simple and mass-producible is key for the use of thermal energy. Although among many thermoelectric conversion technologies, there have been some commercial examples of using thermoelectric generator to harvest high-quality waste heat. Improvement of output power density and S_e in a temperature range of ultra-low-quality waste heat without using toxic and/or minor metals is required for the practical use of these technologies.

In this thesis, the author describes a novel liquid-state thermocell based on the aqueous electrolyte with thermal responsive hydrogel nanoparticles. This thermocell utilizes the volume phase transfer process of the nanoparticles near the ambient

temperature, which can generate very high voltage and output power under a condition of low temperature and small temperature range, thereby achieving efficient harvesting of ultra-low temperature waste heat. Compared with the research in other thermocell fields, this thesis uses simple and safe aqueous electrolyte to achieve thermoelectric conversion efficiency and record-breaking output power beyond other more complex and expensive thermocells by introducing stimuli-responsive polymer materials. This thesis also proposes the design rationale for this novel thermoelectric conversion system by screening and optimizing the components of the thermocell. Moreover, the improvement of the practical design of the cell device in this thesis shows that this thermocell has the possibility of commercialization and practicality. The author believes that the simple, inexpensive, and non-toxic thermoelectric conversion technology in this thesis for ultra-low quality waste heat harvesting will give a fundamental insight into design of energy conversional devices using stimuli-responsive smart materials and provide a direction for the development of flexible energy chargers for wireless devices including portable smart devices and sensors.

In chapter 2, a new thermoelectric conversion mechanism based on the proton-responsive redox reaction and the pH response of hydrogel nanoparticles is proposed. Using a simple and basic liquid-state thermocell system, a typical electrolyte combination, quinhydrone and acrylic acid-containing thermal responsive hydrogel nanoparticles are used as an example to illustrate this mechanism.

In chapter 3, the design rationale of thermocell using thermal sensitive hydrogel nanoparticles is discussed. By screening the types and concentrations of redox species, electrolyte salts and hydrogel nanoparticles, and optimizing the composition of these three basic thermocell components, the record-breaking Seebeck coefficient and extremely high energy conversion efficiency have been achieved.

In chapter 4, by actually assembling the thermocell device, engineering strategies for optimizing cell performance are discussed. A planar liquid-state thermocell with low inter-electrode spacing using CNT buckypaper electrodes and laser-processed PTFE porous separators is designed to improve the cell output power density for waste heat harvesting. The design and introduction of the separator, the precise control of the temperature difference, and the use of carbon nanotube material electrodes with high effective surface area have highly improved the practical performance of the thermocell. The expression of the coupling relationship between cell performance parameters such as the effect of natural converction and inter-electode spacing in actual cell operation is also mentioned. This clarifies that liquid-state thermocells using thermal sensitive hydrogel nanoparticles can flexibly change their design according to different application situations to ensure high output power performance.

1.5. Reference

[1] Hoffert, M. I.; Caldeira, K.; Benford, G.; Criswell, D. R.; Green, C.; Herzog, H.; Jain, A. K.; Kheshgi, H. S.; Lackner, K. S.; Lewis, J. S.; others. *Science.* **2002**, *298*, 981–987.

[2] Forman, C.; Muritala, I. K.; Pardemann, R.; Meyer, B. *Renewable and Sustainable Energy Reviews*. Elsevier Ltd May 1**, 2016**, pp 1568–1579.

[3] Chu, S.; Majumdar, A. *Nature* **2012**, *488*, 294–303.

[4] Rowe, D. M. *Renewable Energy*. **1999**, pp 1251–1256.

[5] Cullen, J. M.; Allwood, J. M. *Energy* **2010**, *35*, 2059–2069.

[6] Lion, S.; Michos, C. N.; Vlaskos, I.; Rouaud, C.; Taccani, R. *Renew. Sustain. Energy Rev.* **2017**, *79*, 691–708.

[7] Lawrence Livermore National Laboratory. *Japan Estimated Energy Use Flow Chart*; **2020**.

[8] Lawrence Livermore National Laboratory. *U.S. Estimated Energy Use Flow Chart*; **2020**.

[9] Semkov, K.; Mooney, E.; Connolly, M.; Adley, C. *Appl. Therm. Eng.* **2014**, *70*, 716–722.

[10] Rashid, W. E. S. W. A.; Ker, P. J.; Jamaludin, M. Z. Bin; Gamel, M. M. A.; Lee, H. J.; Rahman, N. B. A. *IEEE Access* **2020**, *8*, 105156–105168.

[11] Garofalo, E.; Bevione, M.; Cecchini, L.; Mattiussi, F.; Chiolerio, A. *Energy Technol.* **2020**, *8*, 2000413.

[12] Su, Z.; Zhang, M.; Xu, P.; Zhao, Z.; Wang, Z.; Huang, H.; Ouyang, T. *Energy*

Convers. Manag. **2021**, *229*, 113769.

[13] Soda, M.; Beyene, A. *Int. J. Energy Res.* **2016**, *40*, 51–60.

[14] Allahverdyan, A. E.; Hovhannisyan, K. V; Melkikh, A. V; Gevorkian, S. G. *Phys. Rev. Lett.* **2013**, *111*, 50601.

[15] Leonov, V.; Vullers, R. J. M. *J. Renew. Sustain. Energy* **2009**, *1*, 62701.

[16] Bhatnagar, V.; Owende, P. *Energy Sci. & Eng.* **2015**, *3*, 153–173.

[17] Lecompte, S.; Huisseune, H.; Van Den Broek, M.; Vanslambrouck, B.; De Paepe, M. *Renew. Sustain. energy Rev.* **2015**, *47*, 448–461.

[18] Mamia, I.; Appelbaum, J. *Renew. Sustain. Energy Rev.* **2016**, *55*, 713–718.

[19] Abd El-Sattar, H.; Kamel, S.; Vera, D.; Jurado, F. *J. Clean. Prod.* **2020**, *260*, 121068.

[20] Soundararajan, K.; Ho, H. K.; Su, B. *Appl. Energy* **2014**, *136*, 1035–1042.

[21] Nelson, R. E. *Semicond. Sci. Technol.* **2003**, *18*, S141.

[22] Coutts, T. J. *Sol. energy Mater. Sol. cells* **2001**, *66*, 443–452.

[23] Massicotte, M.; Schmidt, P.; Vialla, F.; Watanabe, K.; Taniguchi, T.; Tielrooij, K.-J.; Koppens, F. H. L. *Nat. Commun.* **2016**, *7*, 1–7.

[24] Han, Y.; Zhang, H.; Hu, Z.; Hou, S. *Energy* **2021**, *223*, 120095.

[25] Bell, L. E. *Science* . **2008**, *321*, 1457–1461.

[26] Siddique, A. R. M.; Mahmud, S.; Van Heyst, B. *Renew. Sustain. Energy Rev.* **2017**, *73*, 730–744.

[27] Sebald, G.; Guyomar, D.; Agbossou, A. *Smart Mater. Struct.* **2009**, *18*, 125006.

[28] Thakre, A.; Kumar, A.; Song, H.-C.; Jeong, D.-Y.; Ryu, J. *Sensors* **2019**, *19*, 2170.

[29] McGinnis, R. L.; McCutcheon, J. R.; Elimelech, M. *J. Memb. Sci.* **2007**, *305*, 13–19.

[30] McGinnis, R. L.; Elimelech, M. ACS Publications **2008**.

[31] Boo, C.; Khalil, Y. F.; Elimelech, M. *J. Memb. Sci.* **2015**, *473*, 302–309.

[32] Yip, N. Y.; Vermaas, D. A.; Nijmeijer, K.; Elimelech, M. *Environ. Sci. & Technol.* **2014**, *48*, 4925–4936.

[33] Yang, Y.; Lee, S. W.; Ghasemi, H.; Loomis, J.; Li, X.; Kraemer, D.; Zheng, G.; Cui, Y.; Chen, G. *Proc. Natl. Acad. Sci.* **2014**, *111*, 17011–17016.

[34] Facchinetti, I.; Ruffo, R.; La Mantia, F.; Brogioli, D. *Cell Reports Phys. Sci.* **2020**, *1*, 100056.

[35] Maye, S.; Girault, H. H.; Peljo, P. *Energy & Environ. Sci.* **2020**, *13*, 2191–2199.

[36] Dupont, M. F.; MacFarlane, D. R.; Pringle, J. M. *Chem. Commun.* **2017**, *53*, 6288–6302.

[37] Lee, S. W.; Yang, Y.; Lee, H.-W.; Ghasemi, H.; Kraemer, D.; Chen, G.; Cui, Y. *Nat. Commun.* **2014**, *5*, 1–6.

[38] Datas, A.; Algora, C. *Prog. Photovoltaics Res. Appl.* **2013**, *21*, 1025–1039.

[39] Humphrey, T. E.; O'Dwyer, M. F.; Linke, H. *J. Phys. D. Appl. Phys.* **2005**, *38*, 2051.

[40] Ovik, R.; Long, B. D.; Barma, M. C.; Riaz, M.; Sabri, M. F. M.; Said, S. M.;

Saidur, R.; others. *Renew. Sustain. energy Rev.* **2016**, *64*, 635–659.

[41] He, J.; Tritt, T. M. *Science*. American Association for the Advancement of Science September 29**, 2017**, p 1369.

[42] Quickenden, T. I.; Mua, Y. *J. Electrochem. Soc.* **1995**, *142*, 3985–3994.

[43] Nolas, G. S.; Sharp, J.; Goldsmid, J. *Thermoelectrics: Basic Principles and New Materials Developments*; Springer Science & Business Media, **2013**; Vol. 45.

[44] Tritt, T. M.; Subramanian, M. A. *MRS Bull.* **2006**, *31*, 188–198.

[45] Snyder, G. J.; Toberer, E. S. *Mater. Sustain. energy a Collect. peer-reviewed Res. Rev. Artic. from Nat. Publ. Gr.* **2011**, 101–110.

[46] Twaha, S.; Zhu, J.; Yan, Y.; Li, B. *Renew. Sustain. energy Rev.* **2016**, *65*, 698–726.

[47] Kanatzidis, M. G.; Mahanti, S. D.; Hogan, T. P. *Chemistry, Physics, and Materials Science of Thermoelectric Materials: Beyond Bismuth Telluride*; Springer Science & Business Media, **2003**.

[48] Zeb, K.; Ali, S. M.; Khan, B.; Mehmood, C. A.; Tareen, N.; Din, W.; Farid, U.; Haider, A. *Renew. Sustain. Energy Rev.* **2017**, *75*, 1142–1155.

[49] Mahalakshmi, P.; Kalaiselvi, S. *Int. J. Adv. Res. Electr. Electron. Instrum. Eng.* **2014**, *3*.

[50] Tan, J.; Kalantar-Zadeh, K.; Wlodarski, W.; Bhargava, S.; Akolekar, D.; Holland, A.; Rosengarten, G. In *Smart Sensors, Actuators, and MEMS II*; **2005**; Vol. 5836, pp 711–718.

[51] Zheng, Z.; Fan, P.; Luo, J.; Liang, G.; Zhang, D. *J. Electron. Mater.* **2013**, *42*, 3421–3425.

[52] Hsu, C.-T.; Huang, G.-Y.; Chu, H.-S.; Yu, B.; Yao, D.-J. *Appl. Energy* **2011**, *88*, 1291–1297.

[53] Sano, S.; Mizukami, H.; Kaibe, H. *Komatsu Tech. Rep* **2003**, *49*, 1–7.

[54] DiSalvo, F. J. *Science* . **1999**, *285*, 703–706.

[55] Ioffe, A. F.; Stil'Bans, L. S.; Iordanishvili, E. K.; Stavitskaya, T. S.; Gelbtuch, A.; Vineyard, G. *Phys. Today* **1959**, *12*, 42.

[56] Zhao, L.-D.; Dravid, V. P.; Kanatzidis, M. G. *Energy & Environ. Sci.* **2014**, *7*, 251–268.

[57] Bejan, A.; Kraus, A. D. *Heat Transfer Handbook*; John Wiley & Sons, **2003**; Vol. 1.

[58] Zhao, L.-D.; Lo, S.-H.; Zhang, Y.; Sun, H.; Tan, G.; Uher, C.; Wolverton, C.; Dravid, V. P.; Kanatzidis, M. G. *Nature* **2014**, *508*, 373.

[59] Takashiri, M.; Shirakawa, T.; Miyazaki, K.; Tsukamoto, H. *Sensors Actuators A Phys.* **2007**, *138*, 329–334.

[60] Yadav, A.; Pipe, K. P.; Shtein, M. *J. Power Sources* **2008**, *175*, 909–913.

[61] Navone, C.; Soulier, M.; Plissonnier, M.; Seiler, A. L. *J. Electron. Mater.* **2010**, *39*, 1755–1759.

[62] Francioso, L.; De Pascali, C.; Farella, I.; Martucci, C.; Creti, P.; Siciliano, P.; Perrone, A. *J. Power Sources* **2011**, *196*, 3239–3243.

[63] Jo, S. E.; Kim, M. K.; Kim, M. S.; Kim, Y. J. *Electron. Lett.* **2012**, *48*, 1015–

1017.

[64] Khan, S.; Dahiya, R. S.; Lorenzelli, L. In *2014 44th European Solid State Device Research Conference (ESSDERC)*; **2014**; pp 86–89.

[65] Fan, P.; Zheng, Z.; Li, Y.; Lin, Q.; Luo, J.; Liang, G.; Cai, X.; Zhang, D.; Ye, F. *Appl. Phys. Lett.* **2015**, *106*, 73901.

[66] Martin-González, M.; Caballero-Calero, O.; Diaz-Chao, P. *Renew. Sustain. Energy Rev.* **2013**, *24*, 288–305.

[67] Shakouri, A. *Annu. Rev. Mater. Res.* **2011**, *41*, 399–431.

[68] Vining, C. B. *Nat. Mater.* **2009**, *8*, 83–85.

[69] Shakouri, A.; Zebarjadi, M. *Therm. Nanosyst. Nanomater.* **2009**, 225–299.

[70] LeBlanc, S.; Yee, S. K.; Scullin, M. L.; Dames, C.; Goodson, K. E. *Renew. Sustain. Energy Rev.* **2014**, *32*, 313–327.

[71] Rowe, D. M. *CRC Handbook of Thermoelectrics*; CRC press, **2018**.

[72] Suemori, K.; Hoshino, S.; Kamata, T. *Appl. Phys. Lett.* **2013**, *103*, 153902.

[73] Li, M.; Hong, M.; Dargusch, M.; Zou, J.; Chen, Z. G. *Trends in Chemistry*. Cell Press **2020**.

[74] Zito, R. *AIAA J.* **1963**, *1*, 2133–2138.

[75] Liu, W.; Hu, J.; Zhang, S.; Deng, M.; Han, C.-G.; Liu, Y. *Mater. Today Phys.* **2017**, *1*, 50–60.

[76] Duan, J.; Yu, B.; Huang, L.; Hu, B.; Xu, M.; Feng, G.; Zhou, J. *Joule* **2021**.

[77] Gunawan, A.; Lin, C.-H.; Buttry, D. A.; Mujica, V.; Taylor, R. A.; Prasher, R. S.; Phelan, P. E. *Nanoscale Microscale Thermophys. Eng.* **2013**, *17*, 304–323.

[78] Agar, J. N.; Breck, W. G. *Trans. Faraday Soc.* **1957**, *53*, 167–178.

[79] Hu, R.; Cola, B. A.; Haram, N.; Barisci, J. N.; Lee, S.; Stoughton, S.; Wallace, G.; Too, C.; Thomas, M.; Gestos, A.; Dela Cruz, M. E.; Ferraris, J. P.; Zakhidov, A. A.; Baughman, R. H. *Nano Lett.* **2010**, *10*, 838–846.

[80] Buckingham, M. A.; Aldous, L. *J. Electroanal. Chem.* **2020**, *872*, 114280.

[81] Hudak, N. S.; Amatucci, G. G. *J. Electrochem. Soc.* **2011**, *158*, A572.

[82] Yu, B.; Duan, J.; Cong, H.; Xie, W.; Liu, R.; Zhuang, X.; Wang, H.; Qi, B.; Xu, M.; Wang, Z. L.; Zhou, J. *Science* . **2020**, *370*, 342–346.

[83] Fang, Z. *Thermodyn. Chem. aqueous Syst. Rijeka InTech* **2011**, 27–48.

[84] Laux, E.; Uhl, S.; Journot, T.; Brossard, J.; Jeandupeux, L.; Keppner, H. *J. Electron. Mater.* **2016**, *45*, 3383–3389.

[85] Zhou, H.; Yamada, T.; Kimizuka, N. *J. Am. Chem. Soc.* **2016**, *138*, 10502–10507.

[86] Duan, J.; Feng, G.; Yu, B.; Li, J.; Chen, M.; Yang, P.; Feng, J.; Liu, K.; Zhou, J. *Nat. Commun.* **2018**, *9*, 1–8.

[87] Quickenden, T. I.; Mua, Y. *J. Electrochem. Soc.* **1995**, *142*, 3985–3994.

[88] SABRI, M. *Sains Malaysiana* **2018**, *47*, 403–408.

[89] Liang, Y.; Yamada, T.; Zhou, H.; Kimizuka, N. *Chem. Sci.* **2019**, *10*, 773–780.

[90] Kim, J. H.; Lee, J. H.; Palem, R. R.; Suh, M. S.; Lee, H. H.; Kang, T. J. *Sci. Rep.* **2019**, *9*, 8706.

[91] Lewis, E. A.; Hansen, L. D. *J. Chem. Soc. Perkin Trans. 2* **1973**, *2*, 2081–2085.

[92] Al-Masri, D.; Dupont, M.; Yunis, R.; MacFarlane, D. R.; Pringle, J. M.

Electrochim. Acta **2018**, *269*, 714–723.

[93] Kobayashi, T.; Yamada, T.; Tadokoro, M.; Kimizuka, N. *Chem. – A Eur. J.* **2021**, *27*, 4287–4290.

[94] Zhang, L.; Kim, T.; Li, N.; Kang, T. J.; Chen, J.; Pringle, J. M.; Zhang, M.; Kazim, A. H.; Fang, S.; Haines, C.; Al-Masri, D.; Cola, B. A.; Razal, J. M.; Di, J.; Beirne, S.; MacFarlane, D. R.; Gonzalez-Martin, A.; Mathew, S.; Kim, Y. H.; Wallace, G.; Baughman, R. H. *Adv. Mater.* **2017**, *29*, 1605652.

[95] Kang, T. J.; Fang, S.; Kozlov, M. E.; Haines, C. S.; Li, N.; Kim, Y. H.; Chen, Y.; Baughman, R. H. *Adv. Funct. Mater.* **2012**, *22*, 477–489.

[96] Im, H.; Kim, T.; Song, H.; Choi, J.; Park, J. S.; Ovalle-Robles, R.; Yang, H. D.; Kihm, K. D.; Baughman, R. H.; Lee, H. H.; Kang, T. J.; Kim, Y. H. *Nat. Commun.* **2016**, *7*, 10600.

[97] Salazar, P. F.; Kumar, S.; Cola, B. A. *J. Electrochem. Soc.* **2012**, *159*, B483.

[98] Ikeshoji, T.; de Nahui, F. N. B.; Kimura, S.; Yoneya, M. *J. Electroanal. Chem. interfacial Electrochem.* **1991**, *312*, 43–56.

[99] Im, H.; Moon, H. G.; Lee, J. S.; Chung, I. Y.; Kang, T. J.; Kim, Y. H. *Nano Res.* **2014**, *7*, 443–452.

[100] Salazar, P. F.; Kumar, S.; Cola, B. A. *J. Appl. Electrochem.* **2014**, *44*, 325–336.

[101] Hasan, S. W.; Said, S. M.; Sabri, M. F. M.; Bakar, A. S. A.; Hashim, N. A.; Hasnan, M. M. I. M.; Pringle, J. M.; MacFarlane, D. R. *Sci. Rep.* **2016**, *6*.

[102] Cabral, D.; Howlett, P. C.; Pringle, J. M.; Zhang, X.; MacFarlane, D. *Electrochim. Acta* **2015**, *180*, 419–426.

[103] Cabral, D. M.; Howlett, P. C.; MacFarlane, D. R. *Electrochim. Acta* **2016**, *220*, 347–353.

[104] Dietzel, M.; Hardt, S. *Phys. Rev. Lett.* **2016**, *116*, 225901.

[105] Yamato, Y.; Katayama, Y.; Miura, T. *J. Electrochem. Soc.* **2013**, *160*, H309.

[106] Migita, T.; Tachikawa, N.; Katayama, Y.; Miura, T. *Electrochemistry* **2009**, *77*, 639–641.

[107] Cornwell, K. *J. Phys. D. Appl. Phys.* **1972**, *5*, 1199.

[108] MacFarlane, D. R.; Tachikawa, N.; Forsyth, M.; Pringle, J. M.; Howlett, P. C.; Elliott, G. D.; Davis, J. H.; Watanabe, M.; Simon, P.; Angell, C. A. *Energy & Environ. Sci.* **2014**, *7*, 232–250.

[109] Sosnowska, A.; Barycki, M.; Gajewicz, A.; Bobrowski, M.; Freza, S.; Skurski, P.; Uhl, S.; Laux, E.; Journot, T.; Jeandupeux, L.; others. *ChemPhysChem* **2016**, *17*, 1591–1600.

[110] Abraham, T. J.; Tachikawa, N.; MacFarlane, D. R.; Pringle, J. M. *Phys. Chem. Chem. Phys.* **2014**, *16*, 2527–2532.

[111] He, J.; Al-Masri, D.; MacFarlane, D. R.; Pringle, J. M. *Faraday Discuss.* **2016**, *190*, 205–218.

[112] Salazar, P. F.; Stephens, S. T.; Kazim, A. H.; Pringle, J. M.; Cola, B. A. *J. Mater. Chem. a* **2014**, *2*, 20676–20682.

[113] Lazar, M. A.; Al-Masri, D.; MacFarlane, D. R.; Pringle, J. M. *Phys. Chem. Chem. Phys.* **2016**, *18*, 1404–1410.

[114] Yang, P.; Liu, K.; Chen, Q.; Mo, X.; Zhou, Y.; Li, S.; Feng, G.; Zhou, J.

Angew. Chemie Int. Ed. **2016**, *55*, 12050–12053.

[115] Wu, J.; Black, J. J.; Aldous, L. *Electrochim. Acta* **2017**, *225*, 482–492.

[116] Jin, L.; Greene, G. W.; MacFarlane, D. R.; Pringle, J. M. *ACS Energy Lett.* **2016**, *1*, 654–658.

[117] Han, C. G.; Qian, X.; Li, Q.; Deng, B.; Zhu, Y.; Han, Z.; Zhang, W.; Wang, W.; Feng, S. P.; Chen, G.; Liu, W. *Science* . **2020**, *368*, 1091–1098.

[118] Kim, S. L.; Hsu, J.-H.; Yu, C. *Org. Electron.* **2018**, *54*, 231–236.

[119] Cole, T. *Science* . **1983**, *221*, 915–920.

[120] Endo, M.; Yamagishi, Y.; Inagaki, M. *Synth. Met.* **1983**, *7*, 203–209.

[121] Shindo, K.; Arakawa, M.; Hirai, T. *J. Power Sources* **1998**, *70*, 228–234.

[122] Shindo, K.; Arakawa, M.; Hirai, T. *J. Power Sources* **2002**, *110*, 46–51.

[123] Zhou, H.; Liu, P. *ACS Appl. Energy Mater.* **2018**, *1*, 1424–1428.

[124] Shibata, T.; Iwaizumi, H.; Fukuzumi, Y.; Moritomo, Y. *Sci. Rep.* **2020**, *10*, 1–8.

[125] Nayak, S.; Lyon, L. A. *Angew. Chemie Int. Ed.* **2005**, *44*, 7686–7708.

[126] Preman, N. K.; Barki, R. R.; Vijayan, A.; Sanjeeva, S. G.; Johnson, R. P. *Eur. J. Pharm. Biopharm.* **2020**.

[127] Zhang, Y. S.; Khademhosseini, A. *Science* . **2017**, *356*, eaaf3627.

[128] Chen, G.; Hoffman, A. S. *Nature* **1995**, *373*, 49–52.

[129] Yoshida, R.; Uchida, K.; Kaneko, Y.; Sakai, K.; Kikuchi, A.; Sakurai, Y.; Okano, T. *Nature* **1995**, *374*, 240–242.

[130] Kim, Y. S.; Liu, M.; Ishida, Y.; Ebina, Y.; Osada, M.; Sasaki, T.; Hikima, T.;

Takata, M.; Aida, T. *Nat. Mater.* **2015**, *14*, 1002–1007.

[131] Dong, L.; Agarwal, A. K.; Beebe, D. J.; Jiang, H. *Nature* **2006**, *442*, 551–554.

[132] Korevaar, P. A.; Kaplan, C. N.; Grinthal, A.; Rust, R. M.; Aizenberg, J. *Nat. Commun.* **2020**, *11*, 1–10.

[133] Suzuki, A.; Tanaka, T. *Nature* **1990**, *346*, 345–347.

[134] Osada, Y.; Okuzaki, H.; Hori, H. *Nature* **1992**, *355*, 242–244.

[135] Miyata, T.; Asami, N.; Uragami, T. *Nature* **1999**, *399*, 766–769.

[136] Miyata, T.; Jige, M.; Nakaminami, T.; Uragami, T. *Proc. Natl. Acad. Sci.* **2006**, *103*, 1190–1193.

[137] Dušek, K.; Patterson, D. *J. Polym. Sci. Part A-2 Polym. Phys.* **1968**, *6*, 1209–1216.

[138] Schild, H. G. *Prog. Polym. Sci.* **1992**, *17*, 163–249.

[139] Matsumoto, K.; Sakikawa, N.; Miyata, T. *Nat. Commun.* **2018**, *9*, 2315.

[140] Maeda, Y.; Higuchi, T.; Ikeda, I. *Langmuir* **2000**, *16*, 7503–7509.

[141] Shibayama, M.; Tanaka, T. In *Responsive gels: volume transitions I*; Springer, **1993**; pp 1–62.

[142] Oya, T.; Enoki, T.; Grosberg, A. Y.; Masamune, S.; Sakiyama, T.; Takeoka, Y.; Tanaka, K.; Wang, G.; Yilmaz, Y.; Feld, M. S.; Dasari, R.; Tanaka, T. *Science* . **1999**, *286*, 1543–1545.

[143] Serpe, M. J.; Yarmey, K. A.; Nolan, C. M.; Lyon, L. A. *Biomacromolecules* **2005**, *6*, 408–413.

[144] Yoshimatsu, K.; Lesel, B. K.; Yonamine, Y.; Beierle, J. M.; Hoshino, Y.; Shea,

K. J. *Angew. Chemie Int. Ed.* **2012**, *51*, 2405–2408.

[145] Geng, H.; Xu, Q.; Wu, M.; Ma, H.; Zhang, P.; Gao, T.; Qu, L.; Ma, T.; Li, C. *Nat. Commun.* **2019**, *10*, 1512.

[146] Hoshino, Y.; Moribe, M.; Gondo, N.; Jibiki, T.; Nakamoto, M.; Guo, B.; Adachi, R.; Miura, Y. *ACS Appl. Polym. Mater.* **2020**, *2*, 505–514.

[147] Hoshino, Y.; Imamura, K.; Yue, M.; Inoue, G.; Miura, Y. *J. Am. Chem. Soc.* **2012**, *134*, 18177–18180.

[148] Jones, C. D.; Lyon, L. A. *Macromolecules* **2000**, *33*, 8301–8306.

[149] Zhou, S.; Chu, B. *J. Phys. Chem. B* **1998**, *102*, 1364–1371.

[150] Suzuki, H.; Wang, B.; Yoshida, R.; Kokufuta, E. *Langmuir* **1999**, *15*, 4283–4288.

[151] Debord, J. D.; Lyon, L. A. *Langmuir* **2003**, *19*, 7662–7664.

[152] der Linden, H. J.; Herber, S.; Olthuis, W.; Bergveld, P. *Analyst* **2003**, *128*, 325–331.

[153] Hoshino, Y.; Ohashi, R. C.; Miura, Y. *Adv. Mater.* **2014**, *26*, 3718–3723.

[154] Hoshino, Y.; Miyoshi, T.; Nakamoto, M.; Miura, Y. *J. Mater. Chem. B* **2017**, *5*, 9204–9210.

[155] Hoshino, Y.; Jibiki, T.; Nakamoto, M.; Miura, Y. *ACS Appl. Mater. & interfaces* **2018**, *10*, 31096–31105.

[156] Yue, M.; Hoshino, Y.; Miura, Y. *Chem. Sci.* **2015**, *6*, 6112–6123.

[157] Tanaka, T.; Sato, E.; Hirokawa, Y.; Hirotsu, S.; Peetermans, J. *Phys. Rev. Lett.* **1985**, *55*, 2455.

[158] Tanaka, T.; Fillmore, D. J. *J. Chem. Phys.* **1979**, *70*, 1214–1218.

[159] Hoshino, Y.; Moribe, M.; Gondo, N.; Jibiki, T.; Nakamoto, M.; Guo, B.; Adachi, R.; Miura, Y. *ACS Appl. Polym. Mater.* **2019**, *2*, 505–514.

[160] Zavgorodnya, O.; Carmona-Moran, C. A.; Kozlovskaya, V.; Liu, F.; Wick, T. M.; Kharlampieva, E. *J. Colloid Interface Sci.* **2017**, *506*, 589–602.

[161] Zhang, H.; Zhai, Y.; Wang, J.; Zhai, G. *Mater. Sci. Eng. C* **2016**, *60*, 560–568.

[162] Molina, M.; Asadian-Birjand, M.; Balach, J.; Bergueiro, J.; Miceli, E.; Calderón, M. *Chem. Soc. Rev.* **2015**, *44*, 6161–6186.

[163] Sasaki, Y.; Akiyoshi, K. *Chem. Rec.* **2010**, *10*, 366–376.

[164] Crespy, D.; Rossi, R. M. *Polym. Int.* **2007**, *56*, 1461–1468.

[165] Motornov, M.; Roiter, Y.; Tokarev, I.; Minko, S. *Prog. Polym. Sci.* **2010**, *35*, 174–211.

Chapter 2. Development of a Thermocell by using Thermal Responsive Hydrogel Nanoparticles

Abstract

Thermoelectric conversion of low temperature, delocalized and abundant thermal sources, is crucial for the development of the Internet of the Things (IoT) and/or carbon free society. Thermocells are of great interest in thermoelectric conversion of low-temperature heat due to the low cost and flexibility of components. However, significant improvement of the conversion efficiency is required for the practical use of the cells. In this study, I report thermo-electrochemical cells driven by volume phase transition (VPT) of thermal responsive hydrogel nanoparticles (NPs). Entropically driven VPT of poly(*N*-isopropylacrylamide) NPs containing carboxylic acids and amines generates a pH gradient of up to 0.049 pH K^{-1} and −0.053 pH K^{-1}, respectively, around physiological temperature. The pH gradient triggers the proton-coupled electron transfer (PCET) reactions of quinhydrone on the electrodes, resulting in the highly efficient thermoelectric conversion with a Seebeck coefficient (S_e) of −6.7 mV K^{-1} and +6.1 mV K^{-1}. Thermocells driven by phase transition of hydrogels provide a non-toxic, flexible, and inexpensive charger that harvests carbon free energy from abundant energy sources such as the solar, body and waste heat.

2.1. Introduction

Energy harvesting from low temperature (< 70 °C), delocalized and abundant thermal sources, such as body heat, solar heat and waste heat is crucial to realize IoT revolution and carbon-free human society[1]–[9]. The development of highly efficient

thermoelectric conversion devices that is small and mass-producible is key for the use of thermal energy[9],[10].

Thermocells, or thermo-electrochemical cells, provide an option for the harvesting low-temperature heat owing to their advantages of low-cost and flexibility of components[9]. Thermocells consist of an aqueous solution of redox-active electrolyte pair and electrodes. The gap of the equilibrium potential of the redox species provided between electrodes in response to temperature difference induces a redox reaction on each electrode resulting in a thermoelectrical conversion. In order to achieve better thermoelectric conversion efficiency, the use of carbon nanotube electrodes with a larger surface area[11], the introduction of host-guest interaction between molecules in the electrolyte[12], and the design of adding a coated porous separation membrane[13] was widely studied. Recently, the conversion efficiency of the thermocells showing a high figure of merit (ZT) of 0.16 with a S_e of −1.4 mV K^{-1} was achieved.[3] However, improvement of S_e is required for the practical use of the cells under the limited temperature difference.

Stimuli-responsive hydrogels are of great interest as materials with dynamic functions[14] because they show a drastic phase transition in response to a small external stimuli such as change in temperature[15]–[20], pH[21],[22], photo irradiation[23]–[25], reduction-oxidation reaction[26], electric field[27], and molecular recognition[28],[29]. Poly(*N*-isopropylacrylamide) (pNIPAM) hydrogels undergoes volume phase transition (VPT) from the swollen phase to the shrunk phase at the temperature around 32 °C as

a result of entropically driven dissociation of water from the polymer chains[30],[31]. The pNIPAM hydrogel with stimuli responsive molecular recognition properties has been developed to reversibly capture and release target molecules such as dyes[32], drugs[33] and proteins[34]. More recently, the gels have been applied as an economical media to extract and/or concentrate moisture[35],[36], salts[37] and carbon dioxide[38] using low temperature waste heat and solar energy as an energy source.

In this study, I took advantage of the quick and reversible pH shift of a solution of thermal responsive hydrogel nanoparticles (NPs) to obtain the thermocells with a high S_e at the temperature around room temperature.[19],[39]–[41] To convert the pH change to a large S_e, quinhydrone, a compound that shows proton-coupled electron transfer (PCET) was selected as the redox species. Through temperature difference-potential difference measurement and maximum output power measurement, a new thermoelectric conversion mechanism based on the PECT reaction and the VPT of NPs is proved.

2.2. Materials and experiments

2.2.1. Materials

The following chemicals and materials were obtained from commercial sources and used as received. *N*,*N*′-methylenebisacrylamide (BIS), cetyltrimethylammonium bromide (CTAB), *N*-[3-(dimethylamino)propyl]methacrylamide (DMAPM) were

obtained from Tokyo Chemical Industry Co., Ltd. HCl, hexane, sodium chloride, acrylic acid (AAc), poly(acrylic acid), sodium dodecyl sulfate (SDS), azobisisobutyronitrile (AIBN) and 4,4'-azobis(4-cyanovaleric acid) (V-501) were obtained from Watanabe Pure Chemical Industry Co., Ltd. NaOH and phosphate buffer (pH = 7.0) were obtained from Kanto Chemical Co., Inc.; *N*-isopropylacrylamide (NIPAM) was obtained from Wako Pure Chemical Industries, Co., Ltd. and recrystallized from hexanes. The dialysis tube (MWCO 12,000–14,000 Da, Spectrum Laboratories, Inc.) was washed with water prior to use. Cation exchange beads (Muromac C1002-H, Muromachi Chemicals, Inc.) and anion exchange beads (Muromachi Technos Co., Ltd., A2004-OH) were pretreated with aqueous HCl (1 M) and then washed with excess water. The water used in this study was purified using a Direct-Q Ultrapure Water System (Merck, Ltd.).

2.2.2. Preparation of NPs

2.2.2.1. Synthesis of NPs containing AAc

NPs consisting of poly(acrylic acid-*co*-*N*-isopropylacrylamide) (AAc NPs) was prepared as reported (Scheme 2-1)[41]–[43]. NIPAM (93 mol%, 3.28 g), BIS (2 mol%, 96 mg), AAc (5 mol%, 285 mg), and SDS (180 mg) were dissolved in 100 mL of water, which resulted in a total monomer concentration of 312 mM. The pH of the solution was adjusted with an HCl solution to 2.6 which was monitored by a pH meter (S50 SevenMulti, Mettler Toledo Co. Ltd.). The reaction mixture was then degassed with

nitrogen flushing for 30 min. Following the addition of V-501 (19.3 mg in 1.96 mL of DMSO), the polymerization was carried out at 70 °C for 3 h under a nitrogen atmosphere. The polymerized solution was purified by dialysis against an excess amount of water (changed more than 3 times a day) for 2 days. Traces of counter anions were removed by strong cation exchange beads (Muromac C1002-H, Muromachi Chemicals, Inc.). The beads were filtered out after exchanging for 1 h.

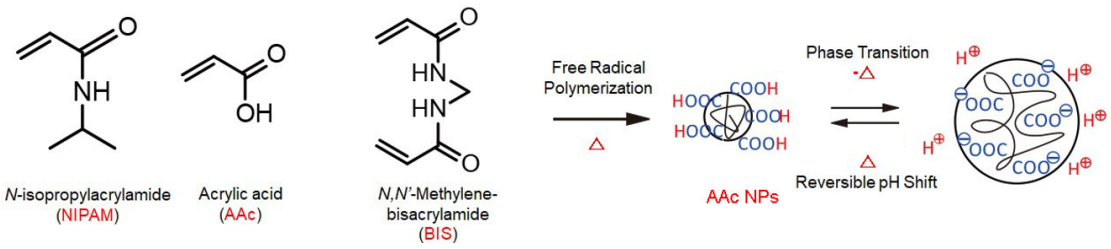

Scheme 2-1. Polymerization process of temperature-responsive hydrogel nanoparticles consisting of AAc. The quick and reversible VPT behavior can lead reversible pK_a change of hydrogel nanoparticles.

The yield of NPs was determined by measuring the weight of NPs obtained by lyophilization of a part of the dialyzed solution. The concentration of NPs treated by the lyophilization method was determined by measuring the moisture absorption and mass after reaching the humidity balance in the air.

2.2.2.2. Synthesis of NPs containing DMAPM

Amine-containing pNIPAM NPs consisting of poly(*N*,*N*-dimethylaminopropyl methacrylamide-*co*-*N*-isopropylacrylamide) (DMAPM NPs) was also prepared as reported (Scheme 2-2)[38],[44]. NIPAM (93 mol%, 3.28 g), BIS (2 mol%, 96 mg), DMAPM (5 mol%, 0.28 mL), and CTAB (73 mg) were dissolved in 100 mL of water, which resulted in a total monomer concentration of 312 mM. The pH of the solution was adjusted with NaOH solution to 10.6 which was monitored by a pH meter (S50 SevenMulti, Mettler Toledo Co. Ltd.). The reaction mixture was then degassed with nitrogen flushing for 30 min. Following the addition of AIBN (11.3 mg in 2 mL of MeOH), the polymerization was carried out at 70 °C for 3 h under a nitrogen atmosphere. The polymerized solution was purified by dialysis against an excess amount of water (changed more than 3 times a day) for 2 days. Traces of counter cations were removed by strong anion exchange beads. The beads were filtered out after exchanging for 1 h.

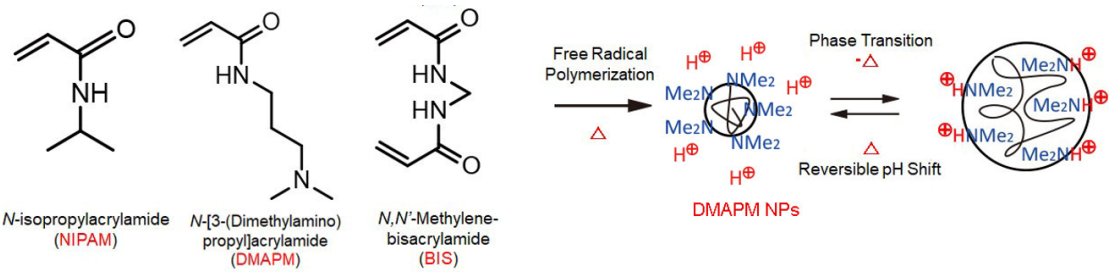

Scheme 2-2. Polymerization process of temperature-responsive hydrogel nanoparticles consisting of DMAPM. The quick and reversible VPT behavior can lead reversible pK_a change of hydrogel nanoparticles.

The yield of NPs was determined by measuring the weight of NPs obtained by lyophilization of a part of the dialyzed solution. The concentration of NPs treated by the lyophilization method was determined by measuring the moisture absorption and mass after reaching the humidity balance in the air.

2.2.3. ^{1}H NMR measurement

Lyophilized powder of NPs was dissolved in CD_3OD (50 mg mL^{-1}). Proton nuclear magnetic resonance (^{1}H NMR) experiments were conducted on a JEOL JNM-ECP400 instrument at 25 °C. The trace of the surfactant remaining in the NPs was determined from the results of NMR.

2.2.4. Quantification of VPT temperature and hydrodynamic diameter of NPs

VPT behavior of the sample was confirmed by a dynamic light scattering (DLS) instrument (Zetasizer Nano, Malvern Instruments Limited) using the ion-exchanged solutions. The solution was equilibrated at each temperature for 2 min prior to the measurement. VPT temperature was determined as the temperature where the plateau of relative scattering intensity started. The relative scattering intensity was defined by Eq. 2-1:

$$Relative \text{ scattering } intensity = \frac{I - I_{min}}{I_{max} - I_{min}} \quad \text{Eq. 2-1}$$

where I is the intensity. Hydrodynamic diameters of NPs were also measured by DLS as a function of temperature.

2.2.5. Quantification of carboxylic acid or amine concentration in NPs

The concentration of the carboxylic acid of the AAc NP was estimated by acid–base titration using aqueous NaOH at 30 and 70 °C with stirring at 500 rpm. A pH meter (S50 SevenMulti, Mettler Toledo Co. Ltd.) equipped with pH probes (InLab Routine Pro, Mettler Toledo Co. Ltd.) was calibrated with standard buffers (pH = 4.01, 7.00, and 9.21) prior to use. Temperature of NP solution was controlled by water bath. According to the mass concentration of NPs, the concentration of carboxyl groups in the original solution of AAc NPs can be calculated. The similar method of acid-base titration was applied to measure the concentration of the amine in DMAPM NPs. Instead of NaOH, aqueous HCl was used in the titration experiment. To prevent alkaline NPs (DMAPM NPs) from absorbing carbon dioxide in the air and affecting the results of the neutralization titration, DMAPM NPs were titrated in a nitrogen atmosphere.

2.2.6. Measurement of pK_a shift curve in heating process

Apparent pK_a of the acids/amine in NPs is equal to the pH value at the half neutralization point. pK_a shift curve was measured with a pH probe by the following

method: half neutralized NP solution was prepared by adding 0.5 equivalents of NaOH and HCl for AAc NPs and DMAPM NPs, respectively. Then pH value and temperature of NP solution every 3 seconds during temperature swing process was recorded by the pH probe with stirring 500 rpm. To prevent DMAPM NPs from absorbing carbon dioxide in the air and affecting the results of the neutralization titration pH, a nitrogen atmosphere was applied during temperature swing. Temperature change was controlled by a synthesis plant (Eyela PPW-200, Tokyo Rikakikai Co., Ltd.).

2.2.7. Preparation of poly(AAc) and poly(DMAPM)

Poly(acrylic acid) (MW 25000) was dissolved in water to prepare poly(AAc) solution. Poly(DMAPM) was synthesis by simple radical polymerization. DMAPM (312 mM, 5.6 mL) was dissolved in 100 mL of water. The pH of the solution was adjusted with HCl solution to 7.8 which was monitored by a pH meter (S50 SevenMulti, Mettler Toledo Co. Ltd.). The reaction mixture was then degassed with nitrogen flushing for 60 min. Following the addition of APS (22.8 mg in 1 mL of water), the polymerization was carried out at 60 °C for 22 h under a nitrogen atmosphere. The polymerized solution was purified by dialysis against an excess amount of water (changed more than 3 times a day) for 2 days. Finally, a light yellow transparent poly(DMAPM) aqueous solution can be obtained.

2.2.8. Measurement of thermoelectric voltage

Experimental apparatus for voltage measurement (Figure 2-1a) was made up of the following components. 10 mL of electrolyte solutions were put into water jacket glass cells (Φ 25.6 mm * h 50 mm). Two mix stirrers (Φ 5 mm * 20 mm) were added in each half cell. Each cell was covered with a 3-hole teflon cap, where a platinum working electrode was immersed into the electrolyte solution. A 25 cm silicon tube salt bridge containing agar gel with 3 M potassium chloride solution was inserted through 3-hole teflon cap to connect two cells (Figure 2-1b). And a thermocouple was inserted into the electrolyte solution in each cell. Temperature of each cell was controlled separately by using an external thermostatic device to circulate water into the water jacket of each cell. The terminals of the source meter 2401 (Keithley) were connected to the electrodes of each cell. DC voltage measurement mode (mV) for displaying the voltage was set. Before the measurement was started, the carbon dioxide and oxygen in the electrolyte solution were removed by nitrogen bubbling for 30 minutes to prevent pH change and oxidation of electrolyte solution. After confirming that the inside of both cells was stabilized at 20 °C., gradually raise the temperature of the jacket water of one cell until it reached 70 °C. The difference in temperature and the voltage between the hot and cold cell sides was plotted, and the S_e was estimated from the slope of the plot.

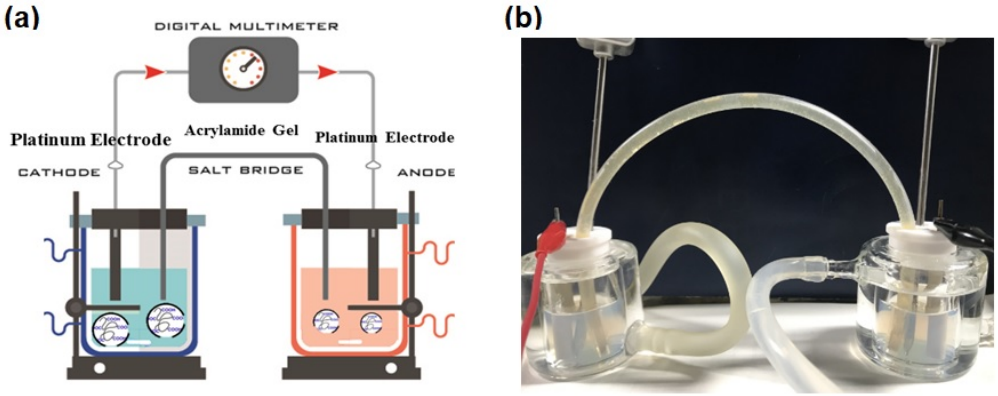

Figure 2-1. (a) Diagram of salt the bridged thermocell. (b) Photograph of a bridged thermocell design for thermoelectric voltage mesurement.

Quinhydrone, which is an equimolar mixture of *p*-quinone and *p*-hydroquinone and shows a reversible two-proton-two-electron PCET reaction (Scheme 2-3), was used as redox species in electrolyte solution. 5.6 mM of quinhydrone and various concentrations of NPs were dissolved into milli-Q water. The pH of each cell was adjusted by the addition of half an equivalent of NaOH and HCl for AAc NPs and DMAPM NPs, respectively. For the cell without NPs, an aqueous solution of quinhydrone (5.6 mM) and HCl was added to adjust the pH to 4.2.

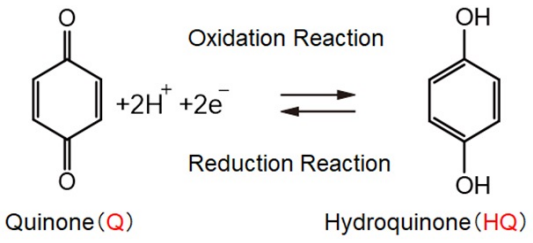

Scheme 2-3. A reversible PCET reaction of *p*-hydroquinone and *p*-quinone.

2.2.9. Measurement of thermoelectric current and power

The experimental apparatus for the thermocell performance measurements (Figure 2-2a) was made up of the following components. A home-made H-shape glass tube with an inner diameter of 20 mm was used as the thermocell and 35 mL of electrolyte solutions were added into it (Figure 2-2b). Each side of the container was soaked in coolant or a heater, respectively, to control the temperature of each side separately. Platinum wires (1 mm in diameter and 80 mm in length) were washed by soaking them in concentrated sulfuric acid and these were rinsed with ultrapure water before use. Two platinum wires were immersed into the electrolyte solution, and the current between the wires were measured with a source meter 2401 (Keithley). The temperature at both sides of the cell was monitored during the measurement with two thermometers (TM-201). The temperature of the cold side of the container was kept at approximately 20 °C and the solution was magnetically stirred during the measurement.

Various concentrations of quinhydrone and NPs were dissolved into milli-Q water. The pH of each cell was adjusted by the addition of half an equivalent of NaOH and HCl for AAc NPs and DMAPM NPs, respectively. Various concentrations of KCl were added to improve ionic conductivity. For the cell without NPs, an aqueous solution of quinhydrone (5.6 mM) and HCl was added to adjust the pH to 4.2.

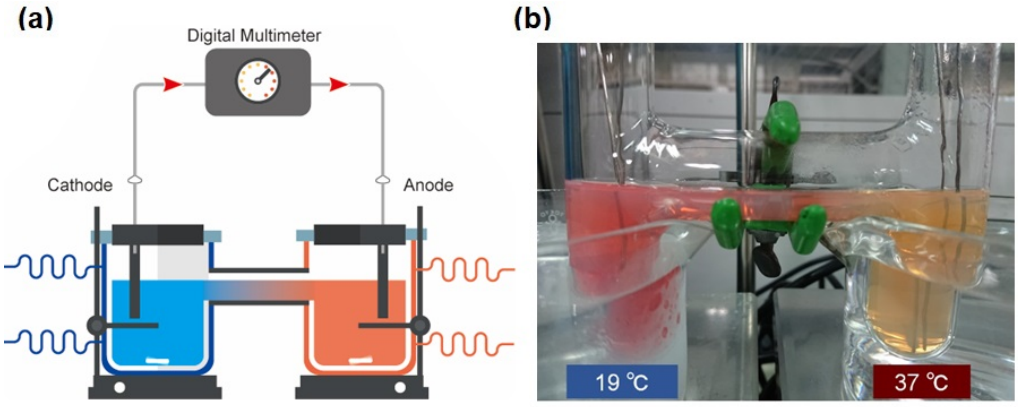

Figure 2-1. (a) Diagram of the H-shape cell for current and output power measurement. (b) Photograph of H-shape thermocell consisting AAc NPs for current measurement. Methyl orange was added to the cell to visualize the pH difference between both sides of the cell.

2.2.10. Measurement of electrical and thermophysical property

The ionic conductivity of the electrolyte solutions was measured by an electric conductivity meter (SevenMulti Dual Digital Meter with Conductivity and pH Modules, Mettler Toledo) with a Mettler-Toledo Conductivity TDS/SAL/Resistivity Module. The thermal conductivity of the samples was measured by a transient plane source technique by a hot disk thermal constants analyzer (Hot Disk TPS 500, Kyoto Electronics) with a #7577 sensor at ambient temperature. 40 mL of electrolytes were used, and each measurement was repeated 10 times with a 1-min interval.

2.2.11. Measurement of Zeta potential of NPs solution

The Zeta potential of the NPs solutions was measured by a dynamic light scattering (DLS) instrument (Zetasizer Nano, Malvern Instruments Limited) using zeta potential measurement mode. 10 mM phosphate buffer (pH=7.0) solutions was used to prevent the influence of pH changes in the NP solution.

2.3. Results and Discussion

2.3.1. Preparation of NPs

AAc NPs and DMAPM NPs that undergoes the VPT in aqueous media at a temperature around 40 °C was prepared as reported.[38],[42]–[44] By measuring the weight of NPs obtained by lyophilization of a part of the dialyzed solution, the yield of NPs was obtained as 79.4% and 84.6% for AAc NPs and DMAPM NPs, respectively. The ^{1}H NMR results of AAc NPs (Figure 2-3a) and DMPAM NPs (Figure 2-3b) showed that the surfactant remaining in NPs was too little to affect the thermal response performance of NPs. Two signals were observed at 1.4 ppm and 4.0 ppm in both NMR results, corresponding to -CH_2- and -CH- in the NIPAM side chain, respectively.

(a)

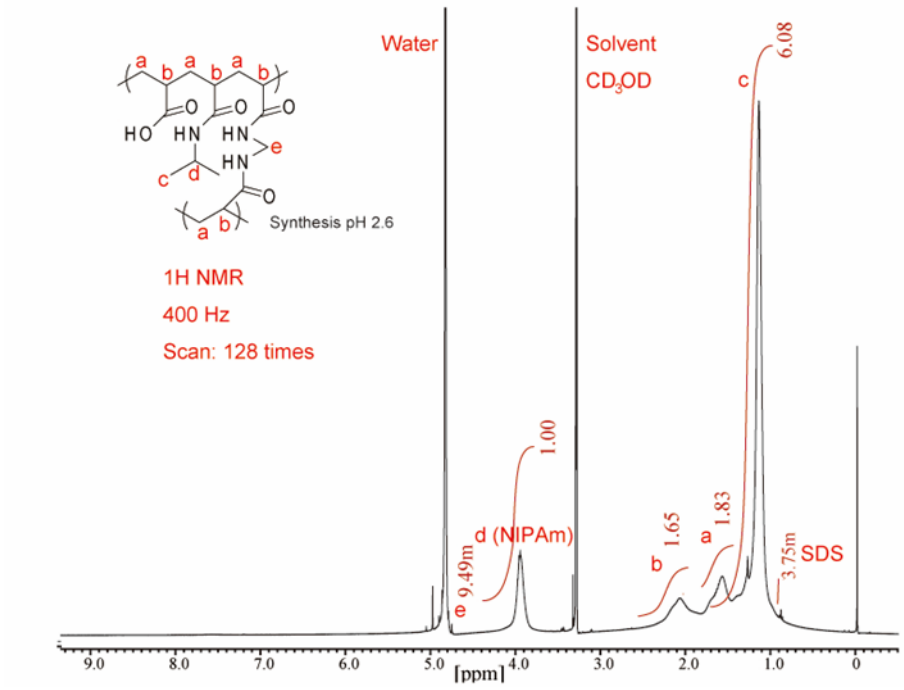

(b)

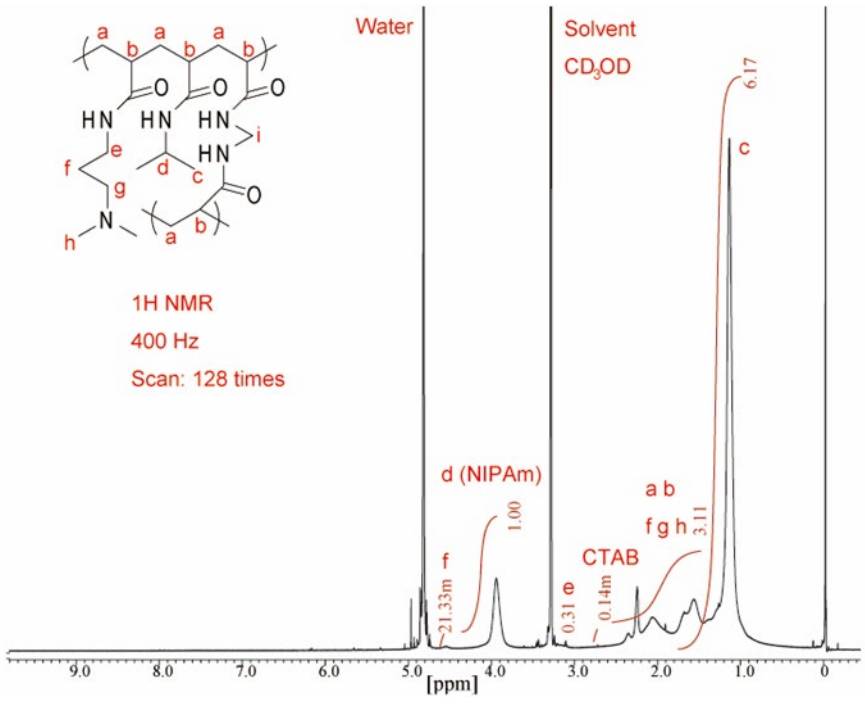

Figure 2-3. ^{1}H NMR results of (a) AAc NPs and (b) DMAPM NPs.

The concentration of AAc NPs (27.05 mg mL^{-1}) and DMAPM NPs (30.76 mg mL^{-1}) treated by the lyophilization method were determined by measuring the moisture absorption and mass after reaching the humidity balance in the air.

2.3.2. VPT behavior of NPs

Figure 2-4 shows a plot of the hydrodynamic diameter of NPs obtained by DLS as a function of temperature. The average diameters of the polymer chains decreased during the VPT, which corresponded to the dehydration of the polymer chains above approximately 30 °C. The VPT temperatures of AAc NPs and DMAPM NPs were measured as 32 °C and 40 °C, respectively.

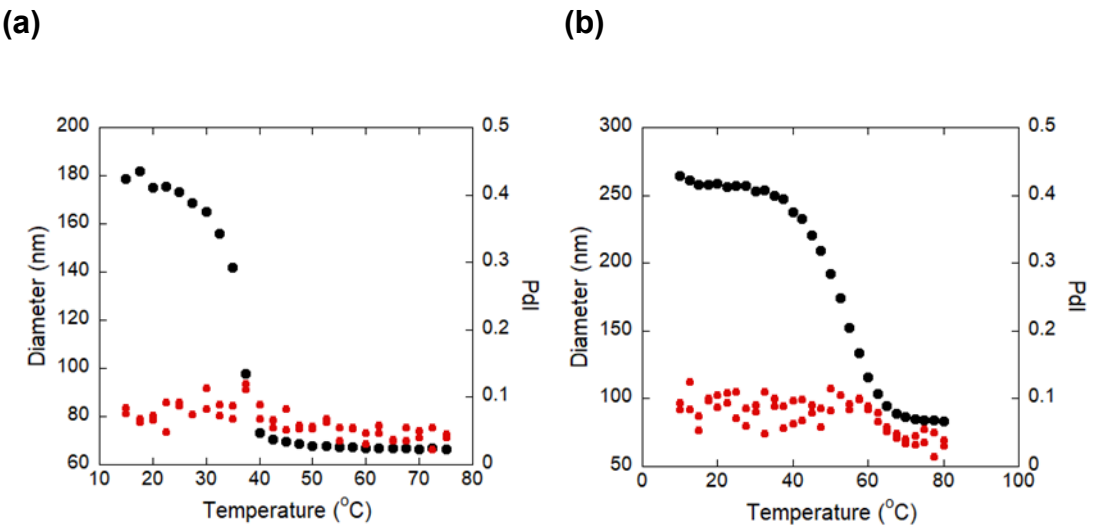

Figure 2-4. Change of mean-diameter of (a) AAc NPs (1.0 mg/mL) and (b) DMAPM NPs (1.0 mg/mL) estimated from DLS measurements with the change in temperature.

In addition, DLS hydrodynamic diameter distribution of NPs between 20 °C and 50 °C was shown in Figure 2-5. Through the experimental results, it can be observed that the hydrodynamic diameter distribution of NPs changes greatly with the change of temperature, which is attributed to the VPT process. In the swollen phase, pNIPAM is hydrated, and thus, microenvironment around the acids in the NPs is hydrophilic. However, at temperatures above the VPT temperature, NPs shrinks as a result of entropically driven dissociation of water molecules from pNIPAM, and the environment around the acids becomes hydrophobic[41]–[43].

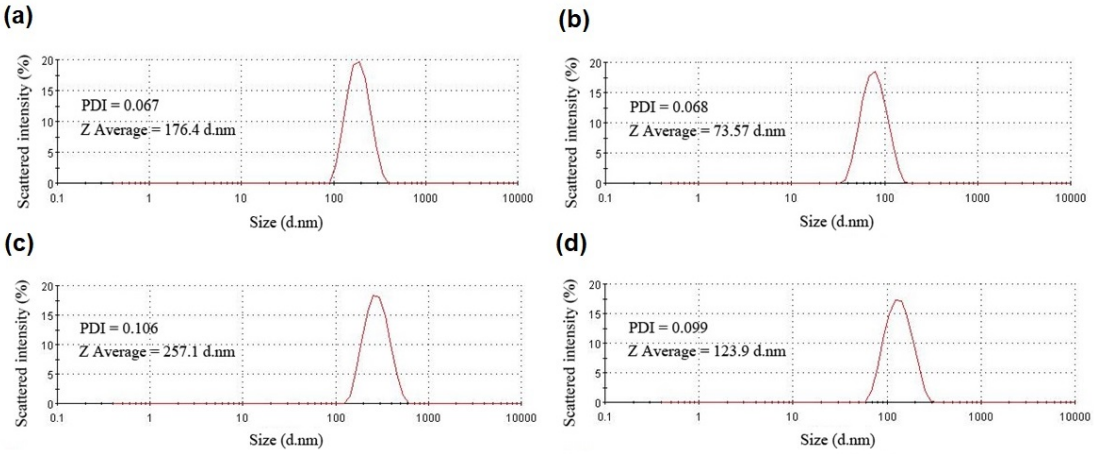

Figure 2-5. DLS hydrodynamic diameter distribution of (a) AAc NPs (1.0 mg/mL) at 20°C, (b) AAc NPs (1.0 mg/mL) at 50 °C, (c) DMAPM NPs (1.0 mg/mL) at 20 °C and (d) DMAPM NPs (1.0 mg/mL) at 50 °C.

2.3.3. Acid–base titration results of NPs

The concentration of the carboxylic acid of the AAc NPs was estimated to be 335.6 μmol/g by acid–base titration using aqueous NaOH at 30 and 70 °C (Figure 2-6a). According to the mass concentration of AAc NPs (27.05 mg mL^{-1}), the concentration of carboxyl groups in the original solution of NPs can be calculated (9.08 mM). Through the similar titration experiment, the concentration of the amine of DMAPM NPs was estimated by acid–base titration using aqueous HCl at 30 and 70 °C (Figure 2-6b) to be 390.3 μmol/g. According to the mass concentration of DMPAM NPs (30.76 mg mL^{-1}), the concentration of amino groups in the original solution of NPs can be calculated (12.0 mM).

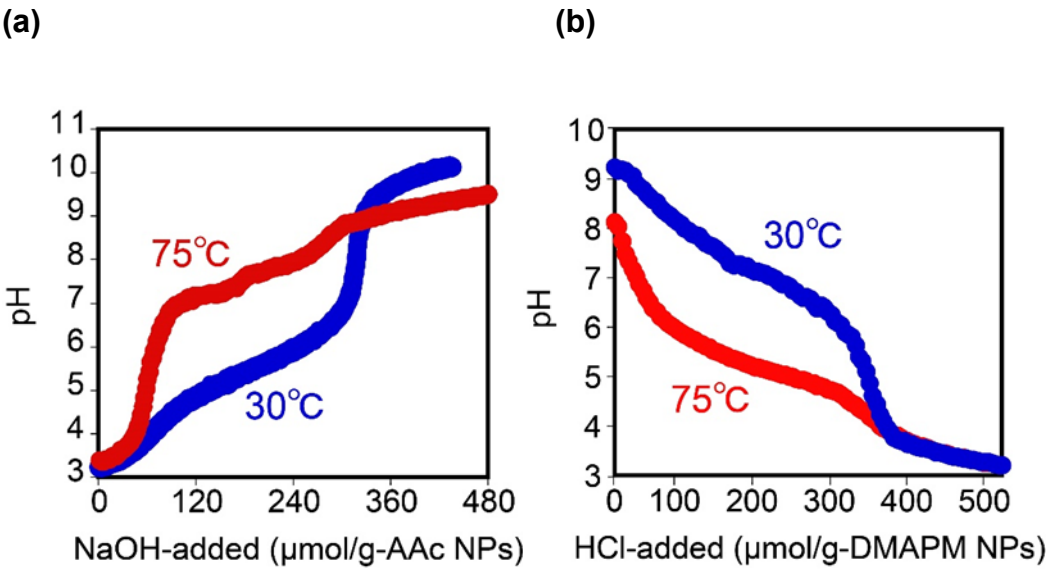

Figure 2-6. Titration curves of (a) AAc NPs (4.0 mg/mL) and (b) DMAPM NPs (4.0 mg/mL) at 30 (blue) and 75 °C (red). The horizontal axis is the amount of added NaOH

and HCl for AAc NPs and DMAPM NPs, respectively. By determining the neutralization point, the amount of carboxy and amino groups contained in NPs can be calculated

Amount and pK_a of acids in NPs were determined by acid base titration. When pH of the solution was adjusted by strong base (NaOH) to be equal to the pK_a of AAc in the NPs, the environmental change induced significant pH change of the NPs solution from pH 5 to pH 7 by elevating the temperature from 30 to 50 °C associating with the pK_a shift of acids in the particles (Figure 2-7, blue line).[42],[43] The solution of DMAPM NPs showed a large pH shift in which the direction is contrary to the acid-containing NPs (Figure 2-7, red line).[38],[43],[44]

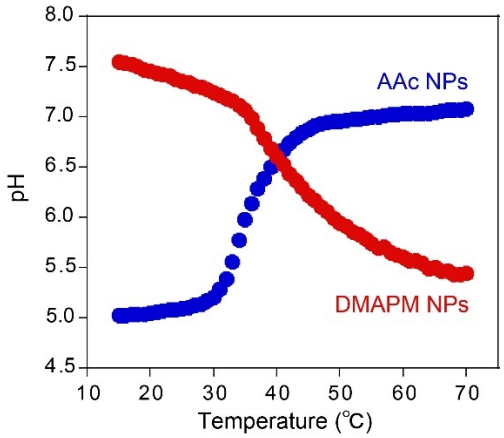

Figure 2-7. Temperature dependent pH change of AAc NPs ([AAc] = 2 mM, [NaOH] = 1 mM) (blue) and DMAPM NPs ([DMAPM] = 2 mM, [HCl] = 1 mM) (red) solutions.

2.3.4. Thermoelectric voltage of thermocells driven by the VPT of AAc NPs

In order to convert the pH change to a large S_e, quinhydrone, which shows a reversible two-proton-two-electron PCET reaction was selected as redox species in thmocell electrolyte solution. At ambient temperature, the equilibrium potential of quinhydrone shifts by changing the concentration of protons (pH) for 59 mV pH^{-1}.[45] Thus, if the pH of one side of the cell is different from the other side, a large shift of equilibrium potential will be observed.

Quinhydrone thermocells were constructed using a set of jacketed cells and platinum electrodes connected with a salt bridge (Figure 2-1a, 2-1b). The open-circuit voltage between the two electrodes was measured during the heating of one of the cells from 20 °C to 70 °C (Figure 2-8, blue line). An open-circuit voltage of 152 mV was observed when adding AAc NPs into the quinhydrone electrolyte. The average S_e over the whole temperature range was −3.0 mV K^{-1}, and the highest S_e of −6.7 mV K^{-1} was observed between 36 and 40 °C (Figure 2-8, blue line). This behavior is similar to the temperature-dependent pH profile of the solution (Figure 2-7, blue line), which reflects the VPT process of AAc NPs.

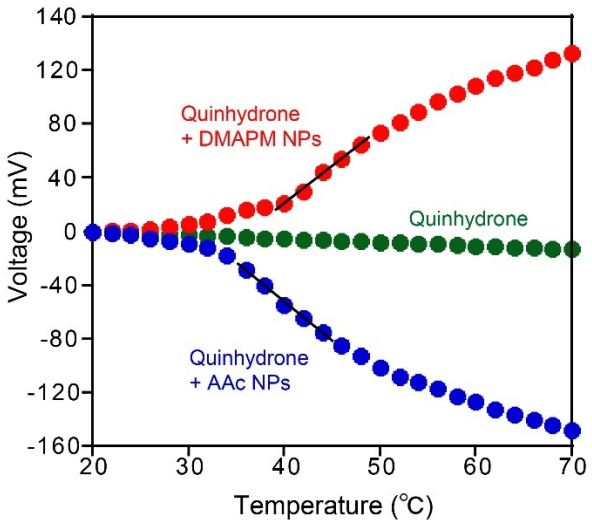

Figure 2-8. Open circuit voltage of quinhydrone (5.6 mM) themocells constructed without NPs (green), and with AAc NPs ([AAc] = 2 mM, [NaOH] = 1 mM) (blue), DMAPM NPs ([DMAPM] = 2 mM, [HCl] = 1 mM) (red). The slope of the curves corresponds to the Seebeck coefficient (S_e). Quinhydrone solution (5.6 mM) showed S_e of −0.72 mV K^{-1}, while addition of AAc NPs resulted in an average S_e of −3.0 mV K^{-1} and maximum S_e of −6.7 mV K^{-1} between 36 and 40 °C. Addition of DMPAM NPs resulted in an average S_e of +2.6 mV K^{-1}, and maximum S_e of +6.1 mV K^{-1} between 42 and 46 °C.

The mechanism was supported by additional experiments using thermocells consisting of the amine containing DMAPM NPs. The cells prepared with DMAPM NPs showed a large voltage in which the direction is contrary to the ones with acid-containing NPs. The average S_e over the whole temperature range was +2.6 mV K^{-1} and the highest S_e of +6.1 mV K^{-1} was observed at the temperature between 42 and

46 °C (Figure 2-8, red line). This is three times higher positive S_e value than the highest ever reported values among liquid-state thermocells.[46]

To establish importance of pH shift on the generation of the large S_e value, two quinhydrone thermocells with AAc NPs which pH is adjusted to be pH 4.4, 5.0 and 8.8 at 20 °C were prepared by adding appropriate amount of NaOH. When pH of the quinhydrone-AAc NPs electrolyte was adjusted to be far from pK_a of the acids in the NPs, significant decrease in S_e was observed, indicating importance of large pH gradient formed by acids in the NPs. (Figure 2-9). It should be noted that this is the highest negative S_e value ever reported among conventional liquid-state thermocells (the previously reported S_e values are listed in Table 1-4).

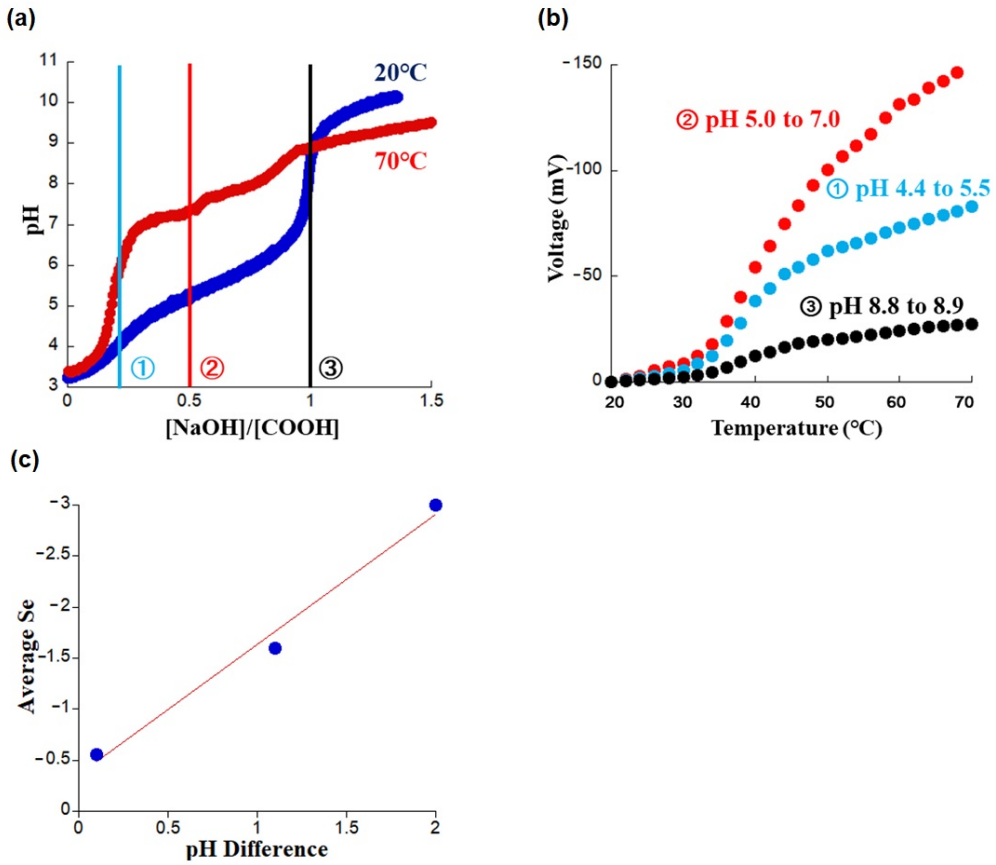

Figure 2-9. (a) Titration curves of AAc NPs at 20 °C and 70 °C. Appropriate amount of NaOH, shown as ①②③, was added in order to prepare thermocells which pH is 4.4, 5.0 and 8.8, respectively at 20 °C. (b) Open circuit voltage of quinhydrone (5.6 mM) themocells constructed with AAc NPs ([AAc] = 2 mM) and 0.4 mM (①blue), 1 mM (②red) and 2 mM (③black) of NaOH. The slope of the curves corresponds to the Seebeck coefficient (S_e). The average S_e of −1.6 mV K^{-1} and −0.6 mV $K^{-1}$was observed upon the heating process of ① and ③, respectively, which were significantly smaller than that of the cell ② which pH was adjusted to be equal to the pK_a of AAc in the NPs (pH = 5.0, S_e = −3.0 mV K^{-1}). (c) The average S_e of thermocells as a function of pH difference. Temperatures of cold and hot electrodes are 20 °C and 70 °C, respectively.

2.3.5. Control experiments using poly(AAc) and poly(DMAPM)

Additional control experiments using thermocells consisting of poly(NIPAM) NPs without AAc, poly(AAc) without NIPAM and ploy(DMPAM) without NIPAM were performed to prove that the driven force of the themocell is the pH change due to VPT of NPs. The cells consisting of poly(NIPAM) NPs, poly(AAc) and poly(DMAPM) did not show temperature-dependent large pH changes (Figure 2-10a). And thus, this cell did not show the large S_e as expected (Figure 2-10b). These results support the proposed mechanism in which the VPT of the hydrogel NPs drives a large S_e of quinhydrone thermocells through the formation of a proton concentration gradient.

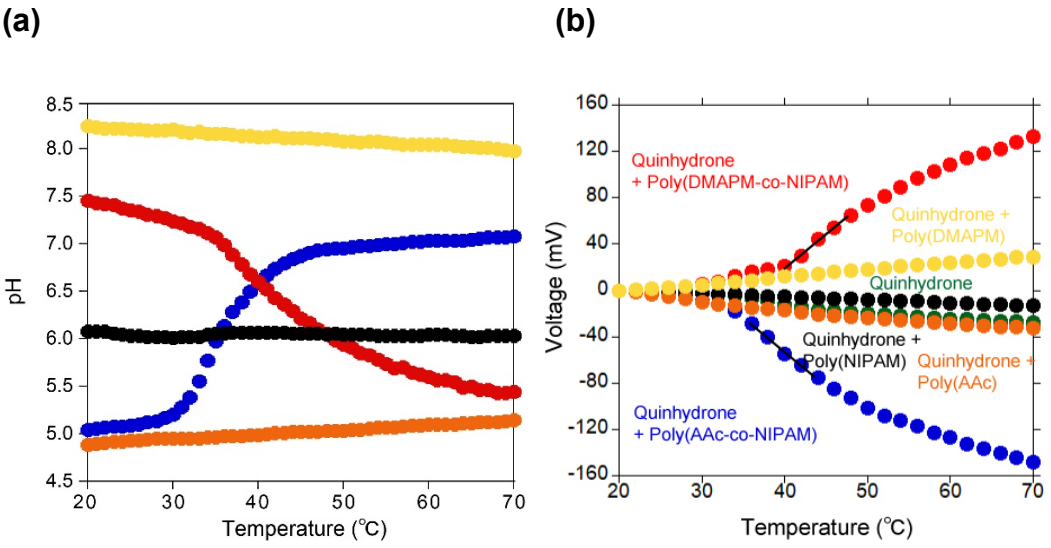

Figure 2-10. (a) Temperature dependent pH change of AAc NPs ([AAc] = 2 mM, [NaOH] = 1 mM) (blue), poly(NIPAM) NPs (5.9 mg/mL) (black), poly(AAc) (5.9

mg/mL) (orange), poly(DMAPM) (5.9 mg/mL) (yellow) and DMAPM NPs ([DMAPM] = 2 mM, [HCl] = 1 mM) (red) solutions. (b) Open circuit voltage of quinhydrone (5.6 mM) themocells constructed without NPs (green), and with AAc NPs ([AAc] = 2 mM, [NaOH] = 1 mM) (blue), DMAPM NPs ([DMAPM] = 2 mM, [HCl] = 1 mM) (red), poly(NIPAM) NPs (5.9 mg/mL) (black), poly(AAc) (5.9 mg/mL) (orange) and poly(DMAPM) (5.9 mg/mL) (yellow). The slope of the curves corresponds to the Seebeck coefficient (S_e).

2.3.6. Thermoelectric current and power of thermocells driven by the VPT of NPs

The current output of the quinhydrone thermocell containing AAc NPs was investigated by applying an external load voltage using an H-shape glass tube and platinum wire electrodes (Figure 2-2).[12],[47] The open-circuit voltage increased with increasing the temperature difference (Figure 2-11). The power output was estimated to be 0.23 μW m^{-2} K^{-2} from the *I–V* measurements when the temperatures of cold and hot cells were 20 °C and 50 °C, respectively (Figure 2-12a). Stability of the voltage was evaluated (Figure 2-12b), and no obvious degradation was observed at least for 700 min. The power will further be improved by optimizing electrode and cell structure.[3] Furthermore, the current output of the quinhydrone thermocell containing DMAPM NPs was comparable with that of AAc NPs (Figure 2-12c). Stability of the voltage was also evaluated (Figure 2-12d). As the same result, no obvious degradation was observed at least for 700 min.

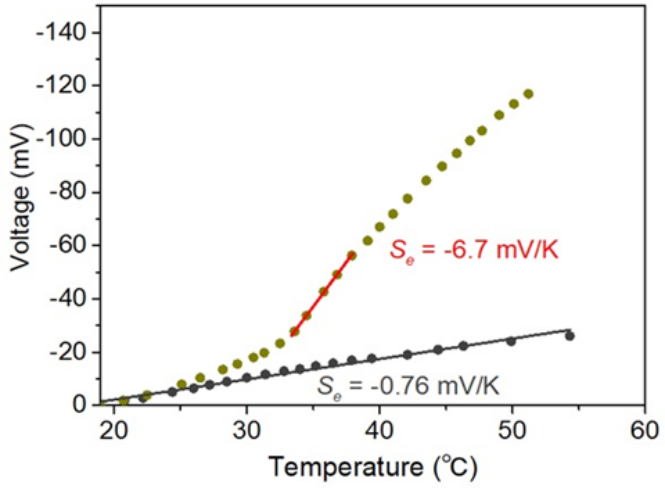

Figure 2-11. Open circuit voltage of quinhydrone (5.6 mM) themocells constructed without NPs (black), and with AAc NPs ([AAc] = 2 mM, [NaOH] = 1 mM) (green) measured by H-shape cell. The slope of the curves corresponds to the Seebeck coefficient (S_e).

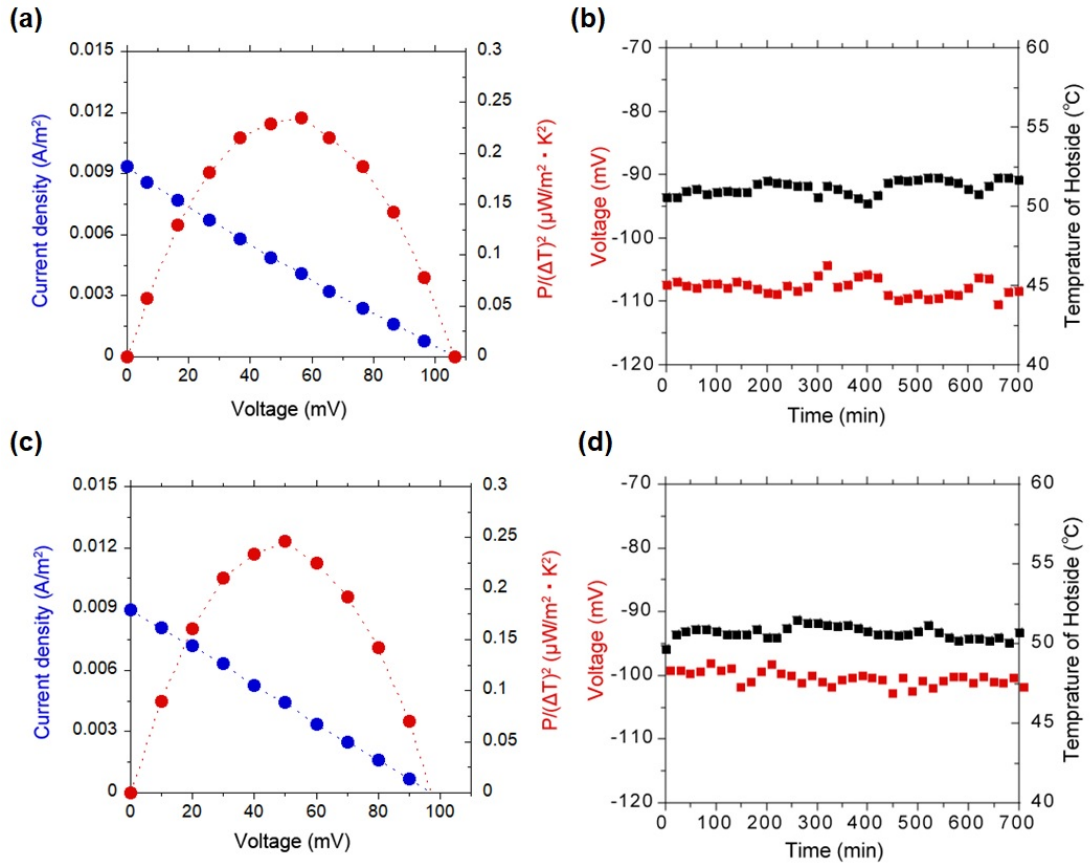

Figure 2-12. (a) *I–V* and *P–V* plots of thermocell consisting of quinthdrone (5.6 mM) with AAc NPs (5.9 mg/mL, [AAc] = 2 mM, [NaOH] = 1 mM). (b) Time dependency of thermocell voltage, respectively. Temperatures of cold and hot cells were 20 °C and 50 °C, respectively. (c) *I–V* and *P–V* plots of thermocell consisting of quinthdrone (5.6 mM) with DMAPM NPs (5.9 mg/mL, [DMAPM] = 2 mM, [HCl] = 1 mM). (d) Time dependency of thermocell voltage, respectively. Temperatures of cold and hot cells were 20 °C and 50 °C, respectively.

Proposed mechanism of the thermocell is shown in Scheme 2-4. When the NPs around the hot electrode were heated, pH of the electrolyte solution increased because protons were captured by the shrunk NPs. Decrease of proton concentration shifted the

equilibrium of the PCET reaction of quinhydrone to the side of *p*-quinone, driving electron transfer from hydroquinones to the hot electrode. On the other hand, pH around the cold electrode became lower because of the protons released from the swollen NPs. The high concentration of protons promoted the reduction of *p*-quinone to hydroquinone on the cold electrode. The preference of the redox equilibrium was affected by the concentration of protons by 59 mV pH^{-1} for the two-proton-two-electron reaction according to the Nernst equation.[45] Therefore, a voltage of about 120 mV was generated when the pH was changed by about 2 (Figure 2-10b).

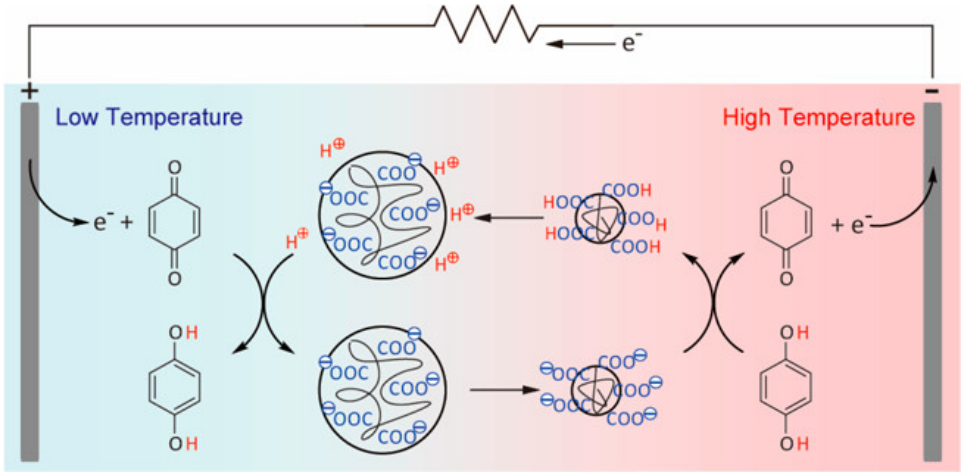

Scheme 2-4. Proposed mechanism for thermocells driven by phase transition of hydrogel nanoparticles.

My results also show that both *p*-type and *n*-type thermocells with high S_e can be obtained by the same strategy with a simple change of the functional group in the NPs. By connecting *p*-type and *n*-type components, a π-connection system of thermocells that shows minimum loss of thermal energy can be designed (Figure 2-14).[48]

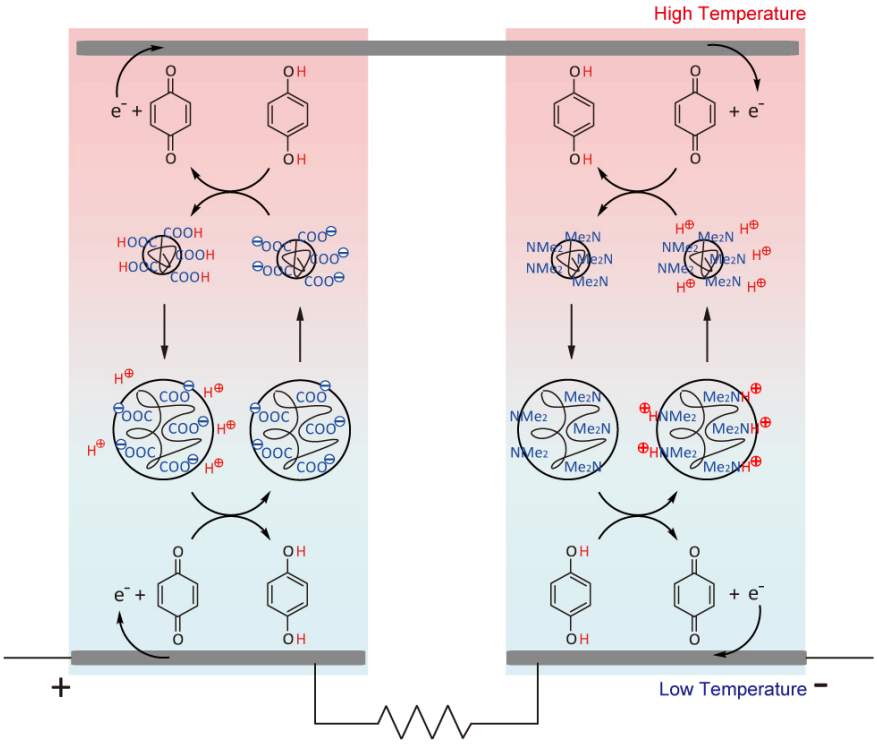

Figure 2-14. Schematic illustration of the p- and n-type thermocell consisting of thermo-responsive NPs and their serial π-type connection.

2.3.7. Zeta potential of NPs solution

In addition, due to the amount of charge of NPs represented by the zeta potential will be able to distinguish the stability and charged state of the particles to a large extent. Temperature-dependence of zeta-potential of the AAc NPs and DMPAN NPs can theoretically support the proposed mechanism of the thermocell shown in Scheme 2-4. The zeta potential of NPs was measured and showed the results in Table 2-1.

Table 2-1. Zeta potential of NPs solution at different temperature and pH value.

Sample Name	NPs Concentration (mg/mL)	Solution pH	Zeta Potential (mV) [b]	
			20 °C	70 °C
AAc NPs	1.0	7.0 [a]	-5.95	-11.4
DMAPM NPs	1.0	7.0 [a]	0.173	0.567

[a] Measured in 10 mM phosphate buffer (pH=7.0) solutions.

[b] Average ± standard deviation of three sequential measurements. Data may include inaccuracy due to polydispersity.

The results show that AAc NPs are negatively charged, and DMAPM NPs are positively charged. However, NPs can only show a small absolute value of zeta potential under different temperature environments, and the value of zeta potential is outside the range of stability behavior (± 30 mV). Even if the temperature of the NPs

solution is changed, an analytically meaningful zeta potential value cannot be measured by my experimental device. This may be caused by more complicated reasons.

2.3.8. Electrical and thermophysical property and *ZT* of thermocells driven by the VPT of NPs

The performance of thermoelectric devices is evaluated by the dimensionless *ZT* value from Eq. 2-2, which is determined by S_e, ionic conductivity (σ), an average of the absolute temperature (T) and thermal conductivity (k).

$$ZT = \frac{\sigma S_e^2}{\kappa} T \qquad \text{Eq. 2-2}$$

Thus, σ and k values of each electrolyte were measured, and apparent *ZT* values were estimated.

As summarized in Table 2-2, both S_e and σ value drastically improved from −0.72 mV K^{-1} and 8.7×10^{-3} S m^{-1} to −6.7 mV K^{-1} and 5.3×10^{-2} S m^{-1}, respectively, by the addition of the AAc NPs at 311 K. As a result, the *ZT* value improved by two orders of magnitude from 2.0×10^{-6} to 8.8×10^{-4} by the NPs. Furthermore, as reported previously,[5] *ZT* value was improved by two more orders by the addition of KCl as a supporting electrolyte that increases ionic conductivity (Table 2-2). According to these two methods, the highest *ZT* value of 2.4×10^{-2} was achieved by the thermocells consisting of AAc NPs and quinhydrone (Table 2-2). The same trend was observed when using DMAPM NPs at 317 K. The highest *ZT* value achieved by DMAPM NPs

was 5.4×10^{-2}. It should be noted that my cell configuration was specialized for a precise S_e measurement, and the *ZT* value will be further improved by optimizing the choice of electrodes and structure of cells.[3],[13],[49]–[51]

Table 2-2. Electrical and thermophysical property and figure of merit of the electrolytes in quinhydrone (5.6 mM) thermocells.

AAc NPs (mM)	DMPAM NPs (mM)	KCl (mM)	σ (S m^{-1})	S_e (mV K^{-1})	κ (W m^{-1} K^{-1})	*ZT*
0*[1]	0	0	8.7×10^{-3}	−0.72	0.71	2.0×10^{-6}
2.0	0	0	4.3×10^{-2}	−6.7	0.68	8.8×10^{-4}
2.0	0	50	8.6×10^{-1}	−6.0	0.73	1.3×10^{-2}
2.0	0	100	NA*[2]	NA*[2]	NA*[2]	NA*[2]
1.0	0	100	1.6	−5.9	0.72	2.4×10^{-2}
0	2.0	0	3.9×10^{-2}	6.1	0.64	7.2×10^{-4}
0	2.0	50	7.6×10^{-1}	7.3	0.64	2.0×10^{-2}
0	2.0	100	NA*[2]	NA*[2]	NA*[2]	NA*[2]
0	1.0	100	1.5	8.9	0.70	5.4×10^{-2}

*[1] pH of the solution was adjusted by the addition of of HCl to be pH=4.2.

*[2] NPs are precipitated.

2.4. Conclusions

In summary, thermocell for energy harvesting at physiological temperature with high conversion efficiency was achieved by combining PCET reactions of redox-active electrolyte pair quinhydrone and VPT of hydrogel NPs. This thermocell shows a high S_e of −6.7 mV K^{-1} and +6.1 mV K^{-1}, which is beyond the maximum value ever reported for liquid-state thermocells. This high pH change of the solution induced by entropy driven VPT of NPs was crucial for the efficient thermoelectric conversion. Furthermore, by the improvement of ionic conductivity, a ZT value of 5.4×10^{-2} was obtained, which is high for liquid-based thermoelectric materials without using sophisticated electrodes. The success of this concept involving entropy-driven phase transition opens a new arena for investigating high performance thermocells. I believe that the strategy enables a non-toxic, flexible, and inexpensive charger for wireless devices, including portable devices and sensors, that harvests energy from low-grade but abundant energy sources such as the solar, body and waste heat.

2.5. Reference

[1] Chu, S.; Cui, Y.; Liu, N. *Nat. Mater.* **2017**, *16*, 16–22.

[2] Liu, W.; Hu, J.; Zhang, S.; Deng, M.; Han, C.-G.; Liu, Y. *Mater. Today Phys.* **2017**, *1*, 50–60.

[3] Im, H.; Kim, T.; Song, H.; Choi, J.; Park, J. S.; Ovalle-Robles, R.; Yang, H. D.; Kihm, K. D.; Baughman, R. H.; Lee, H. H.; Kang, T. J.; Kim, Y. H. *Nat. Commun.* **2016**, *7*, 10600.

[4] Rowe, D. M. *Renewable Energy*. **1999**, pp 1251–1256.

[5] Im, H.; Moon, H. G.; Lee, J. S.; Chung, I. Y.; Kang, T. J.; Kim, Y. H. *Nano Res.* **2014**, *7*, 443–452.

[6] Yang, P.; Liu, K.; Chen, Q.; Mo, X.; Zhou, Y.; Li, S.; Feng, G.; Zhou, J. *Angew. Chemie Int. Ed.* **2016**, *55*, 12050–12053.

[7] Hu, G.; Edwards, H.; Lee, M. *Nat. Electron.* **2019**, *2*, 300–306.

[8] Tarancón, A. *Nat. Electron.* **2019**, *2*, 270–271.

[9] Dupont, M. F.; MacFarlane, D. R.; Pringle, J. M. *Chem. Commun.* **2017**, *53*, 6288–6302.

[10] Riffat, S. B.; Ma, X. *Applied Thermal Engineering*. Elsevier **2003**, pp 913–935.

[11] Hu, R.; Cola, B. A.; Haram, N.; Barisci, J. N.; Lee, S.; Stoughton, S.; Wallace, G.; Too, C.; Thomas, M.; Gestos, A.; Dela Cruz, M. E.; Ferraris, J. P.; Zakhidov, A. A.; Baughman, R. H. *Nano Lett.* **2010**, *10*, 838–846.

[12] Zhou, H.; Yamada, T.; Kimizuka, N. *J. Am. Chem. Soc.* **2016**, *138*, 10502–10507.

[13] Straub, A. P.; Yip, N. Y.; Lin, S.; Lee, J.; Elimelech, M. *Nat. Energy* **2016**, *1*, 1–6.

[14] Zhang, Y. S.; Khademhosseini, A. *Science* . **2017**, *356*, eaaf3627.

[15] Chen, G.; Hoffman, A. S. *Nature* **1995**, *373*, 49–52.

[16] Yoshida, R.; Uchida, K.; Kaneko, Y.; Sakai, K.; Kikuchi, A.; Sakurai, Y.; Okano, T. *Nature* **1995**, *374*, 240–242.

[17] Kim, Y. S.; Liu, M.; Ishida, Y.; Ebina, Y.; Osada, M.; Sasaki, T.; Hikima, T.; Takata, M.; Aida, T. *Nat. Mater.* **2015**, *14*, 1002–1007.

[18] Dong, L.; Agarwal, A. K.; Beebe, D. J.; Jiang, H. *Nature* **2006**, *442*, 551–554.

[19] Wang, J.; Gan, D.; Lyon, L. A.; El-Sayed, M. A. *J. Am. Chem. Soc.* **2001**, *123*, 11284–11289.

[20] Wu, S.; Zhang, Q.; Deng, Y.; Li, X.; Luo, Z.; Zheng, B.; Dong, S. *J. Am. Chem. Soc.* **2019**, *142*, 448–455.

[21] Korevaar, P. A.; Kaplan, C. N.; Grinthal, A.; Rust, R. M.; Aizenberg, J. *Nat. Commun.* **2020**, *11*, 1–10.

[22] Kim, J.; Serpe, M. J.; Lyon, L. A. *J. Am. Chem. Soc.* **2004**, *126*, 9512–9513.

[23] Suzuki, A.; Tanaka, T. *Nature* **1990**, *346*, 345–347.

[24] Yan, B.; Boyer, J.-C.; Habault, D.; Branda, N. R.; Zhao, Y. *J. Am. Chem. Soc.* **2012**, *134*, 16558–16561.

[25] Peng, F.; Li, G.; Liu, X.; Wu, S.; Tong, Z. *J. Am. Chem. Soc.* **2008**, *130*, 16166–16167.

[26] Zhang, K.; Feng, X.; Ye, C.; Hempenius, M. A.; Vancso, G. J. *J. Am. Chem.*

Soc. **2017**, *139*, 10029–10035.

[27] Osada, Y.; Okuzaki, H.; Hori, H. *Nature* **1992**, *355*, 242–244.

[28] Miyata, T.; Asami, N.; Uragami, T. *Nature* **1999**, *399*, 766–769.

[29] Miyata, T.; Jige, M.; Nakaminami, T.; Uragami, T. *Proc. Natl. Acad. Sci.* **2006**, *103*, 1190–1193.

[30] Maeda, Y.; Higuchi, T.; Ikeda, I. *Langmuir* **2000**, *16*, 7503–7509.

[31] Shibayama, M.; Tanaka, T. In *Responsive gels: volume transitions I*; Springer, **1993**; pp 1–62.

[32] Oya, T.; Enoki, T.; Grosberg, A. Y.; Masamune, S.; Sakiyama, T.; Takeoka, Y.; Tanaka, K.; Wang, G.; Yilmaz, Y.; Feld, M. S.; Dasari, R.; Tanaka, T. *Science* . **1999**, *286*, 1543–1545.

[33] Serpe, M. J.; Yarmey, K. A.; Nolan, C. M.; Lyon, L. A. *Biomacromolecules* **2005**, *6*, 408–413.

[34] Yoshimatsu, K.; Lesel, B. K.; Yonamine, Y.; Beierle, J. M.; Hoshino, Y.; Shea, K. J. *Angew. Chemie Int. Ed.* **2012**, *51*, 2405–2408.

[35] Geng, H.; Xu, Q.; Wu, M.; Ma, H.; Zhang, P.; Gao, T.; Qu, L.; Ma, T.; Li, C. *Nat. Commun.* **2019**, *10*, 1512.

[36] Matsumoto, K.; Sakikawa, N.; Miyata, T. *Nat. Commun.* **2018**, *9*, 2315.

[37] Hoshino, Y.; Moribe, M.; Gondo, N.; Jibiki, T.; Nakamoto, M.; Guo, B.; Adachi, R.; Miura, Y. *ACS Appl. Polym. Mater.* **2019**, *2*, 505–514.

[38] Hoshino, Y.; Imamura, K.; Yue, M.; Inoue, G.; Miura, Y. *J. Am. Chem. Soc.* **2012**, *134*, 18177–18180.

[39] Lyon, L. A.; Meng, Z.; Singh, N.; Sorrell, C. D.; John, A. S. *Chem. Soc. Rev.* **2009**, *38*, 865–874.

[40] Pelton, R. *Adv. Colloid Interface Sci.* **2000**, *85*, 1–33.

[41] Karg, M.; Pich, A.; Hellweg, T.; Hoare, T.; Lyon, L. A.; Crassous, J. J.; Suzuki, D.; Gumerov, R. A.; Schneider, S.; Potemkin, I. I.; Richtering, W. *Langmuir* **2019**, *35*, 6231–6255.

[42] Hoshino, Y.; Miyoshi, T.; Nakamoto, M.; Miura, Y. *J. Mater. Chem. B* **2017**, *5*, 9204–9210.

[43] Hoshino, Y.; Ohashi, R. C.; Miura, Y. *Adv. Mater.* **2014**, *26*, 3718–3723.

[44] Yue, M.; Hoshino, Y.; Miura, Y. *Chem. Sci.* **2015**, *6*, 6112–6123.

[45] Harned, H. S.; Wright, D. D. *J. Am. Chem. Soc.* **1933**, *55*, 4849–4857.

[46] Al-Masri, D.; Dupont, M.; Yunis, R.; MacFarlane, D. R.; Pringle, J. M. *Electrochim. Acta* **2018**, *269*, 714–723.

[47] Liang, Y.; Yamada, T.; Zhou, H.; Kimizuka, N. *Chem. Sci.* **2019**, *10*, 773–780.

[48] Al Maimani, M.; Black, J. J.; Aldous, L. *Electrochem. commun.* **2016**, *72*, 181–185.

[49] Hasan, S. W.; Said, S. M.; Sabri, M. F. M.; Bakar, A. S. A.; Hashim, N. A.; Hasnan, M. M. I. M.; Pringle, J. M.; MacFarlane, D. R. *Sci. Rep.* **2016**, *6*.

[50] Hoober-Burkhardt, L.; Krishnamoorthy, S.; Yang, B.; Murali, A.; Nirmalchandar, A.; Prakash, G. K. S.; Narayanan, S. R. *J. Electrochem. Soc.* **2017**, *164*, A600--A607.

[51] Kang, T. J.; Fang, S.; Kozlov, M. E.; Haines, C. S.; Li, N.; Kim, Y. H.; Chen,

Y.; Baughman, R. H. *Adv. Funct. Mater.* **2012**, *22*, 477–489.

Chapter 3. Rational Design of Thermocells Driven by the Volume Phase Transition of Hydrogel Nanoparticles

Abstract

Thermocells are thermo-electrochemical conversion systems for harvesting low-temperature thermal energy. Liquid-state thermocells are particularly desirable because of low cost and their high conversion efficiency at the temperature around physiological temperature, and they have, thus, been extensively studied. However, the performance of the thermocells must be improved to utilize them as energy charger and/or battery. In the chapter 2, I reported that a liquid-state thermocell driven by the volume phase transition of hydrogel nanoparticles showed highly efficient thermoelectric conversion with Seebeck coefficient (S_e) of –6.7 mV K^{-1}. Here, I report design rational of the thermocells driven by the phase transition. High S_e of –9.5 mV K^{-1} was achieved at temperature between 36 and 40 °C by optimizing choice and amount of redox chemical species. Figure of merit (ZT) of the thermocell was improved by selecting appropriate electrolyte salt to increase the ionic conductivity and prevent the precipitation of nanoparticles. Furthermore, screening of nanoparticles revealed the high correlation between S_e and the pH shift generated as a result of phase transition of the nanoparticles. After optimization, the maximum ZT of 8.0×10^{-2} at temperature between 20–70 °C was achieved.

3.1. Introduction

The provision of green electricity is a key sustainable development goal (SDG) for this century, but improving the conversion efficiency of green energy resources remains a significant challenge [1]–[5]. In addition, there is high demand for flexible and/or

portable devices that efficiently convert low-grade waste heat into electricity [5]–[7]. Recently, conversion efficiency of thermoelectric conversion elements based on the Seebeck effect have been improved [8],[9]. However, the conversion efficiency of these semiconductor materials for low-temperature thermal energy remains low. In contrast, thermocells, also called thermo-electrochemical cells or thermo-galvanic cells, have huge potential for thermoelectrical energy conversion at the temperature around physiological temperature [10],[11]. In these devices, a difference in the equilibrium potential of redox species is formed in response to temperature differences; this drives redox reactions at the electrodes, thus resulting in thermoelectrical conversion[12],[13].

Recently, a liquid–gas two phase thermocell driven by vaporization of acetone achieved a high S_e of 9.9 mV K^{-1}[14]. A quasi-solid-state thermocell consisting of hydrogel based electrolyte has shown high S_e of 17.1 mV K^{-1}.[15] However, design of liquid-state thermocells (LTC) are still required because of low cost and their potential of high conversion efficiency at the temperature around physiological temperature[16],[17]. Kim et al. reported a LTC showing a high ZT and S_e of 0.16 and 1.4 mV K^{-1}, respectively, by using carbon nanotube as electrodes[18]. Yamada et al. enhanced thermoelectric performance of LTC by using host-guest interactions and salt-induced crystallization[19],[20]. Yu et al. used the dissolution process of thermosensitive crystallization to develop a LTC having a S_e of 3.73 mV K^{-1} [21]. Further, by optimizing the electrolyte and electrode material, S_e has been increased to 4.2 mV K^{-1} [22], which is a considerable thermoelectric conversion efficiency of LTC.

I have reported LTCs using the volume phase transition (VPT) of hydrogel nanoparticles (NPs) and achieved the high S_e values of +6.1 and –6.7 mV K^{-1} [23]. In my systems, as a result of VPT, the proton concentration (pH) in the NP-containing electrolyte changed by a factor of around 100 (~2 units pH shift). The pH difference is converted into cell voltage through proton-coupled redox reactions. Promisingly, S_e values I have obtained are much greater than those of conventional liquid state thermocells[23]. Although thermocells driven by the VPT of hydrogel NPs represent an attractive and promising class of LTCs, a rationale for the design of NP-based thermocells to achieve the high conversion efficiency has not been reported. Thus, in this study, I focused on three primary factors in the construction of the thermocells: the chemical species for the redox reaction (redox species), electrolyte salts, and nature of the hydrogel NPs. Based on my findings, I developed a design rationale for the thermocells driven by the volume phase transition of hydrogel nanoparticles.

Choice of redox species is the most important factor in the design of the thermocell. For pH shift-to-electrical energy conversion, I chose compounds that show proton-coupled electron transfer (PCET) as redox species. At ambient temperature, the equilibrium potential of these redox species is affected by the pH. Therefore, if the pH varies across the thermocell, a large change in the equilibrium potential occurs. In this study, I focused on the quinone-based redox species, including chlorohydroquinone, methylhydroquinone, and anthraquinone-2,7-disulfonic acid combined with VPT of NPs. These redox species undergo reversible redox reactions and have similar structures to the quinone/hydroquinone redox species used in thermocells to date[23],[24].

In addition, to achieve high performance, the thermocell electrolyte must have high ionic conductivity[25]. Different types of electrolyte salts have different effects on ionic conductivity[26], and also affect the colloidal stability of NPs[27],[28]. Therefore,I investigated the optimal electrolyte salt, focusing on KCl, NaCl, and KNO_3.

Last but not least, as a crucial component of the thermocell, the stimulus-responsive hydrogel NPs and their effects on cell performance were investigated. These materials have attracted much attention recently because of their dynamic nature; specifically, they show fast volume changes in response to a small external stimulus, including temperature changes [29]–[32]. A typical stimulus-responsive hydrogel is poly(*N*-isopropylacrylamide) (pNIPAM), which undergoes VPT from the solvent-swollen hydrophilic phase to a shrunken hydrophobic phase at approximately 32 °C [33]–[36]. This change is a result of the entropy-driven dissociation of water from the polymer chains.

In a previous study, I used the changes in the acid dissociation constant (pK_a) of NPs consisting of poly(acrylic acid-*co*-*N*-isopropylacrylamide) (poly(AAc-*co*-NIPAM), also denoted AAc NPs) during the VPT process to produce a shift in pH of approximately 2 pH units from pH 5 to pH 7 between 30 and 40 °C [23]. In the present study, in addition to the AAc-NPs, NPs consisting of chloroacrylic acid (CAc) and methacrylic acid (MAA) instead of AAc (poly(CAc-*co*-NIPAM) and poly(MAA-*co*-NIPAM), respectively) were synthesized and used to trigger the pH shift (Scheme 3-1).

The pK_a values of these two monomers are different from those of AAc, resulting in changes in the ranges of pH shift [35],[36].

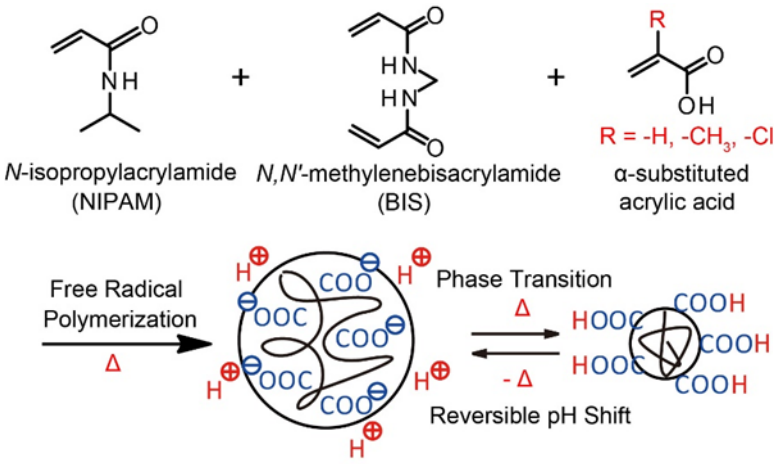

Scheme 3-1. Schematic of the copolymerization of temperature-responsive hydrogel NPs consisting of substituted acrylic acid, *N*-isopropylacrylamide, and *N*,*N*'-methylenebisacryalmide. Rapid, reversible VPT results in reversible changes in the pK_a of the hydrogel nanoparticles.

3.2. Materials and experiments

3.2.1. Materials

The following chemicals and materials were obtained from commercial sources and used as received unless otherwise stated. *N*,*N*-Methylenebisacrylamide (BIS), cetyltrimethylammonium bromide (CTAB), 2-chloroacrylic acid (CAc, purity 96.0%), *N*-[3-(dimethylamino)propyl]methacrylamide (DMAPM), and Sodium dithionite

(DITH, purity > 85.0%) were obtained from Tokyo Chemical Industry Co., Ltd. HCl, hexane, sodium chloride, acrylic acid (AAc, purity > 99.0%), methacrylic acid (MAA, purity > 99.0%), sodium dodecyl sulfate (SDS), azobisisobutyronitrile (AIBN), and 4,4'-azobis(4-cyanovaleric acid) (V-501) were obtained from Watanabe Pure Chemical Industry Co., Ltd. NaOH, KCl, NaCl, and KNO_3 were obtained from Kanto Chemical Co., Inc., and *N*-isopropylacrylamide (NIPAM, purity > 98.0%), anthraquinone-2,7-disulfonic acid (2,7-AQDS, purity > 95.0%), riboflavin (RF, purity > 97.0%), methylene blue (MB, purity > 98.5%), KSCN (purity 98.0%), hydroquinone (HQ, purity > 99.0%), methylhydroquinone (MHQ, purity 99.0%), chlorohydroquinone (CHQ, purity 90.0%), and 2,5-dichlorohydroquinone (DCHQ, purity 98.0%) were obtained from Wako Pure Chemical Industries, Co., Ltd. and recrystallized from hexane. The dialysis tube (MWCO 12,000–14,000 Da, Spectrum Laboratories, Inc.) was washed with water before use. Cation exchange beads (Muromac C1002-H, Muromachi Chemicals, Inc.) and anion exchange beads (Muromachi Technos Co., Ltd., A2004-OH) were pretreated with aqueous HCl (1 M) and then washed with excess water. The water used in this study was purified using a Direct-Q Ultrapure Water System (Merck, Ltd.).

3.2.2. Preparation of NPs

Poly(AAc-*co*-NIPAM) NPs (AAc NPs) were synthesized following our previously reported method [23],[34]–[36]. Using a similar method, I synthesized poly(CAc-*co*-NIPAM) and poly(MAA-*co*-NIPAM). Briefly, NIPAM (93 mol%, 3.28

g), BIS (2 mol%, 96 mg), SDS (180 mg), and CAc (5 mol%, 419.6 mg) or MAA (5 mol%, 340.4 mg) were dissolved in 100 mL of water, resulting in a total monomer concentration of 312 mM. For poly(CAc-*co*-NIPAM), I used two pH values during synthesis. One solution was adjusted with aqueous NaOH to pH 2.9 (monitored using a pH meter (F-52T, Sankei Chemical Co. Ltd.)), whereas the other was adjusted to pH 2.3. For poly(MAA-*co*-NIPAM), the pH of the solution was adjusted using aqueous NaOH to be 2.9. The reaction mixture was then degassed by nitrogen flushing for 30 min. Following the addition of the V-501 initiator (19.3 mg in 1.96 mL of dimethylsulfoxide (DMSO)), polymerization was carried out at 70 °C for 3 h under a nitrogen atmosphere. Subsequently, the polymerized solution was purified by dialysis against an excess amount of water (at least three times a day) for 2 days. Traces of counter anions were removed using strong cation exchange beads (Muromac C1002-H, Muromachi Chemicals, Inc.). The beads were filtered out after 1 h of ion-exchange.

The yields of poly(CAc-*co*-NIPAM) NPs (CAc NPs) and poly(MAA-*co*-NIPAM) NPs (MAA NPs) were determined by measuring the weight of NPs obtained by the lyophilization of a part of the dialyzed solution. The concentrations of the CAc NPs and MAA NPs treated by the lyophilization method were determined by measuring the moisture absorption and mass after reaching humidity balance in air.

3.2.3. ^{1}H NMR measurement

For ^{1}H-NMR measurements, lyophilized NPs were dissolved in CD_3OD (50 mg mL^{-1}) and analyzed on a JEOL JNM-ECP400 instrument at 25 °C. The amount of trace surfactant remaining in the NPs was determined by NMR.

3.2.4. Quantification of VPT temperature and hydrodynamic diameter of NPs

The VPT behavior of the samples was confirmed by dynamic light scattering (DLS) measurements (Zetasizer Nano, Malvern Instruments Limited) using ion-exchanged solutions. The solutions were equilibrated at each temperature for 2 min before measurement. VPT temperature was determined as the temperature where the plateau of relative scattering intensity started.

3.2.5. Quantification of carboxylic acid concentration in NPs

The concentrations of the carboxylic acid groups in the CAc NPs synthesized at pH 2.3 and 2.9 and that of the MAA NPs was estimated by acid–base titration using aqueous NaOH at 30 and 70 °C with stirring at 500 rpm. A pH meter (S50 SevenMulti, Mettler Toledo Co. Ltd.) equipped with pH probes (InLab Routine Pro, Mettler Toledo Co. Ltd.) was calibrated with standard buffers (pH = 4.01, 7.00, and 9.21) prior to use. Temperature of NP solution was controlled by water bath. According to the mass concentration of NPs, the concentration of carboxyl groups in the original solution can

be calculated. The pH values of the solutions were adjusted to be equal to the apparent pK_a of the acids in the NPs by adding NaOH (0.5 eq).

3.2.6. Measurement of pK_a shift curve in heating process

Apparent pK_a of acrylic acids in CAc NPs and MAA NPs is equal to the pH value at the half neutralization point. pK_a shift curve was measured with a pH probe by the following method: half neutralized NP solution was prepared by adding 0.5 equivalents of NaOH. Then pH value and temperature of NP solution every 3 seconds during temperature swing process was recorded by the pH probe with stirring 500 rpm. Temperature change was controlled by a synthesis plant (Eyela PPW-200, Tokyo Rikakikai Co., Ltd.).

3.2.7. Preparation of redox species for the thermocell electrolyte

Redox species were pretreated for electrolyte preparation. Specifically, before preparing the thermocells, 0.5 eq of DITH was added to solutions of 2,7-AQDS, RF, or MB to adjust the ratio of the oxidized state to the reduced state to 1:1. For HQ, MHQ, CHQ, and DCHQ, which are in their reduced states, aqueous solutions were bubbled with air for sufficient time (at least 6 hours) to ensure complete oxidation. Then, an equal amount of the original solution was mixed with the oxidized solution to adjust the ratio of the oxidized state to the reduced state to 1:1 in the electrolyte solution.

3.2.8. Measurement of thermoelectric voltage and current

The thermoelectric voltage and current were measured following my previously reported procedure[23] and the following setup (Figure 3-1). The electrolyte solutions (10 mL) were placed into water-jacketed glass cells (Φ 25.6 mm × 50 mm), and two stirrers (Φ 5 mm × 20 mm) were added to each half cell. Each cell was covered with a three-hole Teflon cap, and a platinum working electrode was immersed in the electrolyte solution. A 25-cm silicon tube salt bridge containing agar gel with 3 M potassium chloride solution was inserted through the three-hole Teflon cap to connect the two cells. Finally, a thermocouple was inserted into the electrolyte solution of each cell. The temperature of each cell was controlled separately using an external thermostatic device to circulate water into the jacket of each cell. The terminals of the Keithley 2401 source meter were connected to the electrodes of each cell. Direct current DC voltage measurement mode (mV) was used to display the voltage. As described above, various redox species and NPs were prepared, and combinations of these were dissolved in Milli-Q water for each experiment. The pH of each cell was adjusted by adding 0.5 eq of NaOH. KCl (30 mM) was added to improve the ionic conductivity. After confirming the voltage of both cells had stabilized at 20 °C, the temperature of the jacket water of one cell was gradually increased to 70 °C. The difference in temperature and voltage between the hot and cold cell sides was then plotted, and S_e was estimated from the slope of the plot. The changes in the pH and ionic conductivity

of the electrolyte during experiments were measured simultaneously using a pH meter and an ion conductivity meter (Sankei Chemical Co. Ltd), respectively.

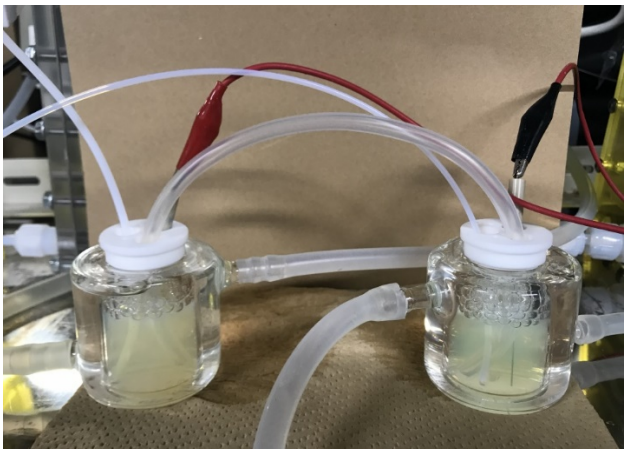

Figure 3-1. Photograph of a bridged thermocell design for open circuit voltage measurement.

The experimental apparatus for the current measurements consisted of the following components: A homemade H-shaped glass tube with an inner diameter of 20 mm was used as the thermocell (Figure 3-2). The cell contained 35 mL of electrolyte solution. Each side of the container was immersed in a cooled or heated solution to control the temperature of each side separately. Before use, platinum wire electrodes (1 mm in diameter and 40 mm in length) were washed by soaking in concentrated sulfuric acid followed by rinsing in ultrapure water. Then, two platinum wires were immersed in the electrolyte solution, and the current between the wires was measured using a Keithley 2401 source meter. The temperatures at each side of the cell were monitored

using two thermometers (TM-201). The temperature of the cold side of the container was maintained at approximately 20 °C, and the solution was magnetically stirred during the measurements. The electrolyte composition was the same as that described above and used for voltage measurements. While one end of the H-shaped glass tube was heated from 20 to 70 °C, the source meter was used to apply a reverse voltage across the electrodes and record the current to obtain a current–voltage (*I–V*) curve that represents the power performance of the thermocell.

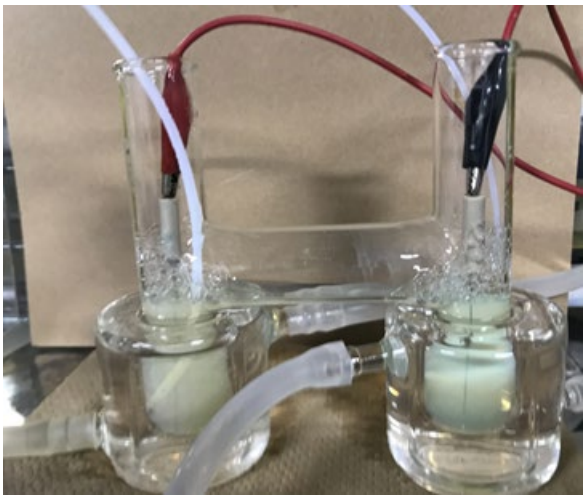

Figure 3-2. Photograph of H-shape thermocell for current measurement.

3.2.9. Ionic conductivity measurement and performance calculation

The ionic conductivity of the electrolyte solutions was measured by an electric conductivity meter (SevenMulti Dual Digital Meter with Conductivity and pH Modules, Mettler Toledo) with a Mettler-Toledo Conductivity TDS/SAL/Resistivity Module.

The performance of the thermoelectric devices was evaluated using the dimensionless *ZT* value given in Eq. 3-1, which is determined from S_e, as well as the ionic conductivity (σ), average absolute temperature (*T*), and thermal conductivity (*k*). The thermal conductivity of a low-concentration NP solution can be approximated as that of water.

$$ZT = \frac{\sigma S_e^2}{\kappa} T \qquad \text{Eq. 3-1}$$

Thus, the apparent *ZT* values were estimated from the measured σ and S_e values for each electrolyte.

3.3. Results and Discussion

3.3.1. Preparation of NPs

CAc NPs and MAA NPs that undergoes the VPT in aqueous media at a temperature around 40 °C was prepared as reported.[35] By measuring the weight of NPs obtained by lyophilization of a part of the dialyzed solution, the yield of CAc NPs was obtained as 82.4% and 80.6% for NPs synthesized at pH 2.3 and pH 2.9, respectively. For MAA NPs, the yield was 79.7%. The concentrations of the CAc NPs (42.21 mg mL^{-1} at pH 2.3 and 31.77 mg mL^{-1} at pH 2.9) and MAA NPs (30.41 mg mL^{-1}) treated by the lyophilization method were also measured. The ^1H NMR results of CAc NPs synthesized at pH 2.9 (Figure 3-3a) and MAA NPs (Figure 3-3b) showed that surfactant concentrations remaining in NPs were low.

(a)

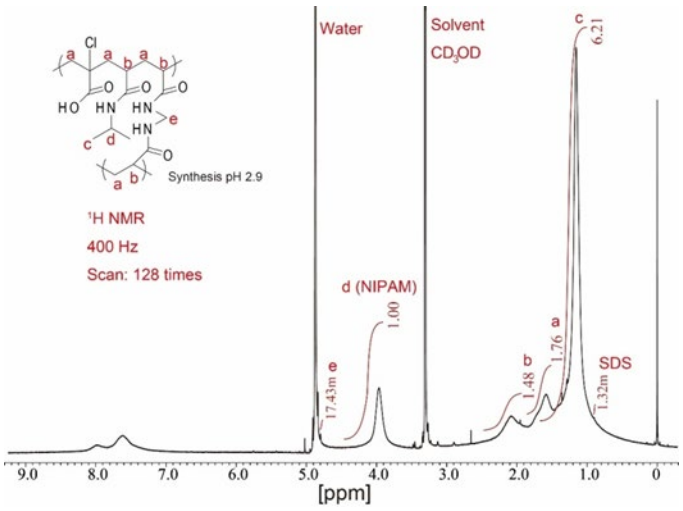

(b)

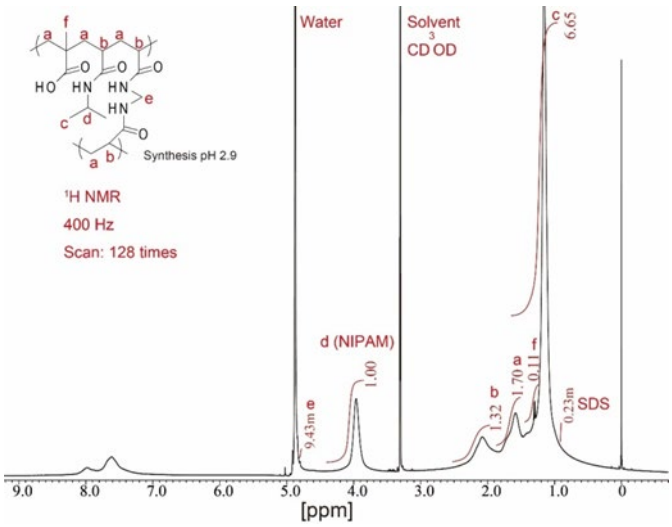

Figure 3-3. ^{1}H NMR results of (a) CAc NPs and (b) MAA NPs.

3.3.2. VPT behavior of NPs

Figure 3-4 shows a plot of the hydrodynamic diameter of NPs obtained by DLS as a function of temperature. The average diameters of the polymer chains decreased during VPT, which corresponds to the dehydration of the polymer chains above 30 °C.

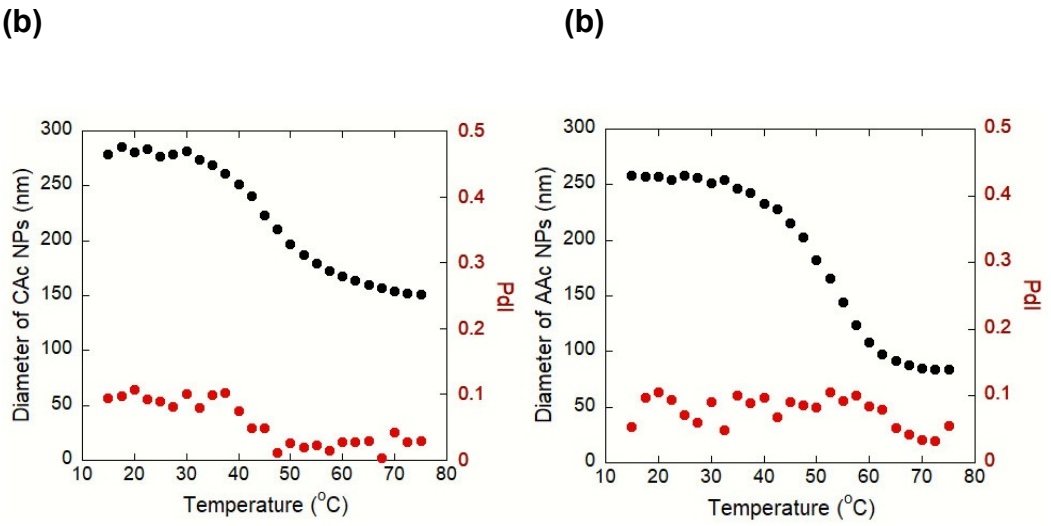

Figure 3-4. Change of mean-diameter (black dots) and poly dispersity index (PdI, red dots) of (a) CAc NPs (1.0 mg/mL) (b) MAA NPs (1.0 mg/mL) estimated from DLS measurements with the change in temperature.

Through results showed that the mean-diameter of NPs changes greatly with the change of temperature, which is attributed to the VPT process. In the swollen phase, pNIPAM is hydrated, and thus, microenvironment around the acids in the NPs is hydrophilic. However, at temperatures above the VPT temperature, NPs shrinks as a

result of entropically driven dissociation of water molecules from pNIPAM, and the environment around the acids becomes hydrophobic[33]–[35].

3.3.3. Acid–base titration results of NPs

The concentrations of the carboxylic acid groups in the CAc NPs synthesized at pH 2.3 and 2.9 and that of the MAA NPs were estimated to be 412.4, 548.0, and 337.5 mmol g^{-1} by acid–base titration with aqueous NaOH at 30 and 70 °C (Figure 3-5).

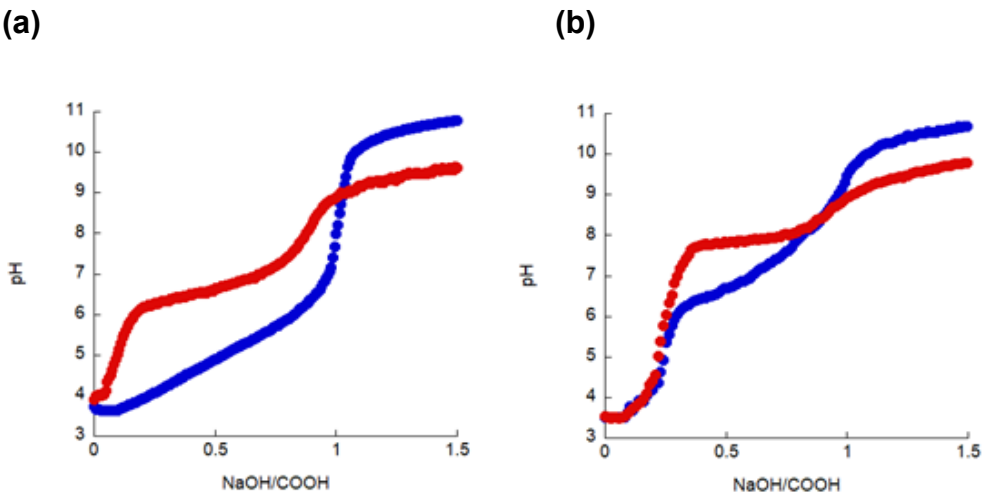

Figure 3-5. Titration curves of (a) CAc NPs (4.0 mg/mL, synthesized in pH 2.9) and (b) MAA NPs (4.0 mg/mL) at 30 (blue) and 75 °C (red). The horizontal axis is the amount of added NaOH to the concentration of carboxy groups in NPs.

Amount and pK_a of acids in NPs were determined by acid base titration. When pH of the solution was adjusted by strong base (NaOH) to be equal to the pK_a of CAc/MAA in the NPs, the environmental change induced significant pH change of the NPs solution by elevating the temperature from 20 to 70 °C (Figure 3-6, red line and black line) associating with the pK_a shift of acids in the particles.[35] The CAc NPs and MAA NPs showed different pH shift ranges comparing to AAc NPs (Figure 3-6, blue line).[35],[37]

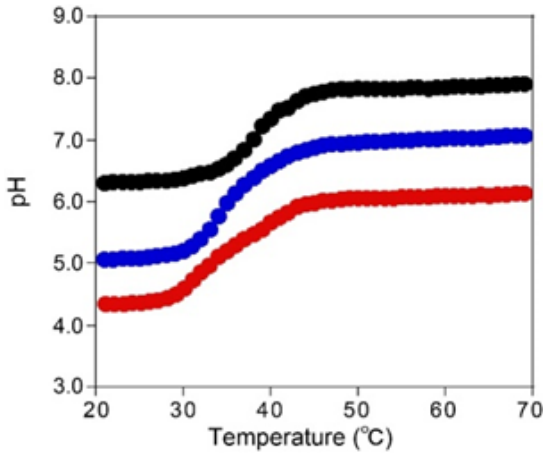

Figure 3-6. Temperature dependent pH change of poly(CAc-co-NIPAM) NPs ([CAc] = 2 mM, [NaOH] = 1 mM) (red) and poly(MAA-co-NIPAM) NPs ([MAA] = 2 mM, [NaOH] = 1 mM)) (black) solutions. As a reference comparison, AAc NPs ([AAc] = 2 mM, [NaOH] = 1 mM) (blue), reported in Chapter 2, shows a different pH shift range as a function of temperature.

3.3.4. Effect of types and concentrations of redox species on thermocell performance

Thermocells (containing 5.6 mM redox species) with AAc NPs (5.9 mg mL^{-1}, [AAc] = 2 mM, [NaOH] = 1 mM) reported in Chapter 2 were constructed using a set of water-jacketed cells and platinum electrodes connected with a salt bridge. Then, 2,7-AQDS, RF, MB, HQ, MHQ, CHQ, and DCHQ were screened as potential redox species. These redox species undergo reversible PCET reactions (Table 3-1) and do not decompose on heating at 70 °C [38]–[40]. The redox species comprising equal amounts of oxidized and reduced states were mixed with the NP solution. A thermocell without redox species was also constructed as a control cell. The compositions of the electrolytes in the two water-jacketed cells were the same. After the system had stabilized, the temperature of one side of the cell was maintained at 20 °C, and that of the other side was gradually increased from 20 to 70 °C by circulating hot or cold water through the jacket. The open-circuit voltage and ionic conductivity of the thermocell were recorded every 2 °C during heating, and S_e and ZT, key thermocell performance metrics, were calculated from the changes in voltage and conductivity (Figure 3-7).

Table 3-1. PCET reaction of redox species and acid dissociation constant[41]–[48].

Name	Chemical Structure	pK_{a1}	PCET reaction
2,7-AQDS	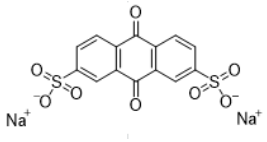	**7.6**	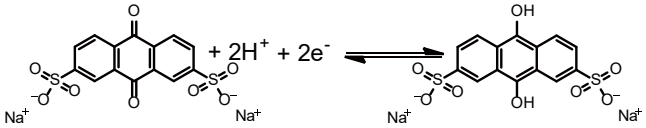
HQ	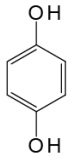	**9.8**	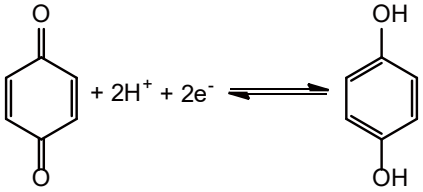
MHQ	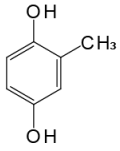	**9.0**	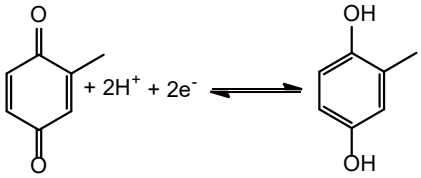
CHQ	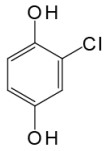	**8.2**	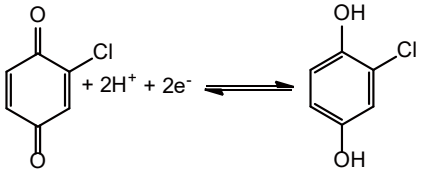
DCHQ	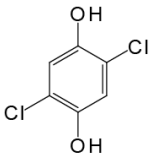	**7.6**	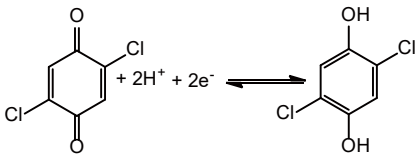
DCNHQ	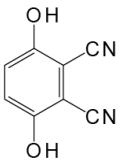	**5.5**	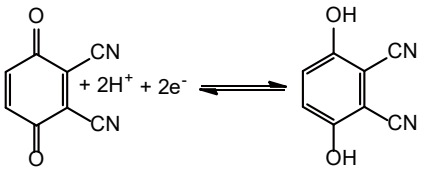
RF	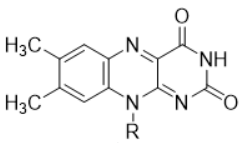	**10.2**	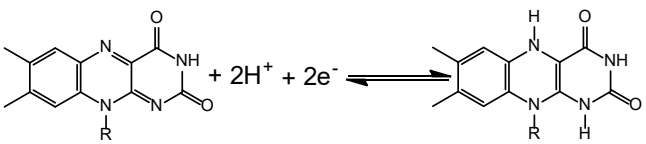
MB	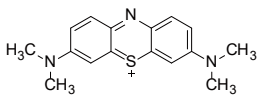	**3.8**	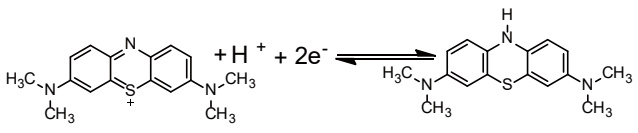

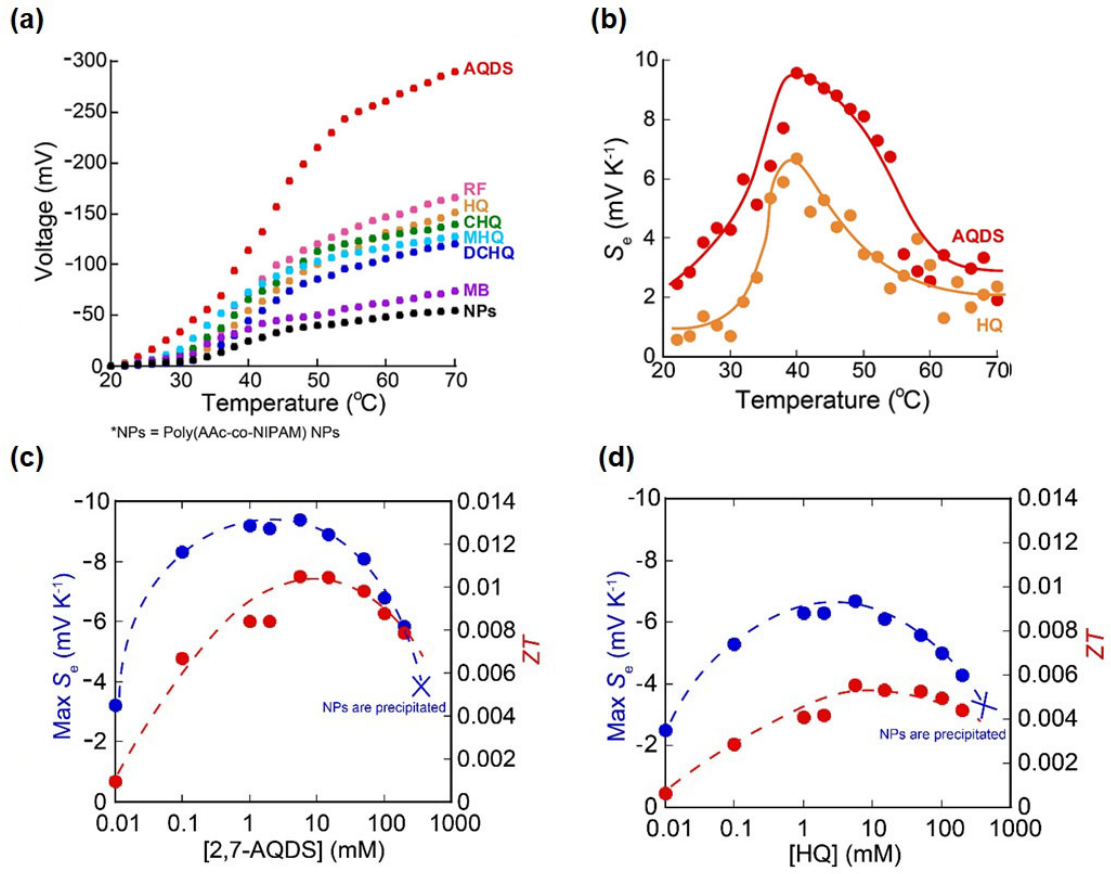

Figure 3-7. (a) Open-circuit voltage of AAc NPs ([AAc] = 2 mM, [NaOH] = 1 mM) thermocells constructed without redox species (black) and with seven different redox species. Gradients correspond to S_e. (b) S_e of thermocells containing 2,7-AQDS (red) and HQ (orange) with AAc NPs with respect to temperature. (c) Maximum values of S_e (blue line) and ZT (red line) at different 2,7-AQDS concentrations. (d) Maximum values of S_e (blue line) and ZT (red line) at different HQ concentrations.

The thermocell that did not contain redox species showed a small voltage (< 50 mV) between the two half-cells (Figure 3-7a), but the voltage abruptly increased at the phase-transition temperature. This is because the solution pH changed in response to

the VPT of the nanoparticles (Figure 3-6)[23]. However, the addition of redox species resulted in larger voltage changes at the phase-transition temperature due to the pH change and redox reaction (Scheme 3-2). The open-circuit voltage of the thermocell also differed depending on the redox species. The maximum open-circuit voltage achieved at a temperature difference of 50 °C was −288 mV using 2,7-AQDS, for which the S_e was −5.8 mV K^{-1}, which is greater than previously reported values (S_e was −3.0 mV K^{-1})[23]. The highest S_e of −9.5 mV K^{-1} was observed at the temperatures between 36 and 40 °C (Figure 3-7b). The origin of this high performance is the sharp change in pH caused by the VPT of the NPs, which results in proton and electron transfer and reduction of the quinone state of 2,7-AQDS to the hydroquinone state [49],[50]. 2,7-AQDS resulted in the highest S_e value of LTCs reported to date (the previously reported S_e values are listed in Table 1-4 in Chapter 1). The potential differences between the redox species in the two half-cells at different pH values were calculated using the Nernst equation[51]. The appropriate combinations of standard potential and pK_a (listed in Table 3-1) allow the stable existence of a redox species in NPs electrolyte solution. For the PCET reaction with the proton number m and electron number n, the equilibrium potential of redox species shifts for 59 m/n mV pH^{-1}. Therefore, if the pH of one side of the cell is different from the other side, a large shift of equilibrium potential can be observed. I assessed several redox species including those that undergo two-electron, two-proton redox processes and one-electron, one-proton processes. Specifically, MB can only react with one proton, so the voltage on pH change is half that of redox species that can react with two protons. Of the two-proton, two-electron redox species, 2,7-

AQDS produced the highest voltage. This might be due to formation of 2,7-AQDS dimers in acidic and neutral solutions[52]–[55]. The changes in reaction equilibrium triggered by 2,7-AQDS dimer formation and intermolecular interactions with NPs[56] are the most likely reasons for the high voltage observed, see appendix.

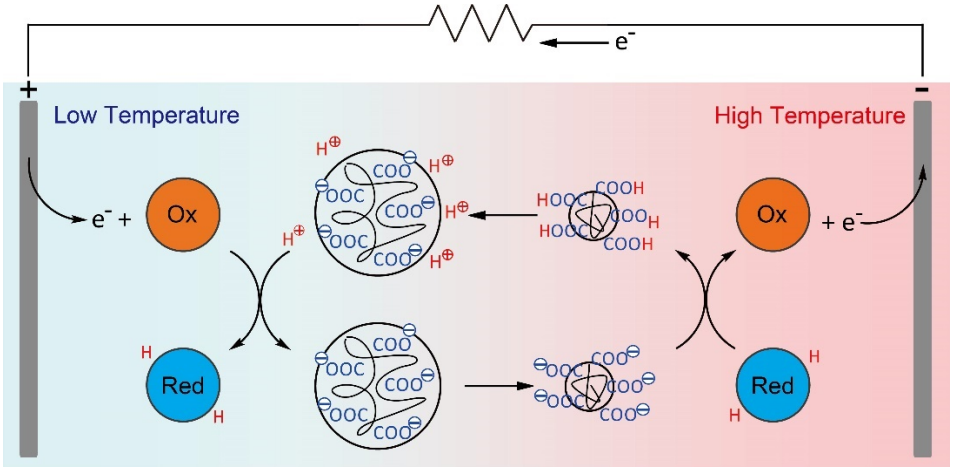

Scheme 3-2. The proposed mechanism of thermocell driven by the volume phase transition of hydrogel nanoparticles. NPs are in the solvent-swollen hydrophilic phase at low temperature and provide protons to promote the reduction reaction of redox species on the cold electrode. On the hot electrode, the shrunken hydrophobic phase NPs absorb protons and promote the oxidation reaction of redox species.

The effect of the concentration of the redox species on thermocell performance was also investigated. Figures 3-7c and 3-7d show the influence of the concentrations of 2,7-AQDS and HQ, respectively, on the maximum values of S_e and ZT. The

maximum value of Se increased when concentration of the redox species was increased withing a certain range (up to 5.6 mM). However, as the redox-species-to-NP concentration ratio increased, there was a decrease in the maximum value of S_e, probably because the NPs became less capable of controlling the pH change due to relative reduction of ionization effect. If the concentration of redox species is very low, the thermocell performance will also be greatly reduced because the ion-entropy transfer and electromotive force will be reduced [57]. Further, if the concentration of redox species is very high, the ionic conductivity of the solution will also be high, thus enhancing thermocell performance. However, in my experiments, when the concentration of redox species exceeded 100 mM, the NPs salted-out at the phase-transition temperature (36 °C), generating white precipitates and resulting in significant degradation of thermocell performance. Moreover, because the NPs were precipitated, S_e could not be measured at these concentrations. Therefore, to obtain the maximum *ZT*, the optimal concentration of redox species must be used: approximately 5.6 mM.

3.3.5. Effect of types and concentrations of electrolyte salt on thermocell performance

To investigate the effect of the electrolyte salt on the performance of thermocells I screened three common salts: KCl, NaCl, and KNO_3. Thermocells containing 5.6 mM 2,7-AQDS or HQ with AAc NPs (5.9 mg mL^{-1}, [AAc] = 2 mM, [NaOH] = 1 mM) were constructed. The addition of these salts to the thermocells increased the ionic

concentration, and the maximum values of *ZT* increased compared to those at the same temperature without the salts (Figure 3-8).

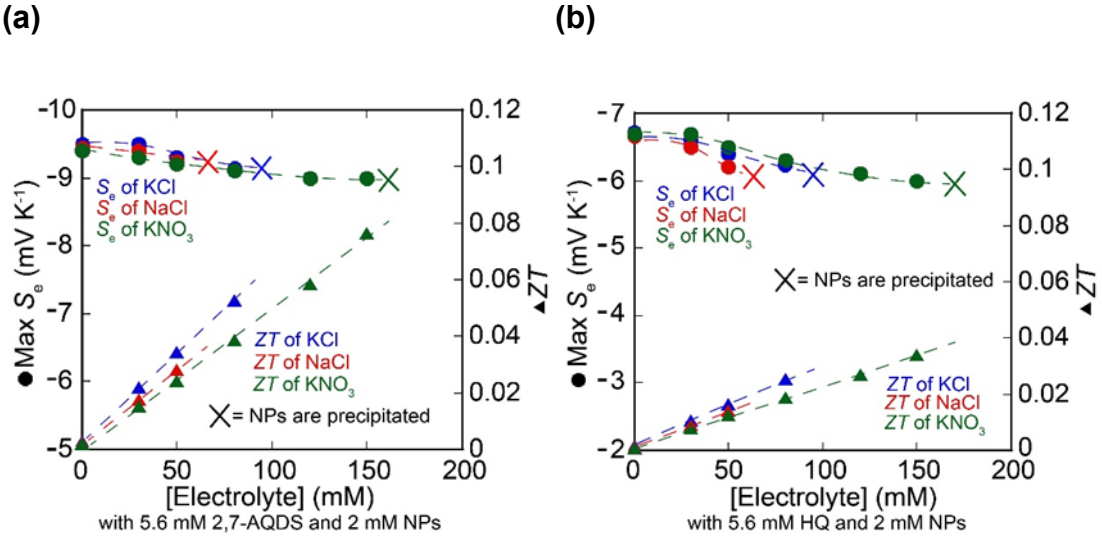

Figure 3-8. Effect of electrolyte concentration on the maximum value of S_e (circles and dashed lines) and *ZT* (triangles and solid lines) of thermocells containing AAc ([AAc] = 2 mM, [NaOH] = 1 mM) and (a) 2,7-AQDS (5.6 mM) or (b) HQ (5.6 mM). When the KCl and NaCl concentrations in the electrolyte reached 100 mM, NPs were precipitated; thus, S_e and *ZT* could not be calculated.

As shown in Figure 3-8, adding KCl, NaCl, or KNO_3 significantly improved the *ZT*. However, when the KCl or NaCl concentration exceeded 100 mM, salting-out of NPs occurred at the temperature above phase transition temperature, yielding a white precipitate that interfered with measurements (Figure 3-9).

Figure 3-9. Photo of NPs being precipitated (left cell). It is caused by the relative high electrolyte concentration.

On the other hand, concentration of KNO_3 can be increased up to 150 mM without yielding precipitations. Previous hydrogel research[27],[28] has shown that replacing KCl or NaCl with the electrolyte salt containing weakly hydrated and highly polarizable anions, e.g., KNO_3, can promote NPs stability in solution and resolve the salting-out issue. The cells with 150 mM KNO_3 showed highest *ZT* because highest ion concentration could be achieved without precipitation NPs, although, aqueous KNO_3 solution shows a smaller ion conductivity than that of NaCl or KCl at the same concentrations (Figure 3-10).

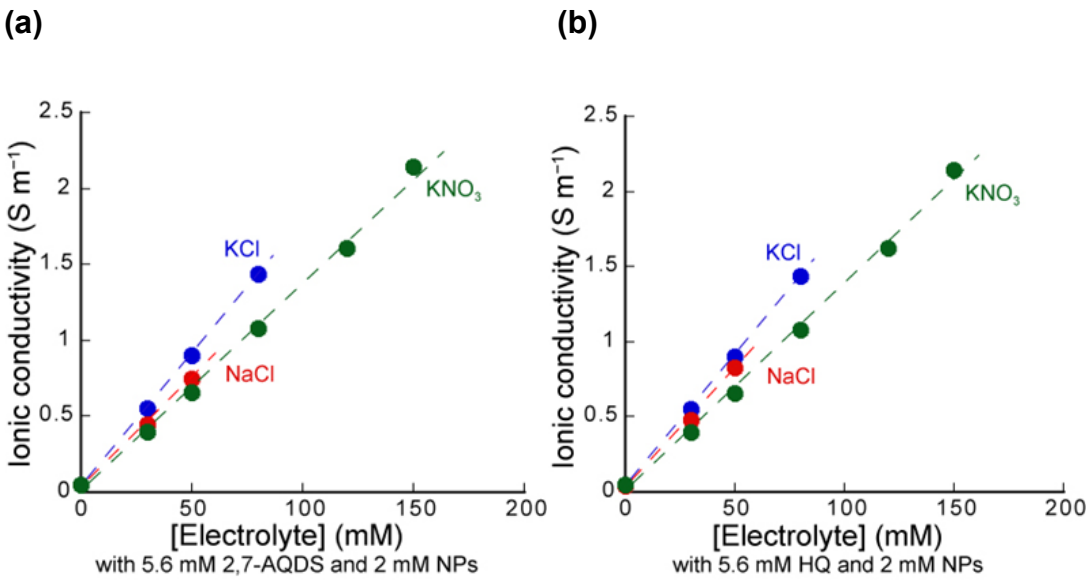

Figure 3-10. Effect of electrolyte concentration on the ionic conductivity in thermocells containing AAc NPs ([AAc] = 2 mM, [NaOH] = 1 mM) and (a) 2,7-AQDS (5.6 mM) or (b) HQ (5.6 mM)

According to the Hofmeister series, the ability of salts to precipitate certain proteins from an aqueous solution follows a recurring trend.[27] Hofmeister series can also be explained for the precipitation of NPs based on direct interactions of the anions with the macromolecule and its immediately adjacent hydration shell. Some anions, such as nitrate ions and thiocyanate ions, can make the precipitation of NPs in aqueous solutions more difficult. Other anions can polarize an adjacent water molecule that is in turn involved in hydrogen bonding with the amide in NPs which leads to the precipitation of the polymer. As a control experiment, I used another electrolyte salt that is more difficult to precipitate NPs in the Hofmeister series, KSCN. The experimental results showed that NPs in thermocells containing KSCN were more

difficult to precipitate than KNO_3. However, the unit concentration of KSCN produced a small increase in ion conductivity (Figure 3-11a), which cannot effectively increase the *ZT* value of the thermocell (Figure 3-11b).

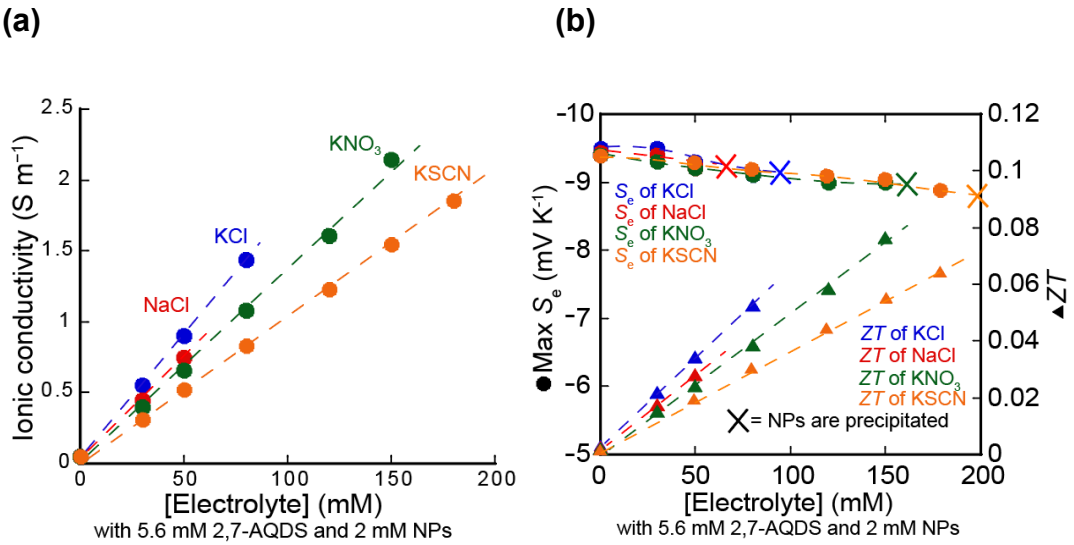

Figure 3-11. (a) Effect of electrolyte concentration on (a) the ionic conductivity and (b) the maximum value of S_e and *ZT* of thermocells containing AAc NPs ([AAc] = 2 mM, [NaOH] = 1 mM), 2,7-AQDS (5.6 mM) and four types of electrolyte salts.

3.3.6. Effect of the type and concentration of NPs on the thermocell performance

In the above experiments and my previous report[23], I used NPs containing AAc to create a pH gradient on temperature change. To verify the effect of the type of NPs on the thermocell performance, NPs containing CAc and MAA were synthesized. The properties of these two monomers are similar to those of AAc but their pK_a values

differ[35]. By controlling the pH and other conditions during synthesis, the formed NPs have different magnitudes of pH change around the VPT temperature (Figure 3-6).

For these tests, thermocells containing 5.6 mM of 2,7-AQDS or HQ were used. For each redox species, I used the same composition ([acid] = 2 mM, [NaOH] = 1 mM) of AAc NPs, CAc NPs, orMAA NPs. The same method was used to measure the open-circuit voltages of the thermocells to determine the effect of the NPs on the maximum voltage generated at a temperature difference of 50 °C of these two redox species (Figure 3-12).

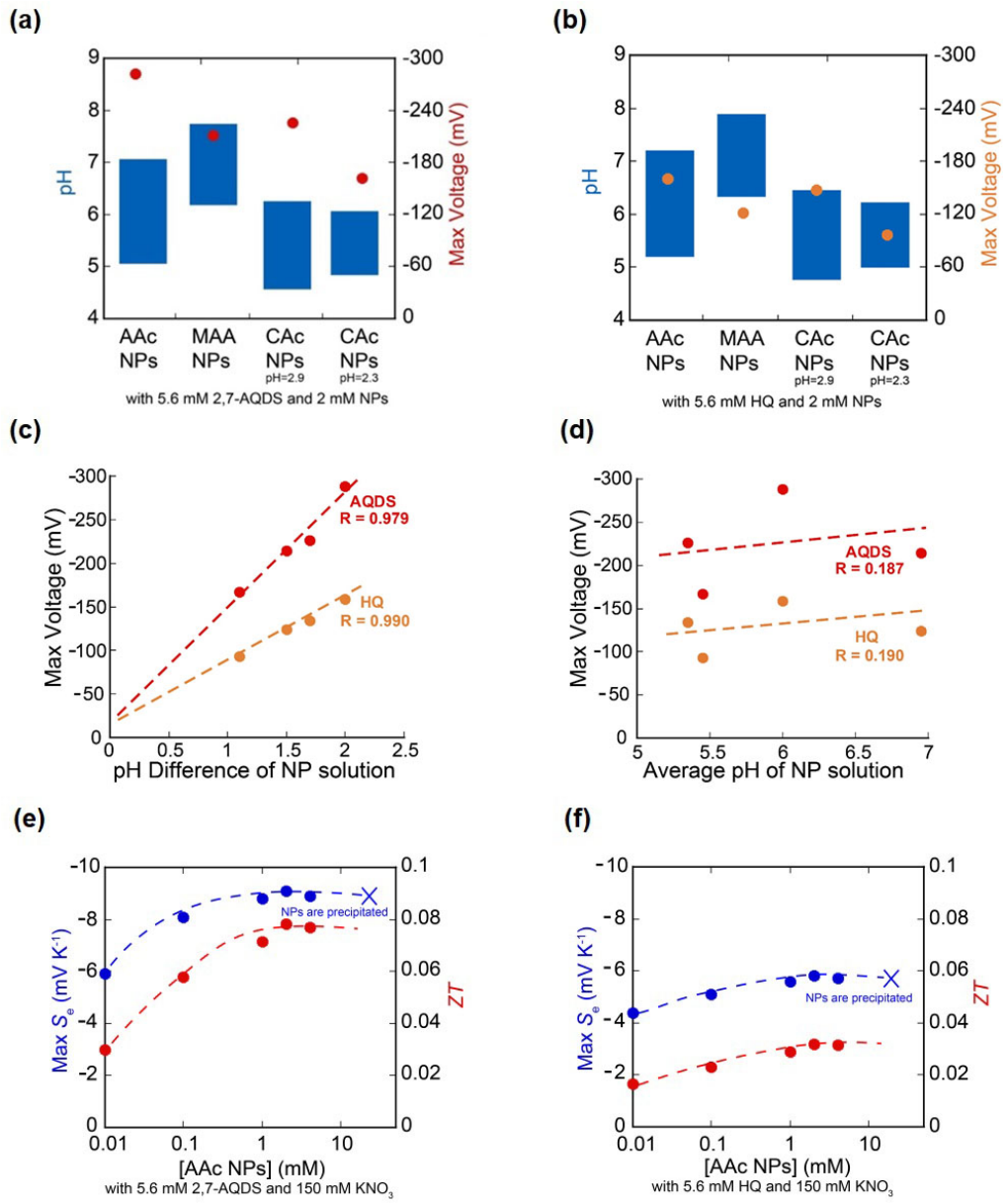

Figure 3-12. (a) pH changes (left-hand *y*-axis) and maximum open-circuit voltages (right-hand *y*-axis, red dots) of thermocells constructed with AAc, MAA, and CAc NPs (synthesized at pH = 2.3 and 2.9) (for all thermocells, [acid] = 2 mM, [NaOH] = 1 mM) and 2,7-AQDS between 20 and 70 °C. (b) As for (a) but with HQ. (c) Correlation between the pH difference and voltage. (d) Correlation between the average pH and voltage. Maximum values of S_e (blue line) and *ZT* (red line) with respect to AAc NP concentration with (e) 2,7-AQDS and (f) HQ.

Figure 3-12 shows the differing open-circuit voltages of thermocells containing 2,7-AQDS with different NPs at the same concentration. An important factor affecting the open-circuit voltage is the difference in the solution pH caused by the VPT of the NPs. The largest change in pH between 20 and 70 °C was observed for the AAc NPs (approximately pH 5.0 to 7.0, respectively), and this also yielded the maximum open-circuit voltage. In contrast, the CAc NPs synthesized at pH = 2.3 showed the smallest pH change at the same temperatures, and the open-circuit voltage was also the lowest of the tested systems. For the MAA and CAc NPs synthesized at pH = 2.9, the magnitudes of the pH changes are similar to AAc NPs (around 1.5 pH units), but the pH values over which these changes occur are different (between pH 6.2 and 7.7 and 4.6 and 6.2, respectively). This difference had only a slight influence on the maximum open-circuit voltage (red dots in Figure 3-12a). Similar experimental results were observed for the thermocells containing HQ (Figure 3-12b). By examining the correlation between the magnitude of the pH change and the average pH (the midpoint of pH change) and the maximum open-circuit voltage, I found that the key factor is the former (Figures 3-12c and 3-12d). Among the pH changes measured for the four NPs, that of the AAc NPs was the largest. This is because the NPs with carboxylic acids which show large and reversible pK_a shifts in response to temperature change were prepared via the proton imprinting polymerization process.[34] Studies have shown that reducing the feed ratio of AAc in AAc NPs can further broaden the width of the pKa shift up to 2.2.[34] However, this will make it more difficult to control the pH change of the electrolyte solution with the same concentration of NPs. In this study, to balance

these effects, a 5 mol% AAc feed ratio was adopted to synthesize AAc NPs. Substitution of the α-position of the acidic monomers (MAA and CAc) prevents complete denaturation of the imprinted proton binding sites and/or prevents formation of well re-foldable proton binding sites, narrowing the width of the pK_a shift.[35] Therefore, of those studied, the AAc NPs, which showed larged pH changes, are the optimal NPs.

The effect of the concentration of AAc NPs on the thermoelectric conversion capability of the thermocells was also investigated. Figures 3-12e and 3-12f show the effects of the NP concentration on the maximum values of S_e and ZT. Higher concentrations of NPs resulted in greater changes in the solution pH, thereby improving performance of the cells. However, when concentrations of NPs were above 2 mM, significant improvement was not observed. In particular, at a concentration higher than 20 mM, precipitation of NPs due to salting out was also observed. Therefore, balancing these factors, to obtain the maximum S_e and ZT values, the optimal NP concentration was determined to be approximately 2 mM.

3.3.7. Performance of optimal thermocell

After screening the redox species, electrolytes, and NPs, I constructed a thermocell with the optimal composition. The screening of the redox species showed that 2,7-AQDS yields the highest S_e, and, at a moderate concentration (5.6 mM), it maintains both high ionic conductivity and NP stability. Secondly, electrolyte screening revealed

that, although KCl and NaCl increase the ionic conductivity to a greater extent at the same concentration, KNO_3 is a better choice because the former salts result in NP precipitation at high concentrations. Thus, by using KNO_3, a higher electrolyte concentration can be used, resulting in higher conductivity. Finally, the optimum NP was chosen based on the maximum voltage. Because the AAc NPs resulted in the largest pH difference at the VPT, and, thus, highest voltage of the tested NPs, they were chosen as the optimum NP species. As discussed earlier, at temperatures above the phase-transition temperature (36 °C), the VPT occurs, and the NPs become hydrophobic and shrink, which reduces the proton concentration in the solution and abstracts protons from the hydroquinone form of 2,7-AQDS (2,7-AH_2DS) driving oxidation reaction. In contrast, when the temperature decreases below 36 °C, the NPs become hydrophilic, volume expansion occurs, and the solution pH increases. As a result, 2,7-AQDS is protonated by the NPs and reduced to the hydroquinone state.

The output current of the optimized thermocell comprising an H-shape glass tube containing 5.6 mM 2,7-AQDS, AAc NPs (5.9 mg mL^{-1}, [AAc] = 2 mM, [NaOH] = 1 mM), and 150 mM KNO_3 was determined by applying an external load voltage via platinum wire electrodes. I found that the open-circuit voltage increased as the temperature difference between the two half-cells increased, and, when the temperatures of the cold and hot cells were 20 and 70°C, respectively, the power output obtained from the *I–V* curve was 0.48 $\mu W m^{-2} K^{-2}$ (Figure 3-13a). Possibly, the power could be further increased by optimizing the electrode and cell structures. Next, the

voltage stability of the thermocell was evaluated, and no significant degradation was observed for at least 600 min (Figure 3-13b).

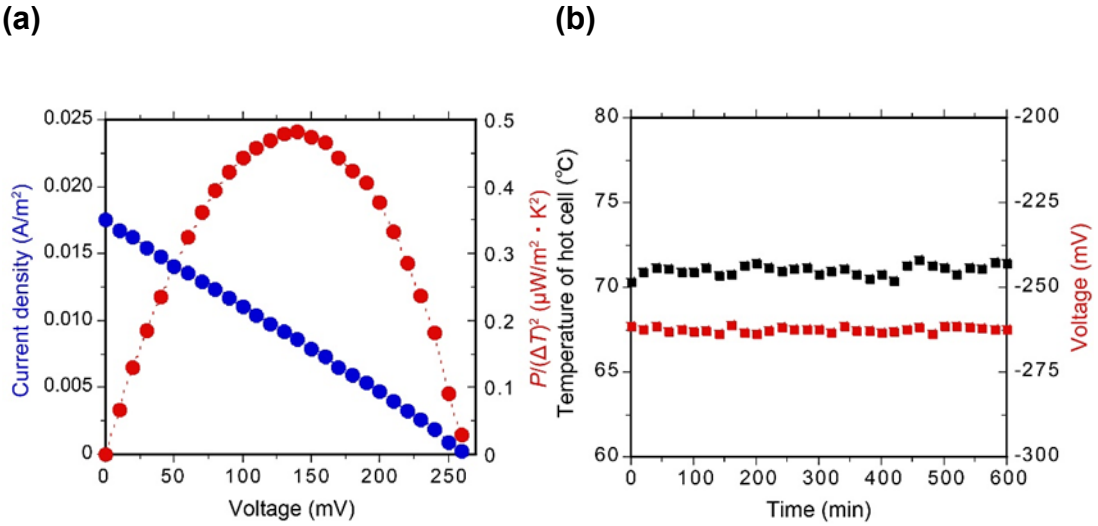

Figure 3-13. (a) *I–V* and *P–V* plots of the thermocell containing 2,7-AQDS (5.6 mM), AAc NPs ([AAc] = 2 mM, [NaOH] = 1 mM), and 150 mM KNO_3. (b) Variation in thermocell voltage with time. The temperatures of the cold and hot cells were 20 and 70 °C, respectively.

My thermocell configuration is suitable for obtaining accurate S_e measurements[23],[58],[59]. Therefore, using Eq. 3-1, the maximum *ZT* of the thermocell containing 2,7-AQDS and AAc NPs was calculated to be 8.0×10^{-2}. Compared with the *ZT* of the thermocell containing HQ, that of the thermocell with 2,7-AQDS is three-times larger. The *ZT* might well be improved by further optimizing each parameter. However, structural design of the cells such and shape of the cell and the distance

between electrodes will have a much greater impact on *ZT*. By optimizing the electrode selection and cell structure, the *ZT* value could be further improved[60]–[62].

3.4. Conclusions

In summary, the PCET reaction of various redox species and the VPT of various hydrogel NPs were combined to produce thermocells. Through the screening of redox species, electrolyte salts, and NPs, the conditions necessary to achieve optimal thermocell performance (S_e and open-circuit voltage) were determined. I found that the combination of 2,7-AQDS and poly(AAc-*co*-NIPAM) NPs achieved the highly efficient conversion of temperature differences to electrical energy at physiological temperature (around 37 °C). The thermocell showed a high S_e of −9.5 mV K^{-1}, which exceeds those of reported liquid-phase thermocells. In addition, by increasing the ionic conductivity of the thermocell using KNO_3, a *ZT* of 8.0×10^{-2} was obtained. The screening process presented in this study provides a guide for the rational design of high-performance thermocell systems based on hydrogel nanoparticles. Specifically, I found that the modification of the hydrogel NP properties and appropriate choice of redox species are key factors for optimizing thermocell performance and merit further exploration. Crucially, my system uses simple, inexpensive, and non-toxic materials to achieve high-efficiency thermoelectric conversion, and I believe that my findings will spur the development of devices such as flexible portable chargers for wireless/portable devices.

3.5. Appendix

3.5.1. Investigation of hydrophobic interaction between redox species and NPs

Four 5 mL 5.6 mM AQDS solutions with 150 mM KNO_3 containing 0 mM, 2 mM, 5.6 mM, and 15.7 mM AAc NPs were prepared using pure water. The solution was loaded into a dialysis membrane (MWCO 1K Da, Spectrum Laboratories, Inc.) and placed in a container containing 20 mL of pure water. They were dialyzed at 20°C and 60°C for at least 24 hours. The ultraviolet-visible (UV-Vis) spectra of the solution outside the dialysis membrane were recorded on an Agilent 8453 spectrometer (Agilent Technologies Inc., Santa Clara, CA, USA). Through the absorbance peak of AQDS at 327 nm (Figure 3-14), the equilibrium concentration of AQDS before and after dialysis can be observed to determine whether the hydrophobic interaction between redox species and NPs exists.

The UV-Vis spectra at 20°C and 60°C are shown in Figure 3-14b and Figure 3-14c, respectively. Under the condition that the concentration of AQDS remained unchanged, as the concentration of NPs increases, no significant changes in the concentration of AQDS that reach the equilibrium of dialysis were observed. Therefore, it can be inferred that the hydrophobic interaction between redox species and NPs is very weak and will not significantly affect the performance of thermocell.

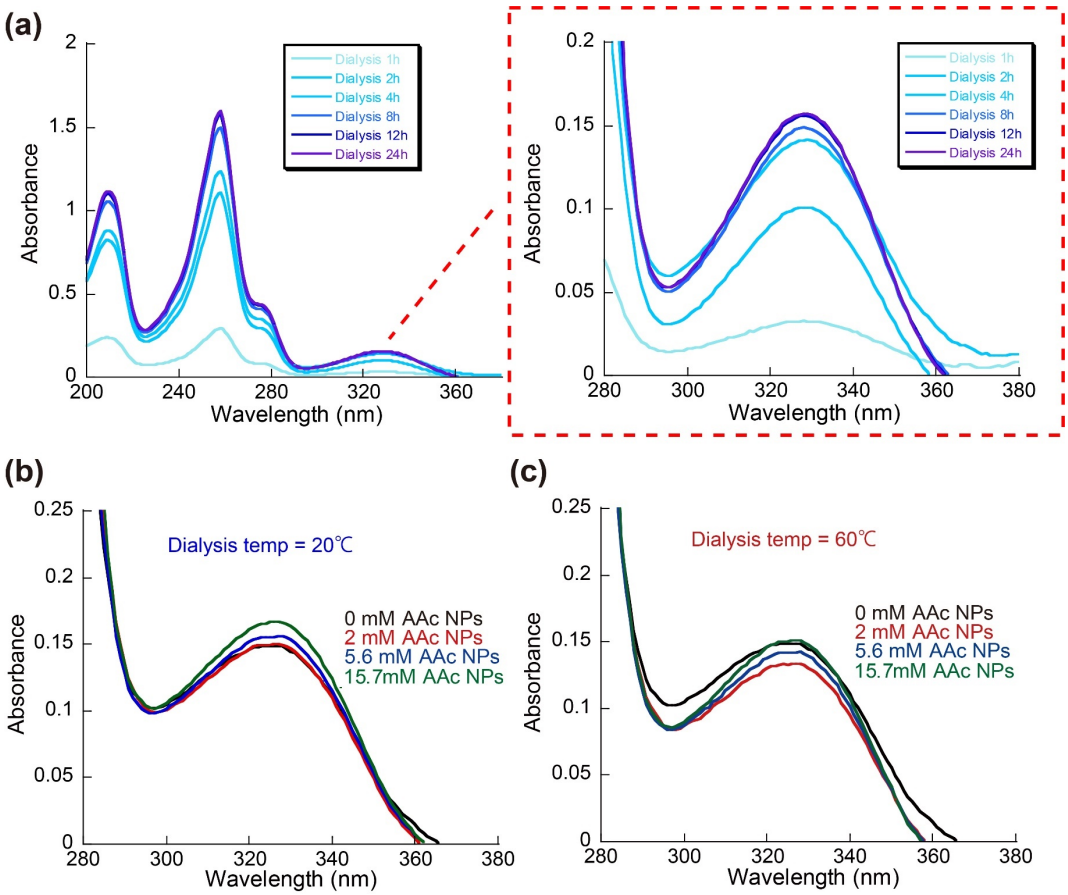

Figure 3-14. (a) The change of the UV-Vis spectra of the AQDS solution with time before reaching the dialysis equilibrium. The UV-Vis spectra of 5.6 mM AQDS solutions with 150 mM KNO_3 containing 0 mM, 2 mM, 5.6 mM, and 15.7 mM AAc NPs after dialysis at (b) 20°C and (c) 60°C for 24 hours.

3.5.2. Investigation of 2,7-AQDS dimerization in thermocell electrolyte solution

To investigate the dimerization of the redox species AQDS in thermocell, the cyclic voltammetry (CV) was employed. The 3 mm in diameter glassy carbon working electrode was polished with 0.05 μm alumina (BAS Co., Ltd.), rinsed with deionized water and then sonicated for 2 min in deionized water before starting the experiment.

Ag/AgCl in 3 M NaCl was used as reference electrode and platinum wire as counter. Three consecutive scans at scan rates of 20 mV s^{-1} were collected by electrochemical analyzer (ALS660E, BAS Co., Ltd.). The extrapolated current from the baseline was subtracted from the peak currents to account for capacitive charging. The voltammograms for AQDS in varying concentrations are shown in Figure 3-15.

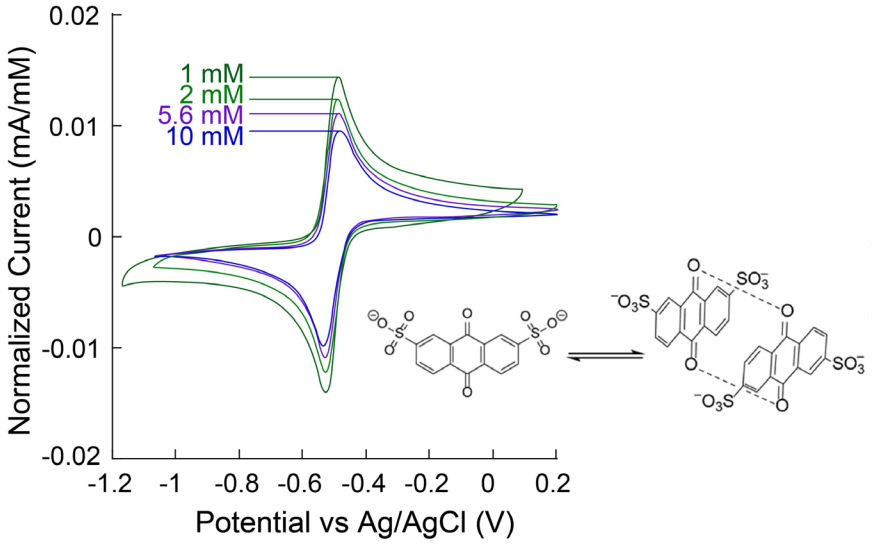

Figure 3-15. Concentration-normalized CVs for different concentrations of AQDS in pH=7.0 phosphate buffer. Scan rate = 20 mV s^{-1}.

The separation between the reductive and oxidative peaks is close to the reversible 30 mV for a two-electron process at 1 mM but increases to 48 mV at 10 mM. This shows that AQDS may change the electrochemical properties due to dimerization. The decrease of the concentration-normalized peak current is due to the decrease of the diffusion coefficient, which can infer the existence of AQDS dimer with larger molecular structure.[55]

3.6. Reference

[1] AlQattan, N.; Acheampong, M.; Jaward, F. M.; Ertem, F. C.; Vijayakumar, N.; Bello, T. *Renewable Energy Focus*. Elsevier Ltd December 1**, 2018**, pp 97–110.

[2] Tarancón, A. *Nat. Electron.* **2019**, *2*, 270–271.

[3] Forman, C.; Muritala, I. K.; Pardemann, R.; Meyer, B. *Renewable and Sustainable Energy Reviews*. Elsevier Ltd May 1**, 2016**, pp 1568–1579.

[4] Chu, S.; Cui, Y.; Liu, N. *Nat. Mater.* **2017**, *16*, 16–22.

[5] Kyriakopoulos, G. L.; Arabatzis, G. *Renewable and Sustainable Energy Reviews*. Elsevier Ltd April 1**, 2016**, pp 1044–1067.

[6] Haras, M.; Skotnicki, T. *Nano Energy*. Elsevier Ltd December 1**, 2018**, pp 461–476.

[7] Heremans, J. P. *Nature*. Nature Publishing Group **2014**, pp 327–328.

[8] He, J.; Tritt, T. M. *Science*. American Association for the Advancement of Science September 29**, 2017**, p 1369.

[9] Sootsman, J. R.; Chung, D. Y.; Kanatzidis, M. G. *Angewandte Chemie - International Edition*. November 2**, 2009**, pp 8616–8639.

[10] Zito, R. *AIAA J.* **1963**, *1*, 2133–2138.

[11] Liu, W.; Hu, J.; Zhang, S.; Deng, M.; Han, C.-G.; Liu, Y. *Mater. Today Phys.* **2017**, *1*, 50–60.

[12] Eastman, E. D. *J. Am. Chem. Soc.* **1928**, *50*, 292–297.

[13] Qian, G.; Yu, X.; Li, Z.; Wu, J.; Huang, R.; Lu, Y. *Energy Convers. Manag.*

2020, *217*, 113005.

[14] Zhou, H.; Liu, P. *ACS Appl. Energy Mater.* **2018**, *1*, 1424–1428.

[15] Han, C. G.; Qian, X.; Li, Q.; Deng, B.; Zhu, Y.; Han, Z.; Zhang, W.; Wang, W.; Feng, S. P.; Chen, G.; Liu, W. *Science* . **2020**, *368*, 1091–1098.

[16] Dupont, M. F.; MacFarlane, D. R.; Pringle, J. M. *Chem. Commun.* **2017**, *53*, 6288–6302.

[17] Quickenden, T. I.; Mua, Y. *J. Electrochem. Soc.* **1995**, *142*, 3985–3994.

[18] Im, H.; Kim, T.; Song, H.; Choi, J.; Park, J. S.; Ovalle-Robles, R.; Yang, H. D.; Kihm, K. D.; Baughman, R. H.; Lee, H. H.; Kang, T. J.; Kim, Y. H. *Nat. Commun.* **2016**, *7*, 10600.

[19] Zhou, H.; Yamada, T.; Kimizuka, N. *J. Am. Chem. Soc.* **2016**, *138*, 10502–10507.

[20] Zhou, H.; Yamada, T.; Kimizuka, N. *Bull. Chem. Soc. Jpn.* **2021**, bcsj.20210061.

[21] Yu, B.; Duan, J.; Cong, H.; Xie, W.; Liu, R.; Zhuang, X.; Wang, H.; Qi, B.; Xu, M.; Wang, Z. L.; Zhou, J. *Science* . **2020**, *370*, 342–346.

[22] Duan, J.; Feng, G.; Yu, B.; Li, J.; Chen, M.; Yang, P.; Feng, J.; Liu, K.; Zhou, J. *Nat. Commun.* **2018**, *9*, 1–8.

[23] Guo, B.; Hoshino, Y.; Gao, F.; Hayashi, K.; Miura, Y.; Kimizuka, N.; Yamada, T. *J. Am. Chem. Soc.* **2020**, *142*, 17318–17322.

[24] Huynh, M. T.; Anson, C. W.; Cavell, A. C.; Stahl, S. S.; Hammes-Schiffer, S. *J. Am. Chem. Soc.* **2016**, *138*, 15903–15910.

[25] Ikeshoji, T.; de Nahui, F. N. B. *J. Electroanal. Chem. interfacial Electrochem.* **1990**, *296*, 19–36.

[26] McCleskey, R. B. *J. Chem. Eng. Data* **2011**, *56*, 317–327.

[27] Zhang, Y.; Furyk, S.; Bergbreiter, D. E.; Cremer, P. S. *J. Am. Chem. Soc.* **2005**, *127*, 14505–14510.

[28] Zajforoushan Moghaddam, S.; Thormann, E. *Langmuir* **2017**, *33*, 4806–4815.

[29] Zhang, Y. S.; Khademhosseini, A. *Science* . **2017**, *356*, eaaf3627.

[30] Chen, G.; Hoffman, A. S. *Nature* **1995**, *373*, 49–52.

[31] Yoshida, R.; Uchida, K.; Kaneko, Y.; Sakai, K.; Kikuchi, A.; Sakurai, Y.; Okano, T. *Nature* **1995**, *374*, 240–242.

[32] Wang, J.; Gan, D.; Lyon, L. A.; El-Sayed, M. A. *J. Am. Chem. Soc.* **2001**, *123*, 11284–11289.

[33] Karg, M.; Pich, A.; Hellweg, T.; Hoare, T.; Lyon, L. A.; Crassous, J. J.; Suzuki, D.; Gumerov, R. A.; Schneider, S.; Potemkin, I. I.; Richtering, W. *Langmuir* **2019**, *35*, 6231–6255.

[34] Hoshino, Y.; Ohashi, R. C.; Miura, Y. *Adv. Mater.* **2014**, *26*, 3718–3723.

[35] Hoshino, Y.; Miyoshi, T.; Nakamoto, M.; Miura, Y. *J. Mater. Chem. B* **2017**, *5*, 9204–9210.

[36] Hoshino, Y.; Moribe, M.; Gondo, N.; Jibiki, T.; Nakamoto, M.; Guo, B.; Adachi, R.; Miura, Y. *ACS Appl. Polym. Mater.* **2020**, *2*, 505–514.

[37] Hoshino, Y.; Imamura, K.; Yue, M.; Inoue, G.; Miura, Y. *J. Am. Chem. Soc.* **2012**, *134*, 18177–18180.

[38] Tabor, D. P.; Gómez-Bombarelli, R.; Tong, L.; Gordon, R. G.; Aziz, M. J.; Aspuru-Guzik, A. *J. Mater. Chem. A* **2019**, *7*, 12833–12841.

[39] Sheraz, M. A.; Kazi, S. H.; Ahmed, S.; Anwar, Z.; Ahmad, I. *Beilstein J. Org. Chem.* **2014**, *10*, 1999–2012.

[40] Roldán, S.; Granda, M.; Menéndez, R.; Santamaría, R.; Blanco, C. *Electrochim. Acta* **2012**, *83*, 241–246.

[41] Wedege, K.; Dražević, E.; Konya, D.; Bentien, A. *Sci. Rep.* **2016**, *6*, 1–13.

[42] Mayer, J. M. *Annu. Rev. Phys. Chem.* **2004**, *55*, 363–390.

[43] Nawar, S.; Huskinson, B.; Aziz, M. *MRS Online Proc. Libr.* **2013**, *1491*.

[44] Uchimiya, M.; Stone, A. T. *Chemosphere* **2009**, *77*, 451–458.

[45] Friedrich, L. E. *J. Org. Chem.* **1983**, *48*, 3851–3852.

[46] Wiberg, C.; Carney, T. J.; Brushett, F.; Ahlberg, E.; Wang, E. *Electrochim. Acta* **2019**, *317*, 478–485.

[47] Massey, V. *Biochem. Soc. Trans.* **2000**, *28*, 283–296.

[48] Roldán, S.; Granda, M.; Menéndez, R.; Santamaria, R.; Blanco, C. *Electrochim. Acta* **2012**, *83*, 241–246.

[49] Hoober-Burkhardt, L.; Krishnamoorthy, S.; Yang, B.; Murali, A.; Nirmalchandar, A.; Prakash, G. K. S.; Narayanan, S. R. *J. Electrochem. Soc.* **2017**, *164*, A600--A607.

[50] Kirkaldy, N.; Chisholm, G.; Chen, J.-J.; Cronin, L. *Chem. Sci.* **2018**, *9*, 1621–1626.

[51] Harned, H. S.; Wright, D. D. *J. Am. Chem. Soc.* **1933**, *55*, 4849–4857.

[52] Carney, T. J.; Collins, S. J.; Moore, J. S.; Brushett, F. R. *Chem. Mater.* **2017**, *29*, 4801–4810.

[53] Khataee, A.; Wedege, K.; Dražević, E.; Bentien, A. *J. Mater. Chem. A* **2017**, *5*, 21875–21882.

[54] Wedege, K.; Dražević, E.; Konya, D.; Bentien, A. *Sci. Rep.* **2016**, *6*, 1–13.

[55] Wiberg, C.; Carney, T. J.; Brushett, F.; Ahlberg, E.; Wang, E. *Electrochim. Acta* **2019**, *317*, 478–485.

[56] Duan, J.; Yu, B.; Liu, K.; Li, J.; Yang, P.; Xie, W.; Xue, G.; Liu, R.; Wang, H.; Zhou, J. *Nano Energy* **2019**, *57*, 473–479.

[57] Eastman, E. D. *J. Am. Chem. Soc.* **1928**, *50*, 292–297.

[58] Gunawan, A.; Lin, C.-H.; Buttry, D. A.; Mujica, V.; Taylor, R. A.; Prasher, R. S.; Phelan, P. E. *Nanoscale Microscale Thermophys. Eng.* **2013**, *17*, 304–323.

[59] Kang, T. J.; Fang, S.; Kozlov, M. E.; Haines, C. S.; Li, N.; Kim, Y. H.; Chen, Y.; Baughman, R. H. *Adv. Funct. Mater.* **2012**, *22*, 477–489.

[60] Hu, R.; Cola, B. A.; Haram, N.; Barisci, J. N.; Lee, S.; Stoughton, S.; Wallace, G.; Too, C.; Thomas, M.; Gestos, A.; Dela Cruz, M. E.; Ferraris, J. P.; Zakhidov, A. A.; Baughman, R. H. *Nano Lett.* **2010**, *10*, 838–846.

[61] Holubowitch, N. E.; Landon, J.; Lippert, C. A.; Craddock, J. D.; Weisenberger, M. C.; Liu, K. *ACS Appl. Mater. Interfaces* **2016**, *8*, 22159–22167.

[62] Kim, J. H.; Kang, T. J. *ACS Appl. Mater. Interfaces* **2019**, *11*, 28894–28899.

Chapter 4. Improvement of Thermocell Performance by Optimized Device Design using Carbon Nanotube Electrodes and Electrolyte Filled Separators

Abstract

Liquid-state thermocells are attracting attention as thermoelectric conversion devices due to their simple system and low cost. However, the development of thin, flexible, and efficient practical devices faces many challenges. In this study, I used flexible carbon nanotube buckypaper as an electrode, and used a laser-processed porous polytetrafluoroethylene film as a separator to maintain a stable temperature gradient at an electrode spacing of 50 μm. Replacing the conventional metal electrode with a carbon nanotube electrode with larger surface area and optimizing the impact of mass and heat transfer through the separator in the individual cells increased the overall power density. According to my previous research, thermal responsive hydrogel nanoparticles containing acrylic acid and anthraquinone-2,7-disulfonic acid with optimal concentration and composition were selected as the thermocell electrolyte. By improving liquid-state thermocell device design, a high output power of 0.82 mW m^{-2} K^{-2} can be achieved at temperature between 33 and 37 °C. This high output power density makes it possible to apply the planar liquid-state thermocells to harvest human body heat through wearable devices. At a low inter-electrode spacing, the thermocell separator design rationale was discussed through the effects of natural convection, mass transfer, and heat transfer according to the cell orientation change. The improved method of this cell and separator design also shows a certain generality and can be applied to thermocells containing other electrolytes.

.

4.1. Introduction

Waste heat thermal energy is widely distributed in the environment, ranging from industrial production and power generation processes to transportation and residential activities.[1] Ultra-low-quality waste heat (temperature below 130 °C) , which accounts for 63% of total waste heat emissions, is projected to be a major sustainable energy source.[2],[3] For example, the human body is an important source of ultra-low-quality waste heat, which is responsible for the continuous production of heat through metabolic functions[4]. The human body releases about 100-525 W of heat, which is continuous and widespread[5]. Converting this heat into electricity has the potential to power Internet-of-Things sensors, especially wearable devices. However, the development of thin, flexible, and efficient thermoelectric devices for ultra-low-quality waste heat harvesting still faces many challenges such as a low power density of single cells and stability issues.[6]

Until relatively recently, most research into thermoelectric conversion was in solid-state.[7] Conventional solid-state thermoelectric devices such as thermoelectric generators (TEGs) are costly and inflexible and only suitable for waste heat harvesting in factories and power plants.[8]–[10] The thermoelectric conversion efficiency of converting a limited heat source into electrical energy is the key.[11],[12] However, for applications such as harvesting human body heat to power wearable devices, the heat source is free and can be obtained in large quantities, thus achieving a high output power density is more concerned.[13]–[15]

Thermocells, especially liquid-state thermocells (LTCs) are a cost-effective and promising approach to harvesting ultra-low-quality waste heat energy with high output power.[16],[17] The principal advantage of LTCs is the high Seebeck coefficient (S_e) which is one or two order of magnitude higher than that of conventional solid-state thermoelectric devices.[18],[19] The high S_e make LTCs can autonomously produce high electrical output power when the electrodes exist in a non-isothermal state. I have reported LTCs using the volume phase transition (VPT) of hydrogel nanoparticles (NPs) and achieved the high S_e values of +6.1 and –6.7 mV K^{-1} [20]. As mentioned in the previous chapter, by optimizing the cell composition design, the S_e of this LTC can be further increased to -9.5 mV K^{-1}. Since the maximum S_e is obtained near the NPs phase transition temperature of about 35 °C, this LTC technology has a huge potential for converting human body heat into electricity with high power density.

To obtain higher output power density, the LTC that already has high S_e needs to further increase the current density of the device. A common method to increase current density is to use electrode materials with a larger effective surface area; another method is to reduce the distance between electrodes.

Carbon materials with nanostructures, such as carbon nanotubes (CNTs) and graphite, have been extensively studied for their potential as electrode materials.[21],[22] These materials have a large effective surface area which increases the number of redox reaction sites, and therefore, can effectively increase the current and power per unit electrode area.[13],[23] Hu et al. first used the carbon multiwalled nanotube electrode in

LTCs containing ferricyanide/ferrocyanide electrolyte in 2010 and obtained cell performance three times better than conventional LTCs.[24] This result showed the possibility of using CNT electrodes to enhance the output power density. Im et al. used CNT aerogel sheets cylindrically wound around a tungsten wire as current collecting electrodes and a record high thermoelectric conversion efficiency of 3.95% was obtained.[19] However, the relatively complex manufacturing process needs to be simplified to make it feasible in practical applications. In this study, electrodes consisting of multi-walled CNT buckypaper were used. It is formed by a large number of CNTs dispersed in a methanol solution and has a porous structure with a high surface area. As a heat collecting electrode, it has relatively excellent flexibility and ductility. While improving cell performance, it also meets the material performance requirements of harvesting body surface waste heat through wearable devices.[6]

Previous studies and simulations have shown that reducing the inter-electrode spacing can increase the maximum power density due to the reducing of internal resistance.[25],[26] However, there are few examples of high efficiency LTCs with an inter-electrode spacing below 1mm. This is because after the electrode distance decreases, the temperature gradient is greatly reduced due to the reduction of the heat transfer distance, and a short circuit may be caused due to a small deformation of the electrode materials.[27],[28] As reported by Holubowitch et al.[29], because of the inter-electrode spacing decreasing, thermal resistance between the external source and the electrolyte gives rise to a more significant nonideal loss of heat. Especially in the case of using CNT buckypaper electrodes, the inter-electrode temperature differential of a

thermocell is approximately half of that external to the thermocell. The essence of thermocell is to convert the temperature difference into electric energy, and the stability of the temperature differential is the key point. It has been reported that inserting separators or membranes between two electrodes can effectively maintain the gradient of temperature and avoid the short circuit problem.[30],[31] Therefore, a LTC with a lower inter-electrode spacing can be designed to obtain a greater power density by using a separator. Recently, a ferricyanide/ferrocyanide LTC using a 0.2 mm thick cotton separator membrane with an inter-electrode spacing of 2.6 mm has been studied. The use of the separator maintains a stable and high temperature difference of 81 °C. Therefore, this LTC achieved a record high power density of ~12 W m^{-2}.[32] In the present study, a laser-processed porous PTFE film was used as a separator to achieve an inter-electrode spacing of 50 μm to improve cell performance. As a control experiment, other electrode and separator materials were also employed in the low inter-electrode spacing cell design to verify the influence of natural heat convection, mass transfer, and heat transfer in the thermocell on the improvement of cell performance.

4.2. Materials and experiments

4.2.1. Materials

The following chemicals and materials were obtained from commercial sources and used as received unless otherwise stated. Sodium dithionite (DITH, purity > 85.0%) was obtained from Tokyo Chemical Industry Co., Ltd. NaOH and KNO_3 were obtained from Kanto Chemical Co., Inc. Anthraquinone-2,7-disulfonic acid (2,7-AQDS, purity > 95.0%) was obtained from Wako Pure Chemical Industries, Co., Ltd. The water used in this study was purified using a Direct-Q Ultrapure Water System (Merck, Ltd.).

4.2.2. Preparation of Electrolytes

The optimized thermocell electrolyte containing 5.6 mM 2,7-AQDS redox species, 5.9 mg mL^{-1} poly(acrylic acid-*co*-*N*-isopropylacrylamide) (AAc NPs), and 150 mM KNO_3 was prepared as my pervious report in chapter 3 (Scheme 4-1). The pH values of the AAc NPs solutions were adjusted to be equal to the apparent pK_a of the acids in the NPs by adding NaOH ([AAc] = 2 mM, [NaOH] = 1 mM). 0.5 eq of DITH was added to solutions of 2,7-AQDS to adjust the ratio of the oxidized state (AQDS) to the reduced state (hydroquinone form of AQDS, AH_2DS) to 1:1.

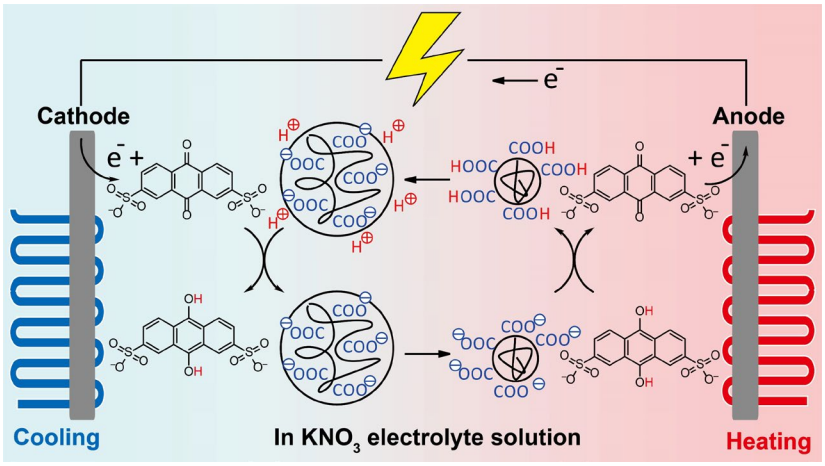

Scheme 4-1. Optimal electrolyte composition of the thermocell.

4.2.3. Preparation of CNT electrodes

The CNT buckypaper, a pure CNT sheet with an areal density of 20 g m^{-2}, was acquired from Zeon Co., Ltd. of Japan. CNTs in buckypapers are dispersed using aqueous solutions, methanol solutions and aqueous solutions with surfactants. The CNT buckypaper was cut into a 50 mm × 50 mm square, and the surface was washed three times with deionized water. The cleaned CNT buckypaper is directly used as a thermocell electrode and has not undergone other modification and lamination of CNTs.

4.2.4. Scanning electron microscope (SEM) observation and Brunauer–Emmett–Teller (BET) measurement of CNT electrode

The porous structure of the CNT electrode was observed by SEM (SU8000, Hitachi High-Tech Co., Ltd.). The CNT electrodes using different dispersion methods

were cut to a suitable size, washed with deionized water three times, and then the surface was observed.

The surface area of the CNT buckypaper electrode was measured by N_2 adsorption experiments at liquid nitrogen temperature (−196 °C, 77 K) on a Belsorp-Mini adsorption device (Microtrack Bell Co., Ltd., Japan), after evacuating samples at 25 °C for 24 h (< 0.9 Pa). The surface area of the CNT buckypaper electrode was calculated from N_2 adsorption–desorption isotherms using the BET method. (BELSORP-mini analysis software). The pore size distributions were obtained by applying Barrett–Joyner–Halenda (BJH) methods to the nitrogen adsorption isotherms at 77 K.[33]

4.2.5. Preparation of electrolyte filled separators

The separators with thicknesses of 0.05 mm and 0.1 mm are made by laser processing using commercially available PTFE films. Laser processing is performed by Spectronics Co., Ltd. using LDH-G series machines. PTFE films (thickness 0.05 mm and 0.1 mm) was cut out into a 60 mm square, and a large number of circular pores were machined in a hexagonal grid in the central 30 mm square area (Figure 2). The diameter of each pore on the surface was from 40 μm to 80 μm, the pore spacing was from 60 μm to 120 μm, and the taper angle was as small as possible. In addition, fiber mesh (RE2012-100, CSM Co., Ltd.), filter papers (Kiriyama-5A, Kiriyama Glass Works Co., Ltd.) and polyethylene (PE) porous membrane (Medium Pore ≤ 200nm, Teijin Co., Ltd.) were used in a control experiment.

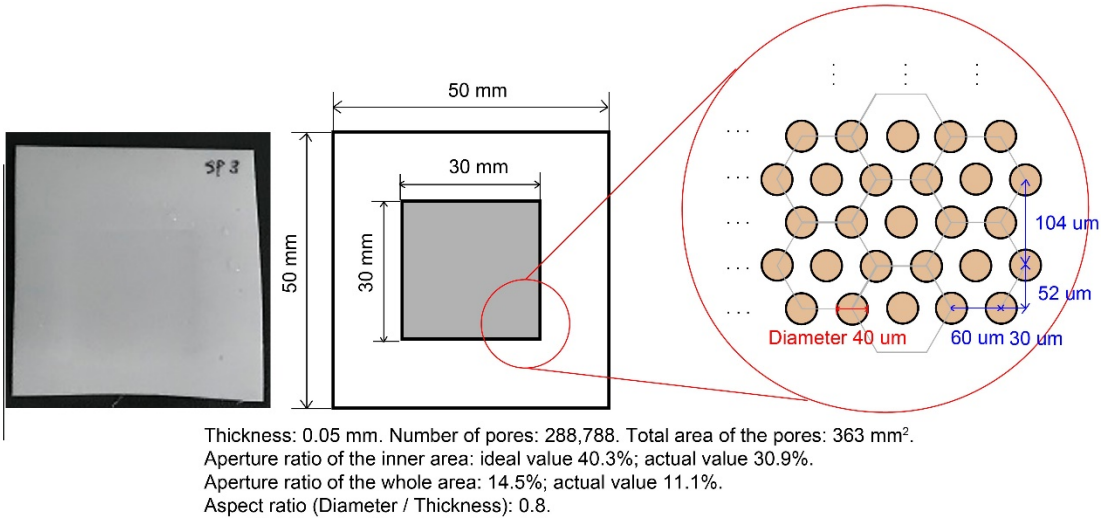

Figure 4-1. A design example of a separator processed with a PTFE film. In the case of a thickness of 0.05 mm, an aperture of 40 μm and a pore spacing of 60 μm: the number of pores is 288,788, the aperture ratio is 40.3%, and the aspect ratio (aperture/thickness) is 0.8.

The surfaces of PTFE separators, fiber mesh and filter papers were observed using SEM (Miniscope® TM3030Plus, Hitachi Co., Ltd.) to determine the actual pore size and pore distribution.

To verify the influence of inter-electrode spacing and separator structure on cell performance, I used a separator processed by a 3D printer to conduct a control experiment. The separators with thicknesses 3 mm in shapes of 50 mm × 50 mm squares are processed using a 3D printer (DWS XFAB2000, Seaforce Co., Ltd.). Its shape is designed using Fusion 360 software. The material of the separator is ceramic resin (DWS DM210) with regular circular holes. Three different structures are designed

(Figure 4-2). They have 109, 25, and 1 round hole to allow the electrolyte to pass through. The apertures are 1 mm, 2 mm, and 25 mm, respectively.

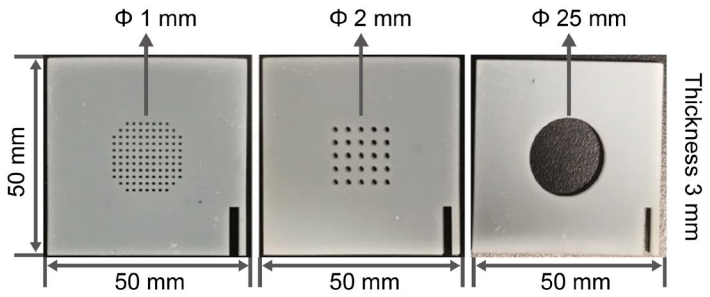

Figure 4-2. Photograph of separators processed by 3D printer with different design. From left to right, the aperture ratio of the separator is 3.7%, 3.1% and 19.6%, respectively. The aspect ratio (aperture/thickness) is 0.33, 0.67 and 8.33, respectively.

Before assembling the thermocells, separators were immersed in the electrolyte solution and evacuated by using a vacuum pump at 25 °C for 2 h to remove the air remaining in the separator pore structure, thus make the separator electrolyte filled.

4.2.6. Contact angle measurement

The contact angle of water droplets on the separator surface was measured by the sessile drop method. The contact angle of water droplets over time on the laser-processed PTFE separator surface indicated the penetration ability of the aqueous electrolyte. Before the measurement, the separator was immersed in distilled water, and

then laid flat on the glass plate. 2 μl distilled water was dropped on the surface of the separator. After the water droplet dropped, observe the change of its contact angle every 5 seconds to determine whether the water droplet can penetrate to the other side through the circular hole on the surface of the separator.

4.2.7. Design of thermocell devices with low inter-electrode spacing

Thermocell devices with low inter-electrode spacing are assembled using optimized electrolyte, two electrodes and electrolyte filled separators (Figure 4-3). The two ends of the thermocell are equipped with aluminum alloy blocks (thickness 10 mm) that have the same area as the electrodes. Two thermocouples with a diameter of 4 mm is inserted in the aluminum alloy blocks to measure the temperature difference. To insulate the aluminum alloy block and the outside cooler/heater and prevent the evaporation of electrolyte, a 0.025 mm thick oriented polypropylene (OPP) film is used without affecting the heat transfer as much as possible. As a control experiment, a platinum electrode (Tanaka Precious Metals Co., Ltd.) with a substrate of titanium, a thickness of 1 mm, and a platinum plating layer of 0.1 μm was used besides the CNT buckypaper electrode. Temperature of each cell was controlled separately with an external thermostatic device to circulate water into the aluminum water cooling block (40×60×12mm, Bewinner Co., Ltd.). To ensure a certain electrode spacing, the thermocell device is sandwiched by a vise. The thermocell device contained two electrodes and a separator filled with electrolyte solution.

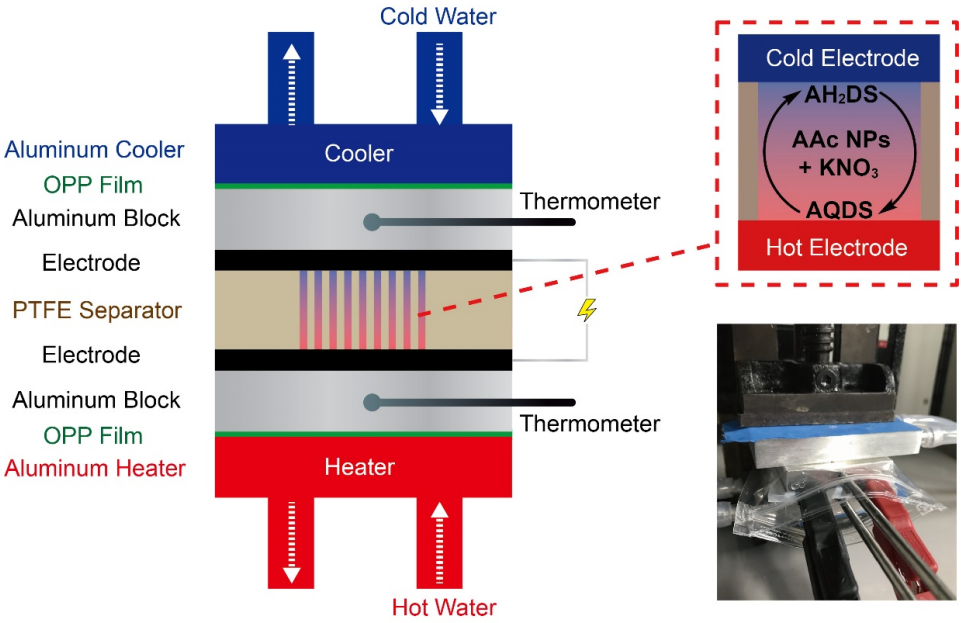

Figure 4-3. Scheme and photograph of cell components and their assembly into a low inter-electrode spacing thermocell.

4.2.8. Measurement of thermoelectric performance and efficiency

Before use, CNT electrodes were washed with deionized water three times, platinum electrodes were washed by soaking in concentrated sulfuric acid followed by rinsing in ultrapure water. The electrolyte composition was the same as that described above and filled in a separator between two electrodes. The current and voltage between the electrodes were measured using a Keithley 2401 source meter. Contacts from the source meter were clipped directly to hot and cold electrodes to minimize contact resistance. The temperature difference external to the thermocell (between two aluminum blocks) were monitored using two thermometers (TM-201). The temperature of the cold side electrode was maintained at approximately 33 °C. While one end of the

electrode was heated from 33 to 37 °C, the source meter was used to measure the output power of the thermocell. To obtain I–V and power curves, constant voltage steps were applied from 0 mV to open circuit voltage while recording current. When the current exceeds the measurement range, the power value was recorded to calculate the actual current. At least three I–V curves were acquired for each condition over about 30 min to ensure reproducible performance.

The energy conversion efficiency (η) of a thermocell is defined as the ratio of maximum electrical power output (P_{max}) from the cell to thermal power flowing through the cell[24]:

$$\eta = \frac{P_{max}}{Q} = \frac{V_{OC} \cdot I_{SC}}{4} \cdot \frac{1}{A \cdot \kappa\left(\Delta T_{ie}/d\right)} \qquad \text{Eq. 4-1}$$

where V_{oc} and I_{sc} are the open-circuit voltage and the short-circuit current, respectively. The P_{max} achieved at 0.5 V_{oc} and 0.5 I_{sc} because of thermocells are dominated by a limiting resistance and follow a $V = IR$ relationship.[34] d is the inter-electrode spacing (the thickness of the separator). κ is the electrolyte thermal conductivity, the thermal conductivity of a low-concentration NP solution can be approximated as that of water. A is the cross-sectional area of the cell. Ideally, the cross-sectional area is approximately equivalent to the total area of holes filled with electrolyte solution in case of using a separator, A_h. However, in the actual operation of the thermocell, considering the influence of the separator on the heat transfer and the temperature distribution between the hot and cold electrodes, the cross-sectional area can also be considered equivalent to the electrode area, A_e. ΔT_{ie} is the inter-electrode

temperature difference between hot and cold electrodes. In this study, to facilitate the measurement, a temperature difference measured by thermometers that is external to the thermocell (ΔT_{ext}) was used instead of ΔT_{ie}. In the ideal case for thermal energy harvesting, no heat is lost from the external source to the electrolyte, and $\Delta T_{ie} \approx \Delta T_{ext}$; However, in the case of using CNT buckypaper electrodes in low inter-electrode thermocells, the $\Delta T_{ie} < \Delta T_{ext}$ due to the relatively significant heat loss in the contact gap on the external side of the electrode (Figure 4-4a). For cells that do not use a separator, $\Delta T_{ie} << \Delta T_{ext}$ due to the relative increase in heat loss caused by the increase in thermal conductivity between the electrodes (Figure 4-4b).

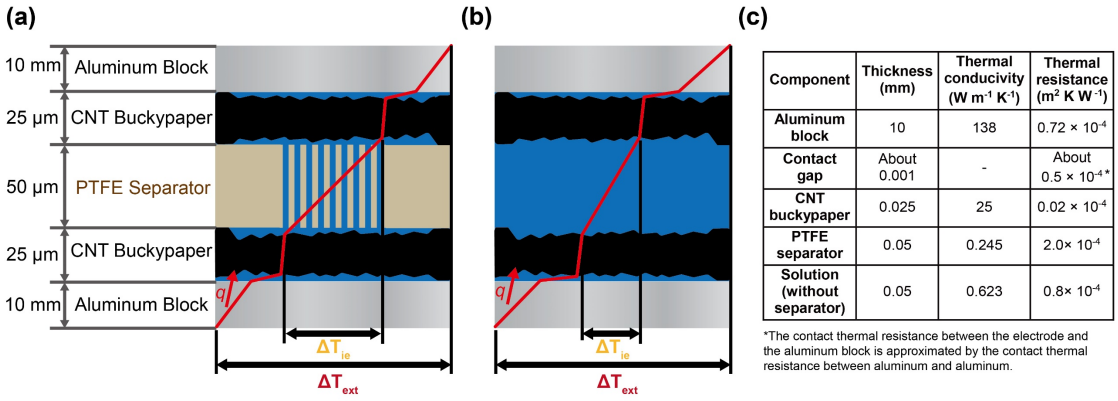

Component	Thickness (mm)	Thermal conducivity ($W\ m^{-1}\ K^{-1}$)	Thermal resistance ($m^2\ K\ W^{-1}$)
Aluminum block	10	138	0.72×10^{-4}
Contact gap	About 0.001	-	About 0.5×10^{-4} *
CNT buckypaper	0.025	25	0.02×10^{-4}
PTFE separator	0.05	0.245	2.0×10^{-4}
Solution (without separator)	0.05	0.623	0.8×10^{-4}

*The contact thermal resistance between the electrode and the aluminum block is approximated by the contact thermal resistance between aluminum and aluminum.

Figure 4-4. Schematic drawing of the heat transfer process in a low inter-electrode spacing thermocell using CNT buckypaper electrodes. Due to the thermally resistive gaps between electrodes and the aluminum blocks, thermal resistance in this region gives rise to unavoidable thermal losses that result in a difference of ΔT_{ie} and ΔT_{ext} when (a) a PTFE separator is employed and (b) no separator is employed. (c) The thickness, thermal conductivity, and thermal resistance of each component.

The theoretical energy conversion efficiency relative to Carnot efficiency (η_r) can be expressed by the following equation, when Eq. 4-1 is divided by the Carnot efficiency ($\eta_c = \Delta T/T_{hot}$):

$$\eta_r = \frac{S_e^2 \cdot T_{hot}}{4\kappa} \cdot \frac{d}{A \cdot R_{cell}} \qquad \text{Eq. 4-2}$$

where S_e is the Seebeck coefficient, R_{cell} is the internal resistance of the thermocell ($V_{oc} = S_e \Delta T$ and $I_{sc} = S_e \Delta T/R_{cell}$). T_{hot} is referred to temperatures external to the thermocell hot side.

4.2.9. Design of thermocells in control experiments

As a control experiment to make the effect of separator structure on cell performance clear, a low inter-electrode spacing thermocell was designed and assembled using other separator materials instead of laser-processed PTFE separator (Figure 4-5). All separators were properly trimmed to make they have the same aperture ratio (effective area 278 mm^2, 11.1% of the 50 mm × 50 mm electrode area). The CNT buckypaper electrode was employed in the thermocell, other cell components and cell performance measurement methods remained unchanged. In addition, I replaced the PTFE separators with 3 mm thick separators processed by a 3D printer and measured the cell performance (Figure 4-6). In order to measure the effect of natural convection of the cell under the condition of small error, the temperature difference between the

hot and cold electrodes ΔT_{ext} was increased from 4 °C to 18 °C (26 to 44 °C), and platinum plate electrodes were employed to obtain a relatively high voltage.

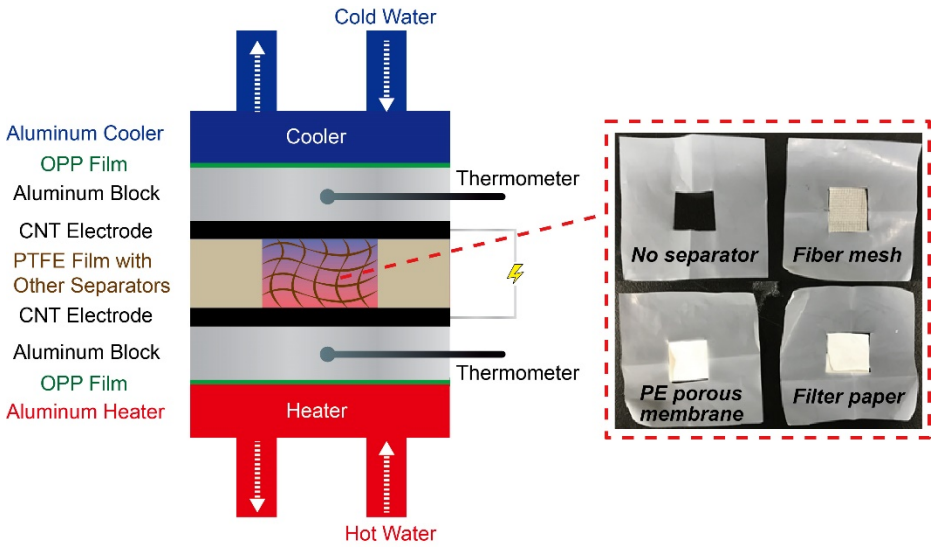

Figure 4-5. Schematic drawing and photograph of a thermocell with various separators.

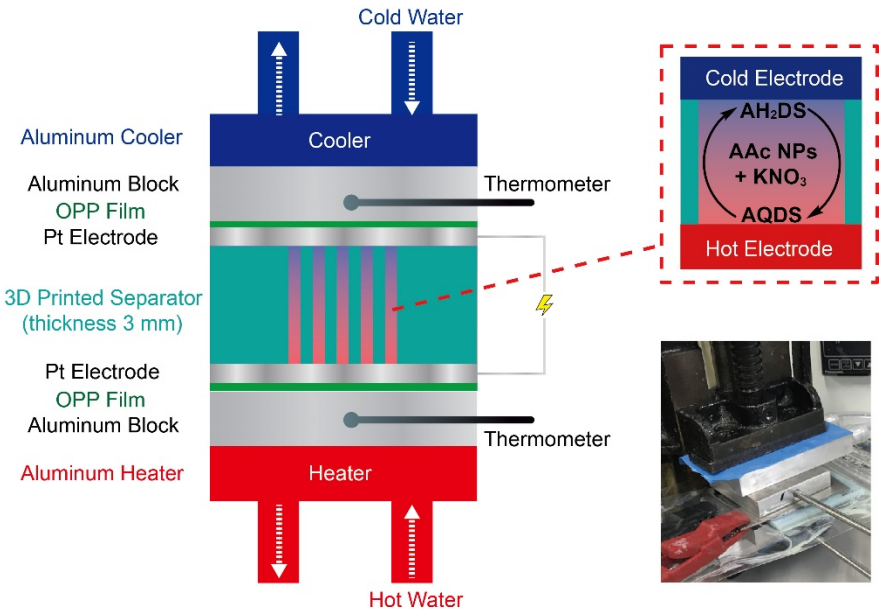

Figure 4-6. Schematic drawing and photograph of a thermocell with 3D separators.

4.2.10. Calculation of natural convection and heat transfer process

In my thermocell design, the cold-above-hot cell orientation was adopted (Figure 4-7a). Due to the temperature difference between the hot and cold electrodes, it may cause natural convection and enhance the mass and heat transfer, thereby affecting the cell performance.

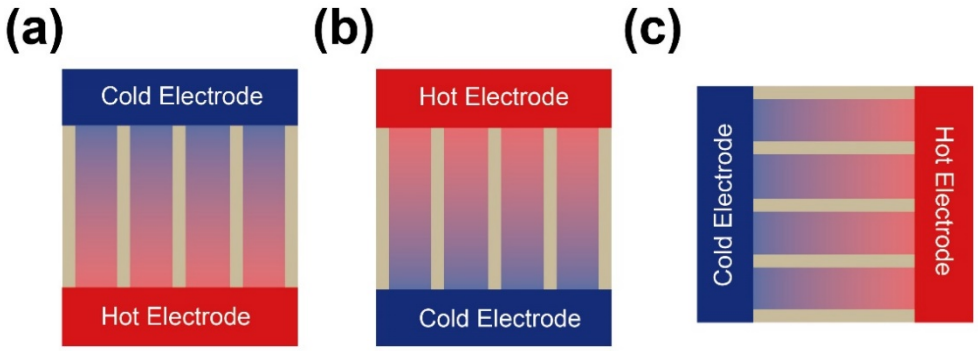

Figure 4-7. Three different cell orientations used in the thermocell design: (a) cold-above-hot, (b) hot-above-cold, and (c) horizontal.

Some dimensionless numbers in fluid mechanics can be used to describe the effects of natural convection.[35] The fluid is characterized by the Grashof (*Gr*), Schmidt (*Sc*), and Prandtl (*Pr*) number. The strength of natural convection on the heat flux density and current density is estimated by the Nusselt (*Nu*) and Sherwood (*Sh*) number, respectively. When the hot-above-cold cell orientation (Figure 4-7b) is adopted, there is no natural convection ($Nu = Sh = 1$).[25] When the cold-above-hot cell orientation is adopted, the effect of natural convection can be calculated by the following equation:[36]

$$Nu = 0.147(GrPr)^{0.247} \quad Sh = 0.147(GrSc)^{0.247} \quad 2\times10^3 < GrPr < 5\times10^5$$

$$Gr = \frac{g(\rho_c-\rho_a)L^3}{\rho_\infty v^2} \quad Pr = \frac{v}{\alpha} \quad Sc = \frac{v}{D_{AB}} \qquad \text{Eq. 4-3}$$

where g is gravitational acceleration, ρ_a and ρ_c are the density of the electrolyte at the anode and cathode's surface, respectively, ρ_∞ the density of the bulk electrolyte (including the anions and/or the background electrolyte), L the distance between the hot and cold electrodes (the inter-electrode spacing), v the kinematic viscosity, α the thermal diffusivity, and D_{AB} the diffusion coefficient (or mass diffusivity). α/ D_{AB} ratio is also known as the Lewis (Le) number.[35]

Since the water content in the electrolyte is very large, I use water parameters instead of electrolyte parameters. These parameters are listed in Table. 4-1.

Table 4-1. Parameters of redox species and AAc NPs aqueous electrolyte.[35]

Parameter	Value
For water at 35 °C	
Density of bulk electrolyte (ρ_∞)	994.0 kg m^{-3}
Kinematic viscosity (ν)	7.243 × 10^{-7} m^2 s^{-1}
Thermal diffusivity (α)	1.5 × 10^{-7} m^2 s^{-1}
Mass diffusivity of electrolyte (D_{AB})	6.84 × 10^{-10} m^2 s^{-1}
Prandtl number (Pr)	4.83
Schmidt number (Sc)	1058.9
Dynamic viscosity (μ)	7.2 × 10^{-4} kg m^{-1} s^{-1}
Thermal conductivity (κ)	0.623 W m^{-1} K^{-1}
Specific heat (Cp)	4178 J kg^{-1} K^{-1}
For water at 26 °C	
Density of electrolyte at the cathode (ρ_c)	996.8 kg m^{-3}
For water at 44 °C	
Density of electrolyte at the anode (ρ_a)	990.7 kg m^{-3}

However, for the horizontal orientation (Figure 4-7c), Bejan and Tien[37] recommend the following *Nu* and *Sh* correlation when $10^3 < GrPr < 10^9$:

$$Nu/AR = 1 + \left\{\left[\frac{((GrPr)\cdot AR)^2}{362880}\right]^{-0.386} + (0.623(GrPr)^{0.2}/AR)^{-0.386}\right\}^{1/-0.386}$$

$$Sh/AR = 1 + \left\{\left[\frac{((GrSc)\cdot AR)^2}{362880}\right]^{-0.386} + (0.623(GrSc)^{0.2}/AR)^{-0.386}\right\}^{1/-0.386} \quad \text{Eq. 4-4}$$

where *AR* is aspect ratio (height/thickness) of the geometric reactive area of each electrode. The characteristic length *L* in the *Gr* number (Eq. 4-3) is the vertical height.

The design of the separator not only affects the natural convection, but also has an influence on the heat transfer in the thermocell. When the separator with straight passage holes is filled with electrolyte fluid, the correlation between the thermal conductivity of the separator and that of the separator material and the electrolyte can be expressed by the following equation[38]:

$$(\kappa_f - \kappa_{eff})/(\kappa_f - \kappa_s) \cdot (\kappa_s/\kappa_{eff})^{1/n} = 1 - \varepsilon \quad \text{Eq. 4-5}$$

where κ_f is thermal conductivity of fluid phase, κ_s is the thermal conductivity of solid phase, and κ_{eff} is the effective thermal conductivity of the fluid-solid coupled separator material. ε is the aperture ratio. *n* is a pore shape factor determined from experimental results. When the pore size ratio remains constant, the increase in pore diameter and the decrease in the number of pores leads to an increase in *n*, thus makes the κ_{eff} tend to be the volume-weighted average thermal conductivity of the fluid phase and the solid phase. In contrast, *n* decreases with the decrease of the pore diameter and the dense distribution of pores, which leads to a relatively lower κ_{eff}.

4.3. Results and Discussion

4.3.1. Characterization of CNT electrodes

SEM was used to observe the surface of CNT buckypaper dispersed in aqueous solution, methanol solution and surfactant (Figure 4-7). SEM micrographs show the degree of dispersion of CNTs and the porous structure they form.

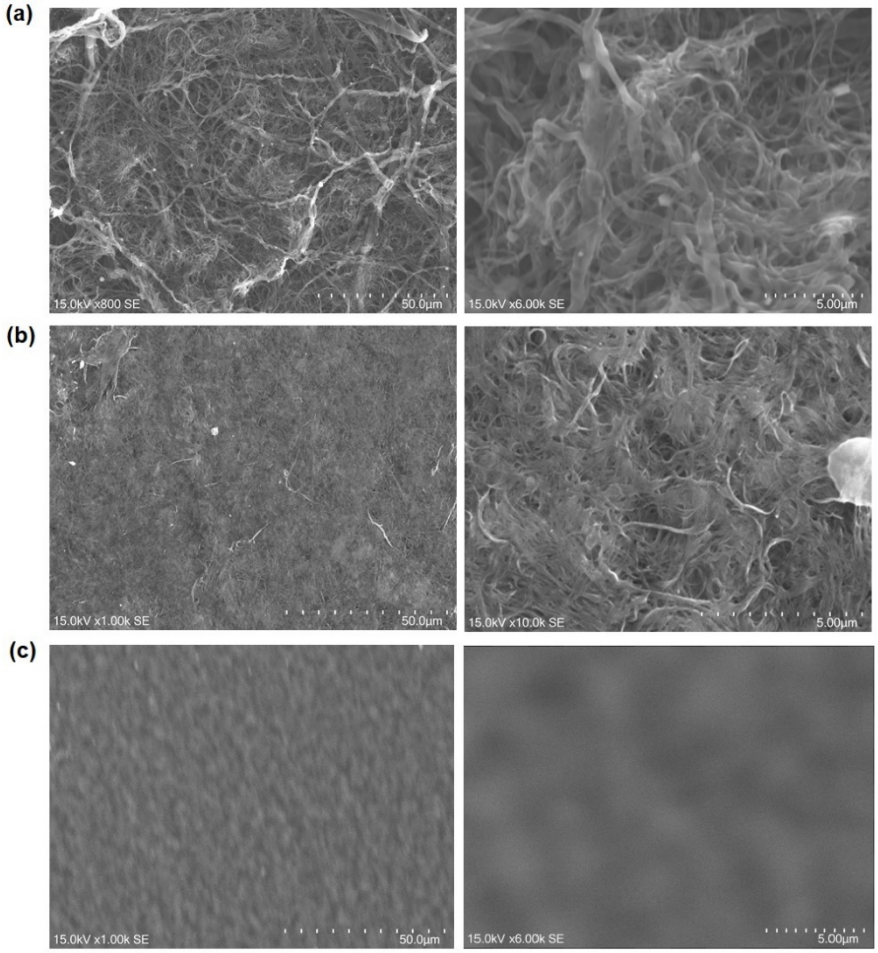

Figure 4-7. Low- and high-resolution SEM images of CNT buckypaper dispersed in (a) aqueous solution, (b) methanol solution and (c) surfactant.

The CNTs dispersed in the aqueous and methanol solutions form a porous structure. The diameter of a multi-walled CNT is about 10 to 100 nm. The CNTs dispersed in the aqueous solution and methanol solution showed a looser structure at high resolution (aperture < 500 nm). This porous structure can accommodate the diffusion of NPs with a molecular size of about 200 nm.[20] However, the CNTs containing surfactants form a dense surface, and the porous structure cannot be observed even at high resolution.

The specific surface areas and pore size distributions of the three types of CNTs were measured by the BET method (Figure 4-8). The result of the BET method of specific surface area mainly shows the process of CNT material adsorption and desorption of nitrogen (Figure 4-8a to 4-8c). the adsorption capacity of a monolayer on the outer surface of the sample was determined through the adsorption curve. The BET equation (Eq. 4-6) can be used to calculate the surface area from the adsorption capacity of a monolayer:[33]

$$\frac{p}{v(p_0-p)} = \frac{1}{C \cdot v_m} + \frac{C-1}{C \cdot v_m} \cdot \frac{p}{p_0} \qquad \text{Eq. 4-6}$$

where p_0 and p represent gas partial pressure and total pressure, respectively. v is the adsorption capacity, v_m is the adsorption capacity of the monolayer, and C is the adsorption constant. The specific surface areas were calculated using the BET method at relative pressures (p/p_0) of 0.01–0.2. The total pore volumes were determined from the amounts of N_2 uptake at p/p_0 of 0.99. The calculation showed that the surface area of the CNTs dispersed in the aqueous solution and the methanol solution are 53.5 and

54.3 m^2 g^{-1}, respectively. The surface area of the CNTs containing surfactants was not available because the amount of adsorption is too small. Its surface area is much smaller than the other two kinds of CNTs.

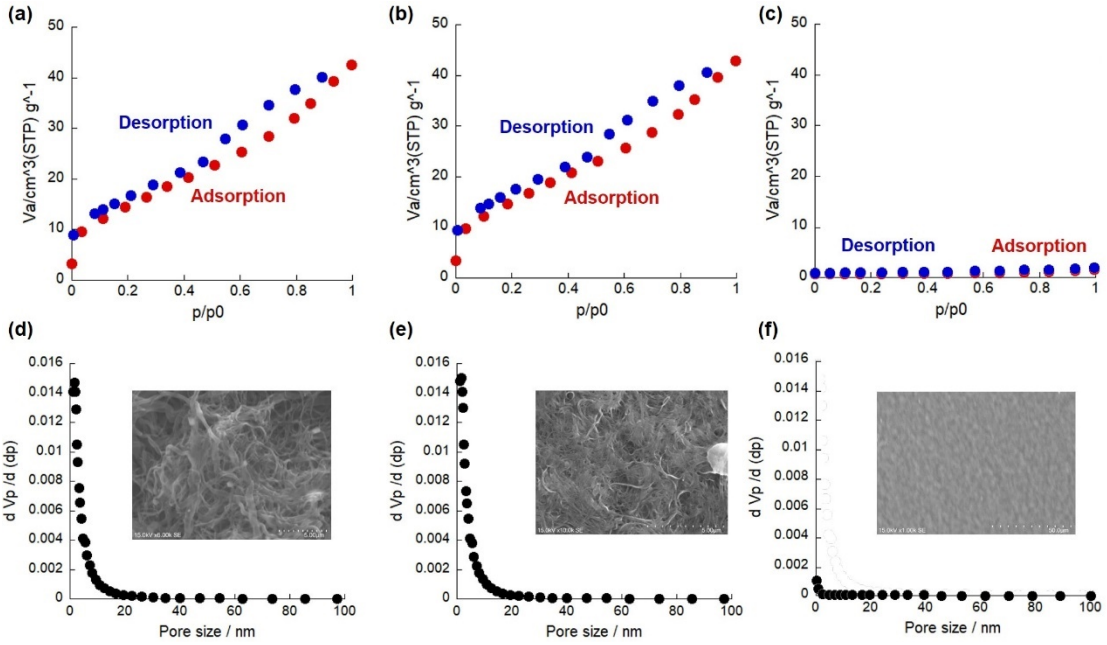

Figure 4-8. Nitrogen adsorption and desorption curve of CNT electrodes dispersed in (a) aqueous solution, (b) methanol solution and (c) surfactant. And pore size distribution by BJH calculations of CNT electrodes (SEM micrographs in the insets) dispersed in (d) aqueous solution, (e) methanol solution and (f) surfactant.

The pore size distribution results calculated by BJH method corroborated the above results (Figure 4-8d to 4-8f). The experimental results showed that the content of micropores with a pore diameter of less than 2 nm in the CNTs dispersed in aqueous

solution and methanol solution was 16.1 and 27.0 m^2 g^{-1}, respectively. The CNTs containing surfactants did not show a microporous structure.

Through the characterization of the CNT electrode, the CNT buckypaper dispersed in aqueous and methanol solutions showed a large surface area with porous structures. CNTs buckypapers have a high surface area can increase the number of reaction sites, and therefore, can effectively increase the current and power per unit electrode area.[39] However, macroscopically, the CNT material dispersed in the aqueous solution was brittle and easily adheres to the surface of other hydrophobic materials (such as the separator used in thermocell). Therefore, I selected the CNT material dispersed in methanol solution as the electrode and used it in the thermocell device.

4.3.2. Characterization of laser-processed PTFE separators

According to the design drawing (Figure 4-1), the laser-processed PTFE separator was observed through SEM (Figure 4-9). The low-resolution SEM image is used to confirm whether the pore size is distributed according to the hexagon (Figure 4-9a). The high-resolution SEM images of the front and back surfaces are used to confirm the size of the pore size and pore spacing (Figure 4-9b and 4-9c). Since the laser beam used for processing was conical, the aperture on the front of the separator was slightly larger than the back. The pore spacing and distribution form were consistent with the design. The effective surface area and apreture ratio are recalculated using a smaller backside pore size. The size data of all four separator designs are summarized in Table 4-1.

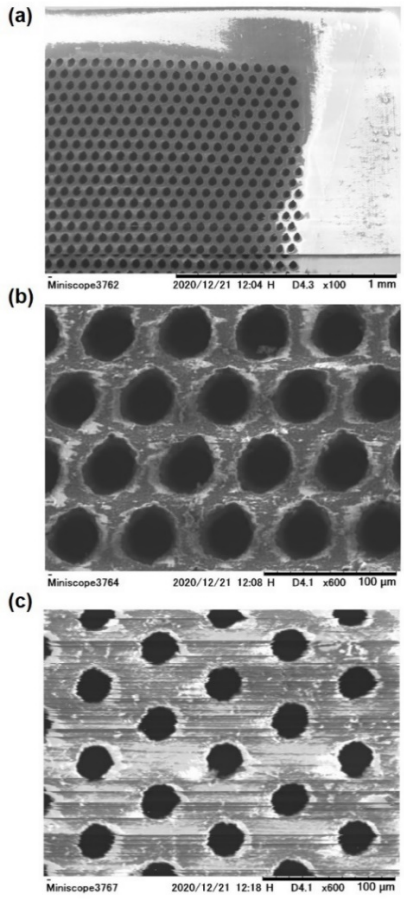

Figure 4-9. (a) Low-resolution SEM image of laser-processed PTFE separator. (b) High-resolution SEM image of the front surface and (c) the back surface.

Table 4-1. Dimensional data of laser-processed separators.

Name	Thickness (mm)	Diameter * (µm)	Spacing (µm)	Number of pores	Area (mm^2)	Aperture ratio	Aspect ratio
T50D35S60	0.05	35	60	288,788	278	30.9%	0.7
T50D35S120	0.05	35	120	163,342	157	17.5%	0.7
T50D70S120	0.05	70	120	72,394	278	30.9%	1.4
T100D70S120	0.1	70	120	72,394	278	30.9%	0.7

* Backside pore diameter observed from the SEM image.

The contact angle of water droplets over time on the laser-processed PTFE separator surface filled with electrolyte indicated the penetration ability of the aqueous electrolyte (Figure 4-10).

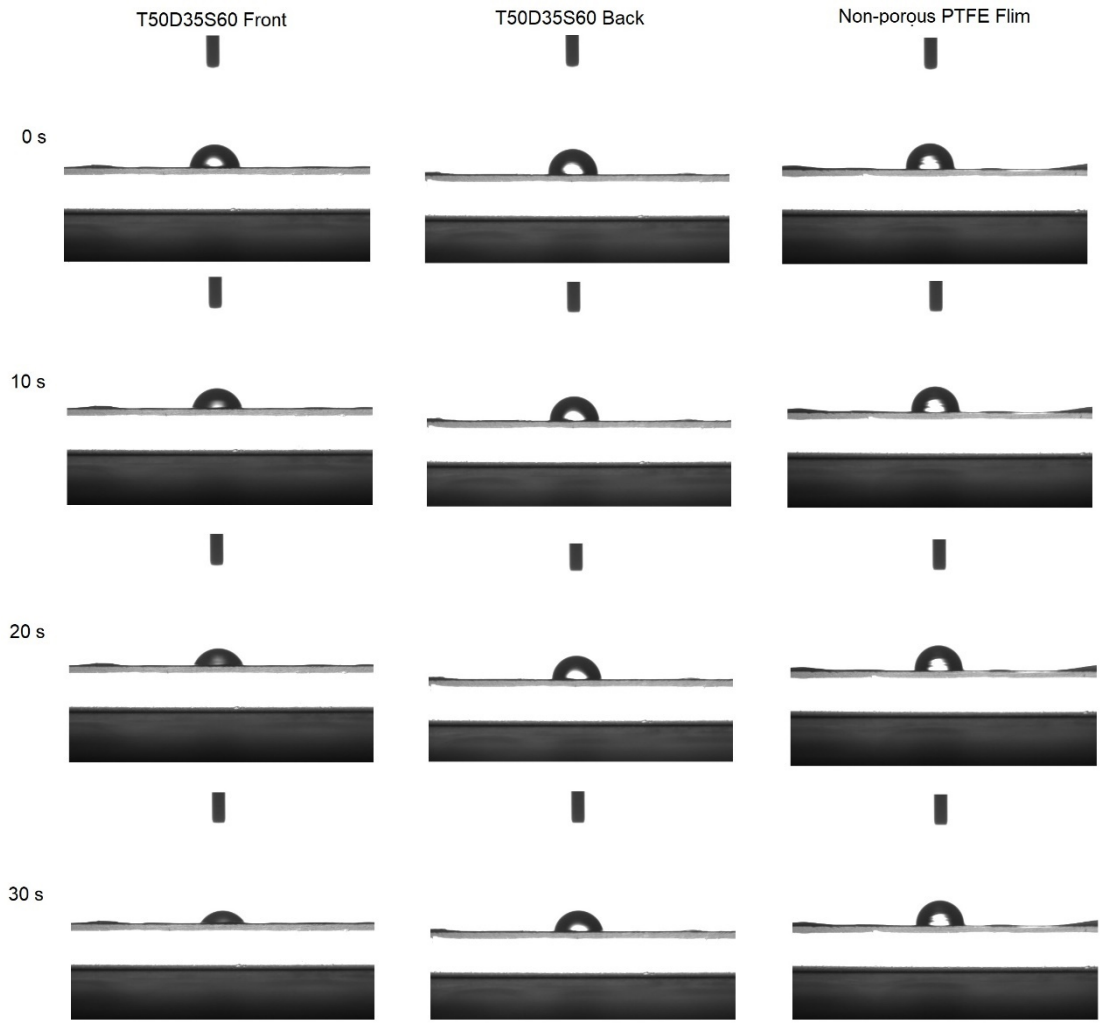

Figure 4-10. Images of a water droplet on front and back surface of laser processed PTFE film separator T50D35S60 and a PTFE film without laser processing. The changes in contact angle every 5 seconds are also showed.

For the front of the separator T50D35S60, the image showed that water droplets slowly penetrate the porous structure of the separator over time. In contrast, due to the smaller pore size on the reverse side of the separator, this permeation process became slower. The contact angle of the droplets on the surface of the separator without laser processing did not change. The experimental results showed that the electrolyte can be filled into and penetrate the circular pores processed by the laser. Therefore, the PTFE separator did not show excessive obstacles to the electrolyte mass transfer.

4.3.3. Thermoelectric performance of thermocells with low inter-electrode spacing

4.3.3.1. Improvement of thermoelectric performance by using CNT electrodes

The thermocell consisting of optimal electrolyte solution with a design of low inter-electrode spacing was assembled (Figure 4-3). At a temperature difference ΔT_{ext} of 4 °C (33 to 37 °C), the thermoelectric performance was measured by using CNT electrodes and platinum plate electrodes. As a representative example, the *I-V* curve of a cell with a T50D35S60 separator inserted between the electrodes was shown in Figure 4-11. The use of platinum plate electrodes (Figure 4-11a) and CNT electrodes (Figure 4-11b) resulted in different cell performance. The cell performance results using the other three separators were summarized in Table 4-2.

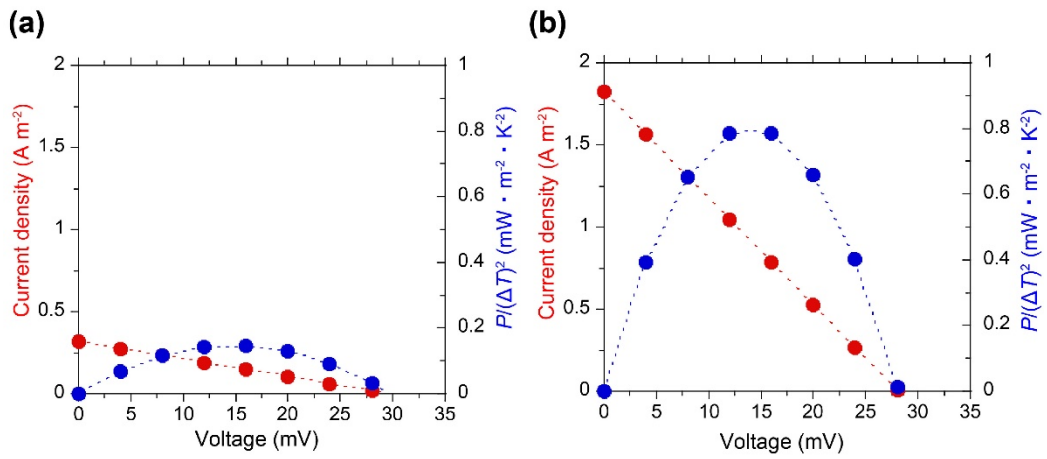

Figure 4-11. *I–V* and *P–V* plots of a low inter-electrode spacing thermocell device consisting of AQDS (5.6 mM) with AAc NPs (5.9 mg/mL, [AAc] = 2 mM, [NaOH] = 1 mM) and KNO_3 (150 mM). Measurement applied by using (a) platinum plate electrodes and (b) CNT electrodes. Temperatures external to the cold side and hot side of the cell were 33 and 37 °C, respectively.

At a temperature difference of 4 °C, the thermocell assembled with CNT and platinum electrodes obtained open circuit voltages of 29.5 and 28.7 mV, respectively. Due to the larger surface area, CNT electrodes showed better cell performance than platinum electrodes. It exhibited as a smaller internal resistance of 55 Ω, a greater current density of 1.83 A m^{-2} and a higher power density of 0.82 W m^{-2} K^{-2}. The results in Table 4-2 showed that for the other three separators, all the cell performance of the CNT electrode was better than that of the platinum electrode, with a maximum performance gap close to 6 times. This is because the CNT electrode has an effective surface area much higher than that of the platinum electrode, which provides faster electron transfer kinetics and more reaction sites for the redox reaction of the thermocell,

thereby reducing the internal resistance and greatly improving the cell performance.[40]–[42]

Table 4-2. Thermocell performance by using PTFE separators.

Separator	Inter-electrode spacing (mm)	Electrode	Power density* (mW m^{-2} K^{-2})	Short circuit current* (A m^{-2})	Open circuit voltage (mV)	Carnot-relative efficiency* (%)
T50D35S60	0.05	Platinum	0.15	0.32	29.5	0.0059
T50D35S60	0.05	CNT	0.82	1.83	28.7	0.032
T50D35S120	0.05	Platinum	0.13	0.27	30.5	0.0057
T50D35S120	0.05	CNT	0.78	1.68	29.6	0.031
T50D70S120	0.05	Platinum	0.15	0.34	28.1	0.0059
T50D70S120	0.05	CNT	0.80	1.87	27.2	0.032
T100D70S120	0.1	Platinum	0.09	0.18	32.3	0.0077
T100D70S120	0.1	CNT	0.50	1.01	31.7	0.040

*The cross-sectional area used in this calculation was A_h, the total area of pores filled with electrolyte in the separator.

4.3.3.2. Improvement of thermoelectric performance by using PTFE separators

A low inter-electrode spacing thermocell consisting of CNT electrodes, optimal electrolyte solutions and various separators was assembled to verify the effect of separators on cell performance. The thermoelectric performance was measured at a

temperature difference of 4 °C (33 to 37 °C) as much as possible. The cell performance of the four PTFE separation membranes has been summarized in Table 4-2. According to the experimental results, under the premise of a porous structure with moderate pore size, the pore size distribution (aspect ratio and aperture ratio) of the separator had no obvious influence on the output power density. The influence of different designs of separators on power density mainly depended on the inter-electrode spacing (separator thickness). Although the reduction of inter-electrode spacing reduced the thermoelectric conversion efficiency (Eq. 4-2), the output power density can be greatly improved.

To prove the necessity of separators in low inter-electrode spacing thermocells, and to make the effect of separator structure on cell performance clear, I conducted control experiments with other separator materials (Figure 4-5, 4-12). The results of control experiments using fiber meshes, filter papers and PE porous membranes instead of PTFE separators, and the experimental results with one hollow (approximately no separator), are summarized in Table 4-3. Considering the influence of the separator on the heat transfer and the temperature distribution between the hot and cold electrodes, the cross-sectional area used in this calculation was A_e, the total electrode area (2500 mm^2). And all separators were properly trimmed to make they have the same aperture ratio, 11.1%. The experimental results show that the open circuit voltage of the thermocell was close to 0 when the separator was not used. This was because the space between the electrodes is small, the small deformation of the electrode material can easily cause a local short circuit in the cell.

Table 4-3. Thermocell performance by using PTFE separators.

Separator	Inter-electrode spacing (mm)	Power density (mW m^{-2} K^{-2})	Short circuit current (A m^{-2})	Open circuit voltage (mV)	Carnot-relative efficiency (%)
T50D35S60	0.05	8.8×10^{-2}	0.203	28.7	3.5×10^{-3}
Fiber mesh	0.18	1.1×10^{-2}	0.072	11.8	1.5×10^{-3}
Filter paper	0.22	5.1×10^{-3}	0.011	29.3	8.9×10^{-4}
PE porous membrane	0.05	5.3×10^{-4}	1.0×10^{-3}	30.0	2.1×10^{-5}
No separator	0.05	NA*	NA*	< 0.1	NA*

* The value is too small to be measured accurately.

The mesh structure of the fiber mesh separator can avoid the occurrence of short circuits. However, it can be seen from the SEM image (Figure 4-12b) that fiber mesh separator has an extremely large pore size. Compared to laser-processed PTFE separators, the increase in pore diameter leads to an increase in pore shape factor n in Eq.4-5, thus increased the effective thermal conductivity κ_{eff}. The promotion of heat transfer caused a reduction of the inter-electrode temperature difference between hot and cold electrodes, ΔT_{ie}. Therefore, the open circuit voltage of the thermocell using the fiber mesh separator was lower, which weakened the cell performance.

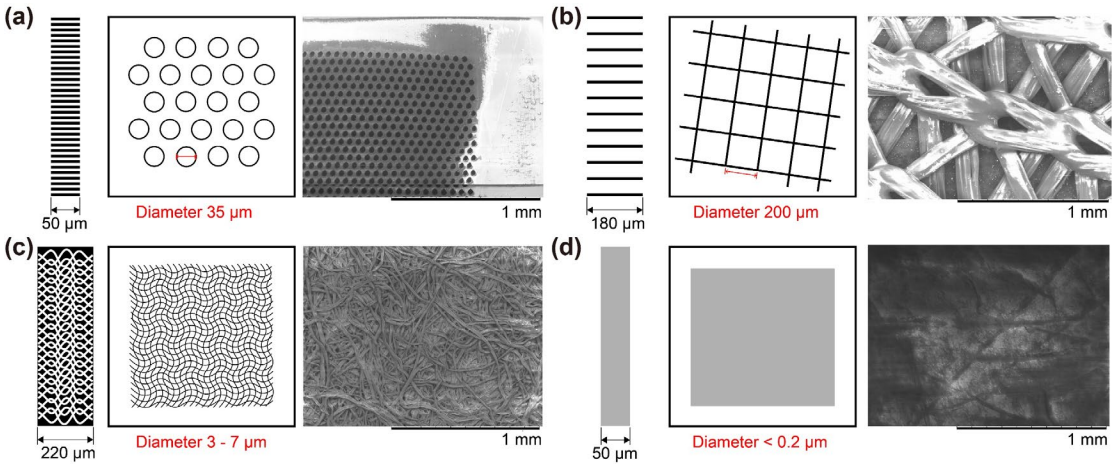

Figure 4-12. Cross-sectional view and SEM image of (a) the PTFE separator, (b) the fiber mesh, (c) the filter paper, and (d) PE porous membrane.

When filter paper was used as a separator, due to the small pore size with a dense structure and the tortuous mass transfer path (Figure 4-12c), the pore shape factor n and the effective thermal conductivity κ_{eff} in Eq.4-5 were decreased. Compared with the fiber mesh, the use of filter paper separators obtained a higher open circuit voltage. However, the internal resistance of the cell also increased substantially, thereby reducing the cell performance. The same phenomenon appeared in the experiment of PE porous membrane. Because the PE porous membrane has good insulation and heat insulation ability, using it as a separator can maintain a large temperature difference between the hot and cold electrodes, thereby generating a higher open circuit voltage. However, the pore size of the PE porous membrane is at the nanometer level (Figure 4-12d), and the mass transfer path is very tortuous, which leads to a substantial increase

in the internal resistance of the cell, thereby greatly reducing the current density and power density, and reducing the cell performance.

Compared with the above-mentioned separator materials, the laser-processed PTFE separator has moderate pore size. This porous structure ensures a relatively small n and κ_{eff}, which reduced the heat transfer perpendicular to the electrode direction. While maintaining a certain temperature difference between the hot and cold electrodes, the internal resistance of the thermocell has not been significantly increased due to the straight electrolyte diffusion path in the PTFE separator. By using optimal PTFE separator, my thermocell device achieved a higher power density of 0.088 W m^{-2} K^{-2} in an extremely thin structure than other separator materials. It should be mentioned that the cell performance of my thermocell can be further improved by optimizing the structure of the CNT electrode, such as using multilayer CNT structure[24],[29] or use aerogel CNT[19], to obtain greater output power density and thermoelectric conversion efficiency.

4.3.4. The effect of thermocell orientation and natural convection

In a low inter-electrode spacing thermocell, the factors that affect the mass transfer and heat transfer process become more complicated.[25] Previous studies and practical applications have shown that the geometric structure of the thermocell, especially the orientation of the cell, will affect the mass and heat transfer process by changing the strength of natural convection, which is ultimately reflected in the change of cell

performance.[25],[43] To investigate this effect, a thermocell with low inter-electrode spacing are assembled using optimized electrolyte, CNT buckypaper electrodes and electrolyte filled separators (Figure 4-3) with three different cell orientation (Figure 4-7). As a representative example, the *I-V* curves of cells with the T50D35S60 and the T100D70S120 separator in three different cell orientations were shown in Figure 4-13.

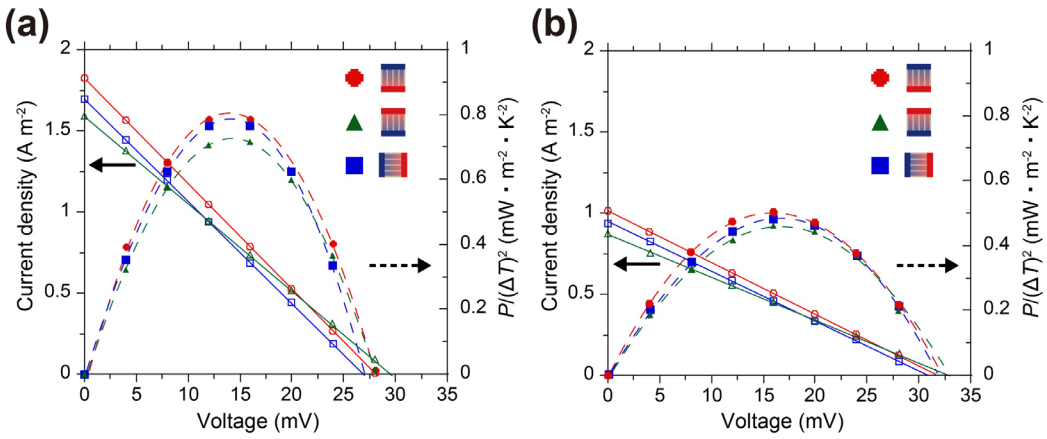

Figure 4-13. *I–V* and *P–V* plots of a low inter-electrode spacing thermocell consisting of AQDS (5.6 mM) with AAc NPs (5.9 mg/mL, [AAc] = 2 mM, [NaOH] = 1 mM) and KNO_3 (150 mM) in three different cell orientations. Measurement applied by using (a) T50D35S60 separator with a thickness of 50 μm and (b) T100D70S120 separator with a thickness of 100 μm. Temperatures external to the cold side and hot side of the cell were 33 and 37 °C, respectively.

The thermocells using two separators of different thicknesses did not show significant performance changes due to the orientation of the cell. According to the

electrolyte parameters in Table 4-1, substituting the thickness of the two separation membranes (50 and 100 μm) into Eq. 4-3, the natural convection effects of these two thermocells can be calculated. The Grashof numbers (*Gr*) of the thermocell with a 50 and 100 μm thick separator were obtained as 1.4×10^{-5} and 1.1×10^{-4}, respectively. Since the value of *Gr* is very low (*GrPr* < 2000), the natural convection effect in thermocell can be ignored.[35] Under this condition, the heat transfer process is pure heat conduction, and the mass transfer process is mainly concentration diffusion. Therefore, no matter how the cell orientation changes, natural convection cannot occur, and cell performance cannot be significantly affected.

Theoretically, as the inter-electrode spacing (the thickness of the separation membrane) increases, the effect of convection will increase, and the effect of cell orientation will also be promoted. When a 3 mm thick separator processed by 3D printer was employed in a thermocell, the calculated *Gr* is about 3044. The result indicates that in theory there is a certain natural convection effect (calculated *Nu* and *Sh* > 1). To verify the influence of inter-electrode spacing and cell orientation on cell performance, I used three separators processed by a 3D printer (Figure 4-2) to conduct a control experiment (Figure 4-6). the *I-V* curves of thermocells in three different cell orientations were shown in Figure 4-14.

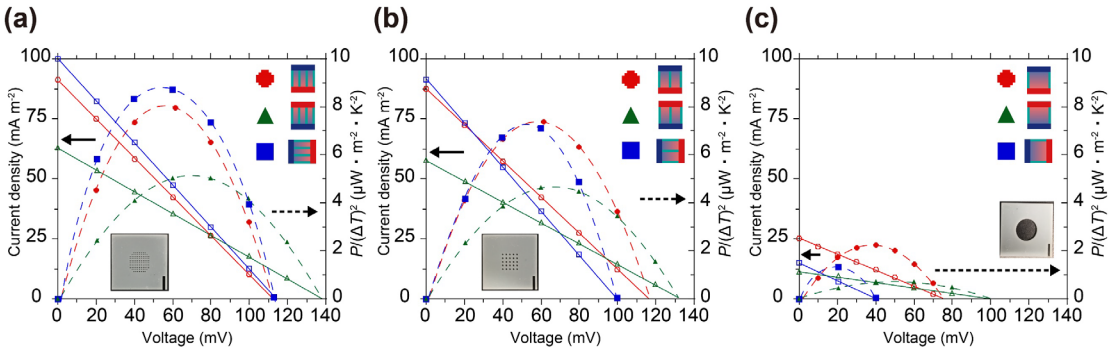

Figure 4-14. *I–V* and *P–V* plots of a 3 mm inter-electrode spacing thermocell consisting of AQDS (5.6 mM) with AAc NPs (5.9 mg/mL, [AAc] = 2 mM, [NaOH] = 1 mM) and KNO_3 (150 mM) in three different cell orientations. Measurement applied by using separators processed by 3D printer with different aspect ratio (aperture/thickness) of (a) 0.33, (b) 0.67 and (c) 8.33. Temperatures external to the cold side and hot side of the cell were 26 and 44 °C, respectively.

The change of cell performance along with the cell orientation can be attributed to the change in the strength of natural convection. Among them, the cell orientation of cold-above-hot (Figure 4-7a) led to an obvious natural convection effect (*Nu* and *Sh* are 1.6 and 6.0 through Eq. 4-3). The mass transfer of redox species through concentration diffusion was relatively slow but can be significantly increased by natural convection in the cell. Convection reduced the boundary layer near the electrode to accelerate heat and mass transfer, thereby increasing the current and power density (red line in Figure 4-14a, 4-14b and 4-14c). Conversely, when the hot-above-cold cell orientation (Figure 4-7b) is adopted, there was no natural convection (*Nu* = *Sh* = 1).[25] Therefore, even if the cell maintains a high open circuit voltage due to the weakening of the heat transfer

process, the increase in internal resistance caused by the weakened mass transfer greatly reduced the cell performance. (green line in Figure 4-14a, 4-14b and 4-14c).

However, for the horizontal orientation, the natural convection effect was affected by the aspect ratio (aperture/thickness) when using a separator.[37] For a separator with only one round hole and an aperture of 8.33 (Figure 4-2), the natural convection effect with the horizontal orientation thermocell can be calculated by Eq. 4-4, Nu = 15.2, Sh = 40.3. The effect of natural convection showed a significant increase, resulting in a significant decrease in open circuit voltage due to faster heat transfer (blue line in Figure 4-14c). For a separator with an aspect ratio of 0.67, it can be calculated by Eq. 4-4, Nu = 2.2, Sh = 9.4. The large increase in natural convection also caused a drop in the open circuit voltage (blue line in Figure 4-14b). Finally, for a separator with an aspect ratio of 0.33, Nu is calculated as 1.1 and Sh as 5.1. The porous structure of the small pore size in the separator weakened the effect of natural convection, especially in the heat transfer process. Therefore, the thermocell can still maintain a high open circuit voltage even after its orientation was changed (blue line in Figure 4-14a).

The above experiments show that the optimal design of the thermocell's orientation and the size of the separator is the key to improving cell performance. When there is natural convection in the cell, the influence of the orientation of the cell on the mass and heat transfer can be changed through the design of the separator, thereby maintain stable performance. For extremely thin thermocells (inter-electrode spacing < 1mm, $GrPr$ < 2000), since the effect of natural convection is very weak, the design of

the separator requires more consideration of heat and mass transfer processes caused by heat conduction and concentration diffusion.

4.4. Conclusions

In summary, I designed a planar liquid-state thermocell with low inter-electrode spacing using CNT buckypaper electrodes and laser-processed PTFE porous separators. A high output power density of 0.82 mW m^{-2} K^{-2} and an open circuit voltage of 29 mV were achieved at an electrode spacing of 50 μm and a temperature difference between 33 and 37 °C. To maintain the temperature difference in an extremely thin thermocell, the porous PTFE separator with a moderate pore size and straight passage pores was designed to suppress the heat transfer between the electrodes without greatly increasing the internal resistance. The CNT electrode has a large effective surface area, which increased the current density and output power density. The effects of natural convection, mass transfer, and heat transfer according to the cell orientation change were discussed for the improvement in the performance of low inter-electrode spacing thermocells. Crucially, my thermocell uses simple, inexpensive, and non-toxic materials to achieve a high output power density, and I believe that my findings will spur the development of ultra-low quality waste heat harvesting devices such as wearable devices to harvest human body heat.

4.5. Reference

[1] Hoffert, M. I.; Caldeira, K.; Benford, G.; Criswell, D. R.; Green, C.; Herzog, H.; Jain, A. K.; Kheshgi, H. S.; Lackner, K. S.; Lewis, J. S.; others. *Science* **2002**, *298*, 981–987.

[2] Kyriakopoulos, G. L.; Arabatzis, G. *Renewable and Sustainable Energy Reviews*. Elsevier Ltd April 1**, 2016**, pp 1044–1067.

[3] Tester, J. W.; Anderson, B. J.; Batchelor, A. S.; Blackwell, D. D.; DiPippo, R.; Drake, E. M.; Garnish, J.; Livesay, B.; Moore, M. C.; Nichols, K.; others. *Massachusetts Inst. Technol.* **2006**, *358*.

[4] Leonov, V.; Vullers, R. J. M. *J. Renew. Sustain. Energy* **2009**, *1*, 62701.

[5] Bhatnagar, V.; Owende, P. *Energy Sci. & Eng.* **2015**, *3*, 153–173.

[6] Siddique, A. R. M.; Mahmud, S.; Van Heyst, B. *Renew. Sustain. Energy Rev.* **2017**, *73*, 730–744.

[7] Dupont, M. F.; MacFarlane, D. R.; Pringle, J. M. *Chem. Commun.* **2017**, *53*, 6288–6302.

[8] He, J.; Tritt, T. M. *Science*. American Association for the Advancement of Science September 29**, 2017**, p 1369.

[9] Shakouri, A. *Annu. Rev. Mater. Res.* **2011**, *41*, 399–431.

[10] Venkatasubramanian, R.; Siivola, E.; Colpitts, T.; O'Quinn, B. *Nature* **2001**, *413*, 597–602.

[11] He, W.; Wang, D.; Wu, H.; Xiao, Y.; Zhang, Y.; He, D.; Feng, Y.; Hao, Y.-J.; Dong, J.-F.; Chetty, R.; others. *Science* **2019**, *365*, 1418–1424.

[12] Mao, J.; Zhu, H.; Ding, Z.; Liu, Z.; Gamage, G. A.; Chen, G.; Ren, Z. *Science* **2019**, *365*, 495–498.

[13] Kang, T. J.; Fang, S.; Kozlov, M. E.; Haines, C. S.; Li, N.; Kim, Y. H.; Chen, Y.; Baughman, R. H. *Adv. Funct. Mater.* **2012**, *22*, 477–489.

[14] Im, H.; Kim, T.; Song, H.; Choi, J.; Park, J. S.; Ovalle-Robles, R.; Yang, H. D.; Kihm, K. D.; Baughman, R. H.; Lee, H. H.; Kang, T. J.; Kim, Y. H. *Nat. Commun.* **2016**, *7*, 10600.

[15] Shin, G.; Jeon, J. G.; Kim, J. H.; Lee, J. H.; Kim, H. J.; Lee, J.; Kang, K. M.; Kang, T. J. *Molecules* **2020**, *25*, 1928.

[16] Duan, J.; Yu, B.; Huang, L.; Hu, B.; Xu, M.; Feng, G.; Zhou, J. *Joule* **2021**.

[17] Yu, B.; Duan, J.; Cong, H.; Xie, W.; Liu, R.; Zhuang, X.; Wang, H.; Qi, B.; Xu, M.; Wang, Z. L.; Zhou, J. *Science* **2020**, *370*, 342–346.

[18] Duan, J.; Feng, G.; Yu, B.; Li, J.; Chen, M.; Yang, P.; Feng, J.; Liu, K.; Zhou, J. *Nat. Commun.* **2018**, *9*.

[19] Im, H.; Kim, T.; Song, H.; Choi, J.; Park, J. S.; Ovalle-Robles, R.; Yang, H. D.; Kihm, K. D.; Baughman, R. H.; Lee, H. H.; Kang, T. J.; Kim, Y. H. *Nat. Commun.* **2016**, *7*.

[20] Guo, B.; Hoshino, Y.; Gao, F.; Hayashi, K.; Miura, Y.; Kimizuka, N.; Yamada, T. *J. Am. Chem. Soc.* **2020**, *142*, 17318–17322.

[21] Tang, L.; Wang, Y.; Li, Y.; Feng, H.; Lu, J.; Li, J. *Adv. Funct. Mater.* **2009**, *19*, 2782–2789.

[22] Nugent, J. M.; Santhanam, K. S. V; Rubio, a A.; Ajayan, P. M. *Nano Lett.*

2001, *1*, 87–91.

[23] Romano, M. S.; Li, N.; Antiohos, D.; Razal, J. M.; Nattestad, A.; Beirne, S.; Fang, S.; Chen, Y.; Jalili, R.; Wallace, G. G.; others. *Adv. Mater.* **2013**, *25*, 6602–6606.

[24] Hu, R.; Cola, B. A.; Haram, N.; Barisci, J. N.; Lee, S.; Stoughton, S.; Wallace, G.; Too, C.; Thomas, M.; Gestos, A.; Dela Cruz, M. E.; Ferraris, J. P.; Zakhidov, A. A.; Baughman, R. H. *Nano Lett.* **2010**, *10*, 838–846.

[25] Salazar, P. F.; Kumar, S.; Cola, B. A. *J. Appl. Electrochem.* **2014**, *44*, 325–336.

[26] Mua, Y.; Quickenden, T. I. *J. Electrochem. Soc.* **1996**, *143*, 2558.

[27] Qian, G.; Yu, X.; Li, Z.; Wu, J.; Huang, R.; Lu, Y. *Energy Convers. Manag.* **2020**, *217*, 113005.

[28] Qian, G.; Lu, Y.; Huang, Y.; Li, Z.; Yu, X.; Roskilly, A. P. *Energy Procedia* **2017**, *142*, 374–380.

[29] Holubowitch, N. E.; Landon, J.; Lippert, C. A.; Craddock, J. D.; Weisenberger, M. C.; Liu, K. *ACS Appl. Mater. Interfaces* **2016**, *8*, 22159–22167.

[30] Hasan, S. W.; Said, S. M.; Bakar, A. S. B. A.; Sabri, M. F. M.; Sajid, I. H.; Hashim, N. A. *J. Mater. Sci.* **2017**, *52*, 10353–10363.

[31] Hasan, S. W.; Said, S. M.; Sabri, M. F. M.; Jaffery, H. A.; Bakar, A. S. B. A. *Macromol. Mater. Eng.* **2018**, *303*, 1700482.

[32] Zhang, L.; Kim, T.; Li, N.; Kang, T. J.; Chen, J.; Pringle, J. M.; Zhang, M.; Kazim, A. H.; Fang, S.; Haines, C.; Al-Masri, D.; Cola, B. A.; Razal, J. M.; Di, J.; Beirne, S.; MacFarlane, D. R.; Gonzalez-Martin, A.; Mathew, S.; Kim, Y.

H.; Wallace, G.; Baughman, R. H. *Adv. Mater.* **2017**, *29*, 1605652.

[33] Wang, T. C.; Bury, W.; Gómez-Gualdrón, D. A.; Vermeulen, N. A.; Mondloch, J. E.; Deria, P.; Zhang, K.; Moghadam, P. Z.; Sarjeant, A. A.; Snurr, R. Q.; others. *J. Am. Chem. Soc.* **2015**, *137*, 3585–3591.

[34] Buckingham, M. A.; Aldous, L. *J. Electroanal. Chem.* **2020**, *872*, 114280.

[35] Cengel, Y.; Heat, T. M. *A Practical Approach*; New York, NY, USA: McGraw-Hill, **2003**.

[36] Prentice, G. *Electrochemical Engineering Principles*; Prentice Hall Englewood Cliffs, NJ, **1991**; Vol. 1.

[37] Bejan, A.; Tien, C. L. **1978**.

[38] Bauer, T. H. *Int. J. Heat Mass Transf.* **1993**, *36*, 4181–4191.

[39] O'Kelly, J.; Forster, R. *Analyst* **1998**, *123*, 1987–1993.

[40] Zhang, N.; Xie, J.; Varadan, V. K. *Smart Mater. Struct.* **2005**, *15*, 123.

[41] Cai, H.; Cao, X.; Jiang, Y.; He, P.; Fang, Y. *Anal. Bioanal. Chem.* **2003**, *375*, 287–293.

[42] Campbell, J. K.; Sun, L.; Crooks, R. M. *J. Am. Chem. Soc.* **1999**, *121*, 3779–3780.

[43] Gunawan, A.; Li, H.; Lin, C.-H.; Buttry, D. A.; Mujica, V.; Taylor, R. A.; Prasher, R. S.; Phelan, P. E. *Int. J. Heat Mass Transf.* **2014**, *78*, 423–434.

Chapter 5. Summary

Summary

The Sustainable Development Goals (SDGs), which advocate an integrated approach to solve development problems in the three dimensions of society, economy, and environment, are the major subject of concern in the next decade. However, the energy crisis and environmental problems caused by the massive use of non-renewable energy have become the biggest challenge to sustainable development. Waste heat, as an exhaust from the process of primary energy consumption, and as a low-grade energy widely distributed in the environment, is a renewable resource with high reuse value. In particular, the ultra-low-quality waste heat, which accounts for the highest proportion, lacks low-cost and efficient harvesting methods.

In this doctoral thesis, the author has developed a novel liquid-state thermocell based on the aqueous electrolyte with thermal responsive hydrogel nanoparticles. This thermocell can achieve efficient harvesting of ultra-low temperature waste heat by utilizing the volume phase transfer process of the nanoparticles near the ambient temperature. Through chemical and engineering strategies to optimize the design of electrolyte and thermocell devices, this kind of thermoelectric conversion device produces a recorded high voltage and cell performance. Moreover, as a practical example of such a simple, safe, and efficient system, an ultra-thin thermocell unit for body heat harvesting was assembled and demonstrated that it can generate high power density under extremely small temperature changes within the body temperature range. Thermocells using temperature-sensitive polymer electrolytes are a new field of

research. This pioneering study has given a new direction to research related to thermoelectric conversion and provided a promising solution for future energy problems in a sustainable society.

In chapter 2, a new thermoelectric conversion mechanism based on the proton-responsive redox reaction and the pH response of hydrogel nanoparticles was proposed. Quinhydrone and acrylic acid-containing thermal responsive hydrogel nanoparticles were used to illustrate this mechanism. This thermocell showed a high Seebeck coefficient of −6.7 mV K^{-1} and +6.1 mV K^{-1}, which is beyond the maximum value ever reported for liquid-state thermocells. The success of this concept involving entropy-driven phase transition opened a new arena for investigating high performance thermocells and became the cornerstone of follow-up research.

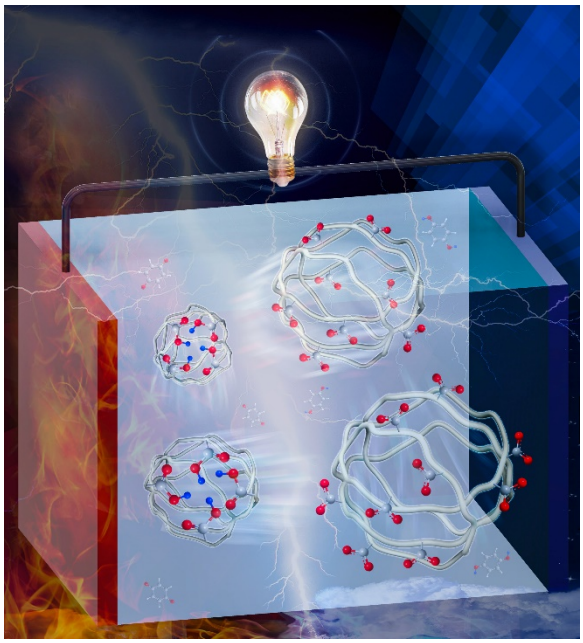

Figure 5-1. Schematic of a nanoparticle thermocell of entropy-driven phase transition.

In chapter 3, the design rationale of thermocell using thermal sensitive hydrogel nanoparticles were discussed. Through the screening of redox species, electrolyte salts, and NPs, the conditions necessary to achieve optimal thermocell performance were determined. The combination of 2,7-AQDS and poly(AAc-*co*-NIPAM) NPs achieved the highly efficient conversion of temperature differences to electrical energy at physiological temperature. The thermocell showed a high Seebeck coefficient of −9.5 mV K^{-1}, which exceeds those of reported liquid-phase thermocells. The screening process presented in this study provides a guide for the rational design of high-performance thermocell systems based on hydrogel nanoparticles. The optimal electrolyte composition shown by the experimental results was also used in subsequent studies.

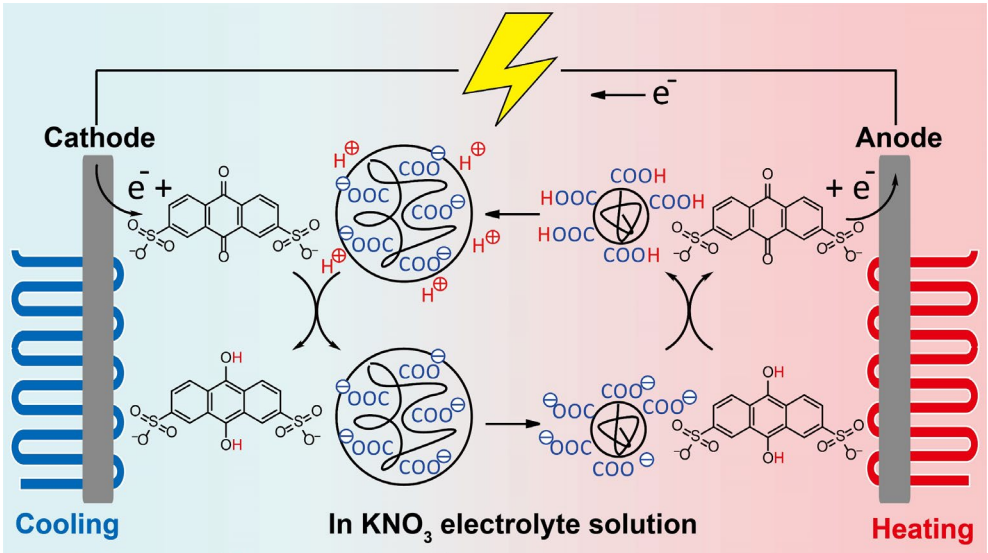

Figure 5-2. Optimal electrolyte composition of a nanoparticle thermocell.

In chapter 4, by assembling a thermocell device with low inter-electrode spacing, engineering strategies for optimizing cell performance were discussed. A planar liquid-state thermocell with low inter-electrode spacing was designed using CNT buckypaper electrodes and laser-processed porous separators. A high output power density of 0.82 mW m^{-2} K^{-2} is achieved at an electrode spacing of 50 μm and a temperature difference between 33 and 37 °C. The use of flexible and low-cost carbon electrode materials and the design of the ultra-thin cell size meet a variety of ultra-low-quality waste heat harvesting applications. Moreover, the high output power density that can be generated by a small temperature difference within the body temperature range is a very attractive result. Crucially, my thermocell uses simple, inexpensive, and non-toxic materials to achieve a high output power density, and I believe that my findings will spur the development of ultra-low quality waste heat harvesting devices such as wearable devices to harvest human body heat.

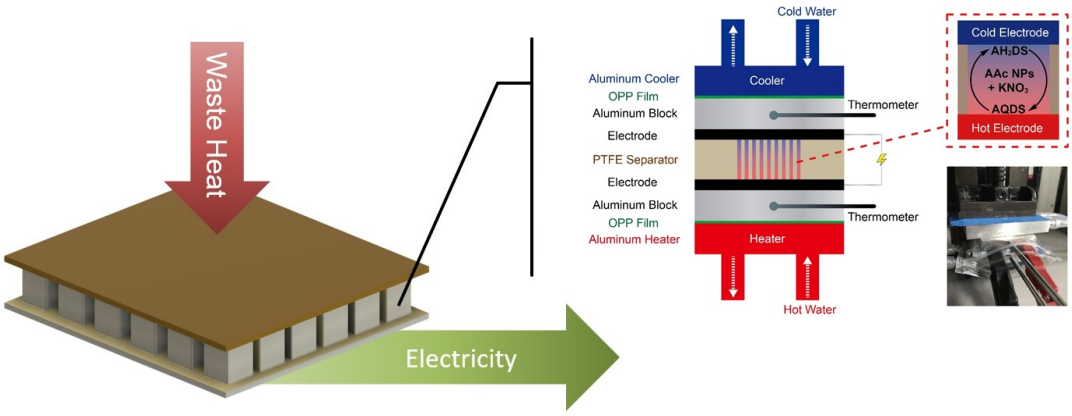

Figure 5-3. Schematic of thermoelectric conversion achieved by thermocell devices.

Acknowledgement

First of all, I am deeply grateful to Prof. Hoshino Yu for his careful guidance of my research. He is a researcher with unique insights and always has a sharp insight into the key points of the study. Under his instructions, I have gained a lot of growth, not only the quality and ability as a researcher, but also the persistence in dealing with difficult problems, the seriousness of work and so on.

I would like to thank Prof. Miura Yoshiko for giving me the opportunity to study in her laboratory. She is a learned and patient tutor, and she has given me a lot of care in my studies and life. As an international student, studying in an unfamiliar country always faces many unexpected difficulties. She can always give me a lot of understanding and help.

Thanks all the laboratory members for supporting me both in daily life and study, especially Dr. Cui, Dr. Nakamoto, Dr. Oh, and Dr. Matsumoto. As my predecessors, their hard work and research experience in the doctoral stage gave me a lot of inspiration and motivation. I would also like to thank Dr. Liu, Miss Wen and Mr. Jin. We also communicated a lot as international students and became very good friends.

Thanks to graduate program for leading graduate schools. I got a scholarship from the leading program to allow me to concentrate on research. In the past five years, I have met many friends in the leading program, and got the opportunity to study abroad. These experiences have made me grow a lot.

Finally, I would like to express my deepest gratitude to my mother. She raised me hard by herself and devoted a lot to my education. I will try my best to repay her kindness by becoming a better person in the future.